Universidad de Navarra

Facultad de Ciencias

Particle flows in silos, significance of particle shape, stiffness and friction

Tivadar Pongó

Universidad de Navarra

School of Science

Particle flows in silos, significance of particle shape, stiffness and friction

Submitted by **Tivadar Pongó** in partial fulfillment of the requirements for the Doctoral Degree of the University of Navarra

This dissertation has been written under my supervision in the Doctoral Program in Natural and Applied Sciences, and I approve its submission to the Defense Committee.

Signed on October 7, 2022

Dr. Raúl Cruz Hidalgo

Declaración:

Por la presente yo, **D. Tivadar Pongó**, declaro que esta tesis es fruto de mi propio trabajo y que en mi conocimiento, no contiene ni material previamente publicado o escrito por otra persona, ni material que sustancialmente haya formado parte de los requerimientos para obtener cualquier otro título en cualquier centro de educación superior, excepto en los lugares del texto en los que se ha hecho referencia explícita a la fuente de la información.

(I hereby declare that this submission is my own work and that, to the best of my knowledge and belief, it contains no material previously published or written by another person nor material which to a substantial extent has been accepted for the award of any other degree of the university or other institute of higher learning, except where due acknowledgment has been made in the text.)

Signed on October 7, 2022

Tivadar Pongó

To my family,

Acknowledgements

First of all I'd like to thank my supervisor, Raúl Cruz Hidalgo, for the lot of effort he spent so that I could grow as a scientist but even more for being awesome as a person. I truly had a great time with him which I will definitely miss. Secondly, I want to thank Tamás Börzsönyi for the rewarding close collaboration, I learned a lot from him during the years of my PhD. También quiero agradecer a los profesores del Laboratorio de Medios Granulares: Diego Maza, Iker Zuriguel, Ángel Garcímartin y a los otros profesores del departamento: Jorge Elorza, Javier Burguete, Sergio Ardanza, Wenceslao González-Viñas, Jean Bragard, Reinaldo García más a otros miembros: Silvia Olza y Luisfer Urrea por las discusiones fructíferas, por ayudarme con mis dudas, preguntas y tareas, por hacer de la UNAV un ambiente agradable y divertido. Además, gracias por las actividades extras, como las comidas juntas, paseos de bici, barbacoas y mucho más.

I thank my family: Köszönöm a családomnak, a szüleimnek és testvéreimnek a doktori elvégzése alatti támogatást. I thank my friends in Hungary, Roli, Zsolt, Dani for receiving and welcoming me when I was returning to Hungary. The friends I made here in Pamplona, from all over the world, for the fun we had together, ILCE and especially my Spanish teacher, Carmen for teaching me, las mesas de español for letting me meet many of these people.

También agradecería a todos mis compañeros de doctorado: Rodrigo, Marina, Jordan, Iñaki, William, Carlos Huesa, Dariel, Ilberto, Gella, Carlos Bejines, Bruno, Ruddy por el ambiente acogedor, por toda la diversión, las risas y el ambiente agradable en general. Agradezco especialmente a quienes me acompañaron durante las comidas, coffee breaks, viajes; los que me enseñaron español; aquellos que compartieron oficina conmigo, para poder conocerlos mejor y disfrutar el tiempo que pasamos juntos.

I thank Joshua Dijksman, the coordinator, and the other CALIPER supervisors: Tamás Börzsönyi, Ralf Stannarius, Devaraj van der Meer, Stefan Radl, Anke Lindner, Arno Mayrhofer, Christoff Kloss, Edward Andò, Alessandro Tenganttini, Cino Viggiani, and Martin Morgeneyer who made CALIPER possible, without their teamwork I wouldn't have been able to write this thesis. I also thank them for the discussions, for the effort put into our scientific development through training schools, especially thank those who I had the opportunity to work together with closely. I am also grateful to have worked together with other collaborators and coauthors outside of CALIPER: Dmitry Puzyrev, Kirsten Harth, János Török, Kiwing To. I also thank the European Union for giving me the opportunity and financial means to carry out my investigations in an excellent framework (Horizon 2020 Research and Innovation programme under the Marie Skłodowska-Curie grant agreement CALIPER No. 812638). Furthermore, I thank all the ESRs from CALIPER: Chandan, Lars, Francisco, Michael, Nazanin, Ahmed, Gustavo, Bo, Zorica, Ilija, Jing, Maheandar, Zohreh for all the great moments we had during training schools and other meetings. I'm grateful that I could get to know some of you even better during our secondments.

Thank you all!

Contents

Chapter 1

Introduction

1.1 Granular media

Granular materials are ensembles of macroscopic grains, which interact dissipatively, through contact and frictional interactions. We encounter them in the grocery shop: *rice*, *beans* or *chickpeas*, coffee made from ground *coffee beans*, or when we go to the beach and walk on the *sand*. Also, granular materials are the second most used type of matter in industry, after water. They are both ingredients and products of mining, construction and pharmaceutical processes.

The ensemble of grains makes up an interesting type of complex system, which can be either in solid, liquid or gas phase, depending on the energy input or applied forces. For example, in an hourglass, sand flows like a liquid driven by gravity until it runs out and forms a solid pile below, while asteroid belts and agitated grains can be examples of granular gases. Due to this complexity, it is important to investigate their dynamics, not only in order to understand natural events such as debris flow from a mountain, dune formation or landslides, but also in designing industrial processes, like material conveying or mixing. For these reasons, a significant amount of research is currently devoted to studying the micro- and macromechanical response of granular media. Thus, several research groups around the world are actively investigating this topic. One of these is the Granular Lab of the University of Navarra, where this PhD thesis has been written. This group executes extensive experimental and numerical studies on granular media composed of spherical and non-spherical particles (see Fig. 1.1), and other complex fluids.

1.2 Numerical modelling of granular materials

There are several theoretical paths to examine the macroscopic response of a granular sample. In general, the ultimate aim is the development of theoretical microstructural approaches from which the macroscopic constitutive laws can be derived. Furthermore, by combining general energy and momentum balance laws with these constitutive laws, and applying the boundary conditions of the specific setup, the experimental results can be explained.

An effective, accurate and frequently used numerical approach is the Discrete Element Method (DEM), first introduced by Cundall and Strack [1]. This considers all grains as distinct, soft particles

Figure 1.1: Grains used in experiments in the Granular Lab of the University of Navarra.

with their own position and velocity. When in contact, their overlap serves as the basis of most contact models [2], modeling the deformation of physical grains. After the forces acting on the particles are calculated, a time integration step is followed to obtain the new positions and velocities [3]. For non-spherical particles, the rotational degrees of freedom of the particle should also be integrated, very often conveniently by representing the grain orientation with a quaternion [4, 5]. In the calculations, the time step should be small enough [6, 7] to accurately account for the contacts. Therefore, this iteration is usually repeated many times, which makes this method computationally expensive. The numerical results presented in this thesis are obtained from DEM simulations.

Additionally, the macroscopic response of a granular system can be seen from a continuum perspective. Existing coarse-graining (CG) techniques allow the computing of smooth continuous macroscopic fields, in terms of the DEM output of a particle ensemble [8–10]. These procedures provide the macroscopic density, velocity, and stress fields, while satisfying the mass and momentum balance equations, thus they are extremely valuable for theoretical analysis.

Nevertheless, in industrial and engineering applications, the use of continuum modelling approaches for simulating granular samples is the most effective option. Typically, granular systems involve millions of particles and their description using discrete approaches is very inefficient or even inaccessible. In

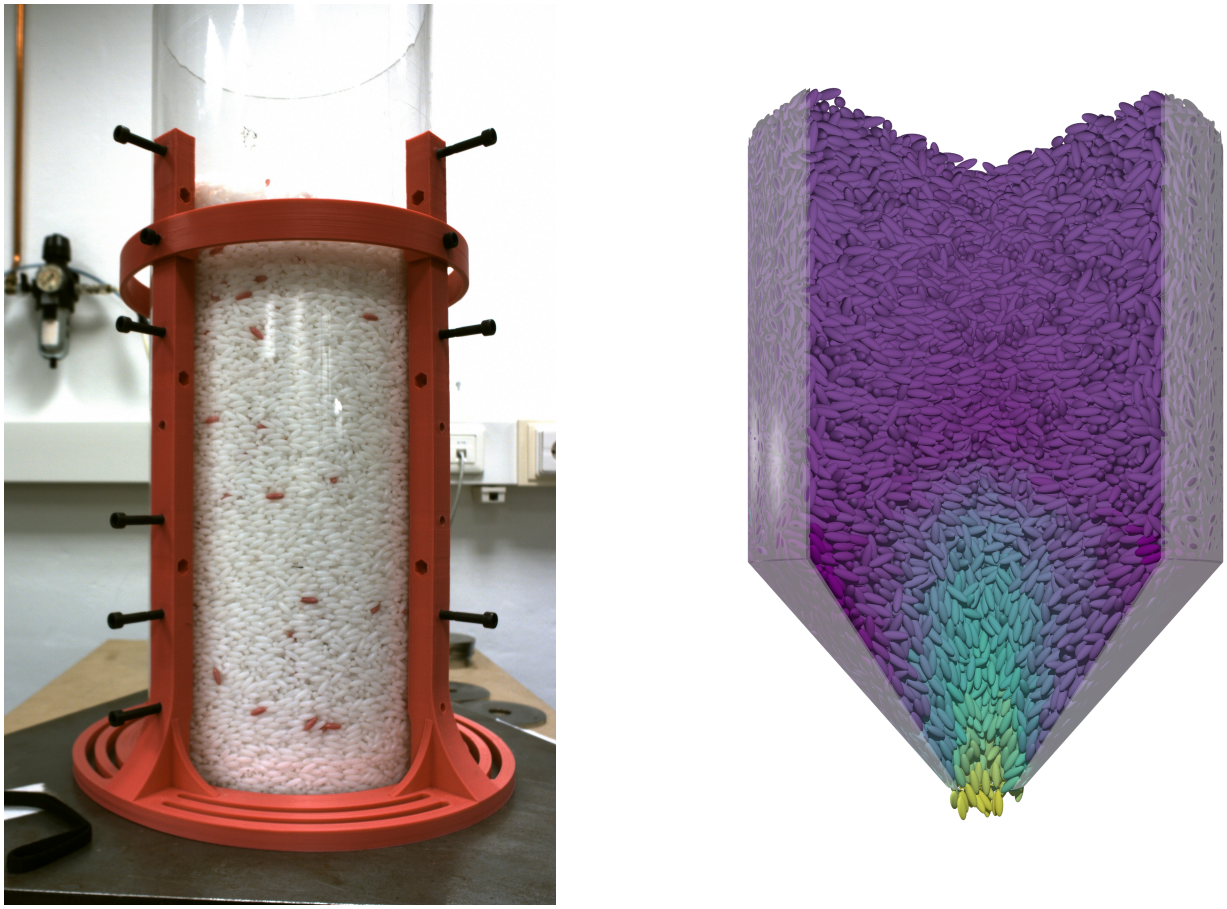

Figure 1.2: The use of Graphics Processing Units (GPUs) have enabled the computational analysis of large and dense experimental systems (for example, left). This allows us to get an insight into dense, complex flows such as the hopper discharge of ellipsoids, modelled as superquadric shapes (for example see right).

these cases, fluid-like solvers provide a more efficient although less accurate computational scheme. In general, they consider the particulate matter as a continuum (liquid or solid), obeying a system of equations based on the governing principles of mass, energy, and momentum conservation. These methods compromise the accuracy of the simulation by proposing simplified constitutive models (rheological response) for the granular media, which are typically motivated by empirical results.

A powerful rheological model for granular flows is the local $\mu(I)$ rheology [11, 12]. It considers the effective macroscopic friction μ, i.e. the ratio of the shear stress and pressure, to be a function of the dimensionless inertial number I. Here the inertial number is defined as $I = \dot{\gamma} d/\sqrt{P/\rho_p}$, where d is the particle diameter, $\dot{\gamma}$ is the shear rate, P is the confining pressure, and ρ_p is the particle density. This inertial number is constructed as the ratio of two timescales: the inertial $\sqrt{d^2\rho_p/P}$ and the shear $1/\dot{\gamma}$ timescale. Incompressible Navier-Stokes solvers have been implemented, using the $\mu(I)$ framework [13–15]. They typically yield better results in specific regimes where the classical fluid solvers fail to represent discontinuities and static zones. It is worth mentioning that, in some cases, simple local rheology approaches are not sufficient to reproduce experimental observations. Thus, a

non-local constitutive relation has also been proposed [16].

In particular, in this dissertation, we examine numerically the mechanical response of granular media by developing novel DEM algorithms and coarse-graining techniques. We have also used LIGGGHTS® [17], which is a well established computational program for particle modelling. In order to access large system sizes (up to half a million particles) and explore a relatively large parameter space, the most advanced High Performance Computing (HPC) techniques have been used. We commonly employed the standard message passing interface (MPI) when executing LIGGGHTS® on supercomputing clusters. MPI is a communication protocol that parallelizes and coordinates many individual processes, mapping them on the cluster nodes. When implementing coarse-graining algorithms on workstations, we used Open Multi-Processing (OpenMP), which is a developer-friendly program interface (API), including a set of compiler directives, library functions, and environment variables, that significantly improves the run-time.

On the other hand, Graphics Processing Units (GPUs) are currently powerful tools, used in many scientific projects, because of their high computing throughput and memory bandwidth. Moreover, GPUs have recently experienced a considerable increase in the number of cores and clock speed, without increasing the cost greatly. In this dissertation, we have developed hybrid CPU-GPU implementations of DEM, which have resulted in an excellent alternative to parallel computing on clusters or supercomputers. This is a flexible implementation, including GPU kernels that accurately compute the contact interaction between (frictional and non-frictional) spheres, spherocylinders and superquadrics (see Fig. 1.2).

1.3 Silo flow systems

The main topic of the thesis has been the investigation of silo flow. In order to store granular materials, humans for long have used silos and hoppers, which are indispensable in the industry even today. These appliances are containers with flat (silo) or inclined (hopper) bottoms with an opening in it. This simple design enables the utilization of gravity to discharge the stored material. Despite their simplicity, engineers face several challenges during their design and operation. These include segregation of mixtures composed of grains with different properties, like polydisperse systems, formation of stable arches near the orifice thus clogging the silo, and predicting the discharge rate based on measured material properties. Therefore, from a physicist's point of view, understanding and creating good models to describe the observed phenomena still poses a great challenge.

When 1 l of water is poured into a high container, the weight measured on the bottom corresponds, logically, to 1 kg. However, if we carry out the same experiment using a granular material, like sand, surprisingly we measure a lower weight than what would correspond to 1 kg. This is actually caused by the frictional nature of sand particles, since the frictional contacts transmit part of the weight of the column to the walls. The first theoretical description of this phenomenon was published in 1895 by Janssen [18]. His derivation implies a one minus exponential dependence [19] of the pressure p measured on the bottom versus the height h of a column:

$$p(h) = \rho_p \phi g \lambda (1 - e^{-h/\lambda}), \tag{1.1}$$

where ρ_p is the particle density, ϕ is the volume fraction, g is the gravitational acceleration, and λ is a

characteristic length which is proportional to the container diameter and inversely proportional to the coefficient of friction.

It has been long known that grains flow with a constant rate through an orifice, which is why the hourglass has been used since millennia to measure time. The mass flow rate Q of a silo with a circular opening on the bottom can be derived to depend on the orifice diameter D as a power law with an exponent of $5/2$, using dimensional analysis arguments. In 1961, Beverloo et al. [20] proposed an improved formula which works well for smaller orifices sizes and gives back the $D^{5/2}$ dependence when the orifice is large:

$$Q = C\rho_b\sqrt{g}(D - kd)^{5/2}, \tag{1.2}$$

where C and k are fitting parameters in the order of unity, ρ_b is the bulk density, and d is the grain diameter. They argued that the kd term can be justified by thinking that the margin of the orifice is less fit for the flow. Recently, Janda et al. [21] introduced an alternative formulation for the dependence of flow rate on the orifice diameter, based on observations of the self-similar density and velocity profiles in the region of the orifice:

$$Q = C'\rho_p\sqrt{g}\phi_\infty(1 - \alpha_1 e^{-D/\alpha_2})D^{5/2}. \tag{1.3}$$

Equation (1.3) corresponds to the three-dimensional case and C' is a constant that depends on the particle diameter and the curvature of the density profiles. ϕ_∞ is the asymptotic value of packing fraction for large orifices, ρ_p is the particle density and α_1, α_2 are fitting parameters. This formulation has a more fundamental base and works better than the Beverloo's correlation for small orifices where clogging might occur.

During the discharge of grains out of a flat-bottomed silo, the flow pattern is usually significantly different from that of a liquid. For example, water continuously flows out of a container, with the flow converging near the opening. Contrary to this, granular media often shows a funnel pattern in the flow field, which is characterized by stagnant zones near the silo corners and a flowing part in the center of the silo. In engineering applications, funnel flow is usually undesirable since at the end of the discharge process a part of the material remains inside the container and the material might exhibit segregation during the flow [22, 23]. A simple solution to this problem is the usage of an inclined bottom, that is, a hopper.

When the orifice of a silo is smaller than about 5 times the grain diameter, the system is prone to clogging due to the formation of stable arches (2D) or a dome-like structure (3D) at the exit. This phenomenon often causes problems in industrial processes. Very interestingly, blood cells flowing through constrictions in veins can exhibit similar events. In general, it is expected that smaller orifices lead to a greater probability of clogging, and this was quantified by To et al. [24] several years ago. An interesting theoretical question about the exit size dependence of clogging is whether there is a critical diameter above which there is no clogging or if clogging might happen at any orifice size but with a very low (practically zero) chance. Zuriguel et al. [25] offered an insight to this puzzle and argued that there exists a critical opening size, based on the measurements of the amount of particles discharged between subsequent clogs (avalanches).

The outflow in a silo with a fixed orifice size can be externally controlled using several approaches. In the past, the discharge have been perturbed, introducing vibrations [26–31], using electric fields [32], magnetic fields [33], or inducing a repulsive force between the grains [34, 35]. In particular, when

analyzing small orifices, it is accepted that introducing vibrations alters the arches' stability [28, 29], and the distributions of the unclogging times [30, 31].

Imposing an external shear is also an alternative to avoid the formation of stable arches. Years ago, a researcher explored the discharge of a cylindrical silo with rotating bottom [36]. However, they only focused their attention on the evolution of the system's surface [36]. Hilton and Cleary [37] examined the impact of the external shear on the flow rate Q, finding that it is unaffected when a low shear rate is applied. However, after reaching a critical value, Q increases monotonically with the rotational frequency f. To et al. [38] recently studied the discharge of plastic beads with diameter d in a silo with rotating bottom, varying both the orifice size D and the rotational frequency systematically. They observed sustained flow for very small orifice sizes $D < 5d$, and detected a weak non-monotonic behavior of Q vs f dependency. Despite considerable research examining these exciting phenomena, well-founded explanations for these complex responses are still lacking.

1.4 Caliper

This investigation has been done under the framework of CALIPER, which is an Initial Training Network funded by the EU Horizon 2020 research program under the Marie Skłodowska Curie grant agreement No 812638, in which I participated as an Early Stage Researcher (ESR). The consortium is coordinated by the Wageningen University, Netherlands and includes 15 academic and private sector partners. The main aim of CALIPER has been *to employ various 3D imaging modalities that have become more available in recent years to help calibrate and improve numerical methods and ultimately enhance our fundamental understanding of the mechanics and flow behavior of disordered materials.* Thus, the project has triggered an intense collaboration of leading experts in experimental techniques and numerical modelling in this field. It has made it possible that all the numerical models presented in this thesis have been calibrated and validated by their corresponding experimental counterparts. As a result, we have notably enriched the fundamental understanding of the mechanical response of granular media.

1.5 Objectives

It is well accepted, that particle shape, surface friction and the material mechanical properties play the most significant role in determining the macroscopic mechanical response of granular media. Non-spherical and irregular grains often exhibit enhanced macroscopic friction and interlocking, and have significant consequences for the flowability and stability of grain ensembles in numerous industrial situations. However, despite the fact that common granular media consists of non-spherical, and often elongated grains, a well-founded rheological model for the flow of non-spherical particles does not exist as of today.

As mentioned earlier, our research mainly focused on silo flow, investigating 2D and 3D configurations using particles with different properties and shape. These systems are examined using DEM, CG of spherical and non-spherical particles, varying the particle friction, stiffness, and restitution coefficient. In all cases, we explored the impact of these properties on the macroscopic response of the system, as well as on the micromechanics and macroscopic stress transmission.

The general objectives of the thesis are the following:

- To develop accurate computational models to predict the macroscopic response of granular materials with different particle features (shape, stiffness, and friction).
- Reduce the computational effort required for discrete element simulations by developing novel and highly efficient algorithms on modern computing platforms.
- To improve the understanding of flows of spherical and non-spherical grains, addressing the dependence of the rheological parameters on the grain features, based on the description of the flow's micromechanical details.

1.6 Thesis outline

This dissertation has been written in the modality of "Compendium of publications". It follows the regulation of the Doctoral Program in Natural and Applied Sciences of the Faculty of Science, University of Navarra, including the document structure, specific sections, and format of the included publications.

The document includes four publications, three of them in JCR journals, reviewing the numerical investigation of four different experiments, which are shortly described in the following.

- Chapter 2 includes the article with the following reference: Tivadar Pongó, Viktória Stiga, János Török, Sára Lévay, Balázs Szabó, Ralf Stannarius, Raúl Cruz Hidalgo and Tamás Börzsönyi. "Flow in an hourglass: particle friction and stiffness matter". *New Journal of Physics* **23** 023001 (2021) [39]. This is a result of a close collaboration with experimental partners of CALIPER. My main contribution to this work is the numerical and analytical analysis.
- Chapter 3 includes the article with the following reference: Jing Wang, Bo Fan, Tivadar Pongó, Kirsten Harth, Torsten Trittel, Ralf Stannarius, Maja Illig, Tamás Börzsönyi, Raúl Cruz Hidalgo. "Silo discharge of mixtures of soft and rigid grains". *Soft Matter* **17**, 4282-4295 (2021) [40]. This is a result of a close collaboration with experimental partners of CALIPER. My main contribution to this work is the numerical analysis. The first authorship is shared between Jing Wang, Bo Fan and Tivadar Pongó
- Chapter 4 includes the article with the following reference: Tivadar Pongó, Tamás Börzsönyi and Raúl Cruz Hidalgo, "Discharge of elongated grains in silos under rotational shear" *Physical Review E* accepted on 16 August 2022. It reviews a numerical analysis that mimics an experiment executed in collaboration with a researcher from the Academia Sinica (Taiwan) (see our publication Ref. [41])
- Chapter 5 includes the article with the following reference: Tivadar Pongó, Dmitry Puzyrev, Kirsten Harth, Ralf Stannarius, and Raúl Cruz Hidalgo. "Continuously heated granular gas of elongated particles". *EPJ Web of Conferences* **249**, 04004 (2021) [42]. Our numerical analysis mimics the experiment introduced in Ref. [43], which consists of a dilute granular gas of rod shaped grains heated in microgravity conditions.
- A brief discussion is included.

- The main conclusions of the thesis are summarized.

Chapter 2

Flow in an hourglass: particle friction and stiffness matter

Tivadar Pongó, Viktória Stiga, János Török, Sára Lévay, Balázs Szabó, Ralf Stannarius, Raúl Cruz Hidalgo, Tamás Börzsönyi

New Journal of Physics **23** 023001 (2021) DOI: 10.1088/1367-2630/abddf5

Granular flow out of a silo is studied experimentally and numerically. The time evolution of the discharge rate as well as the normal force (apparent weight) at the bottom of the container is monitored. We show, that particle stiffness has a strong effect on the qualitative features of silo discharge. For deformable grains with a Young's modulus of about $Y_m \approx 40$ kPa in a silo with basal pressure of the order of 4 kPa lowering the friction coefficient leads to a gradual change in the discharge curve: the flow rate becomes filling height dependent, it decreases during the discharge process. For hard grains with a Young's modulus of about $Y_m \approx 500$ MPa the flow rate is much less sensitive to the value of the friction coefficient. Using DEM data combined with a coarse-graining methodology allows us to compute all the relevant macroscopic fields, namely, linear momentum, density and stress tensors. The observed difference in the discharge in the low friction limit is connected to a strong difference in the pressure field: while for hard grains Janssen-screening is effective, leading to high vertical stress near the silo wall and small pressure above the orifice region, for deformable grains the pressure above the orifice is larger and gradually decreases during the discharge process. We have analyzed the momentum balance in the region of the orifice (near the location of the outlet) for the case of soft particles with low friction coefficient, and proposed a phenomenological formulation that predicts the linear decrease of the flow rate with decreasing filling height.

2.1 Introduction

Gravity driven discharge of a granular material from a silo or hopper is a frequent operation in various industrial procedures [21, 44–50]. Materials involving deformable and/or viscoelastic grains with low surface friction pose new challenges for controlling the flow of such samples. Several experimental and numerical studies have shown that for frictional hard grains the discharge rate of a silo is constant and independent of the filling height [44, 51–56], if the orifice diameter D is larger than about 5 particle diameters [25]. This feature is very useful in engineering applications and lead to the emergence of simple devices such as the hourglass. More precisely, the flow rate was found to be constant until near the end of the discharge when the shape of the bed surface (often having a form of a funnel) starts perturbing the outflow. These results hold for such particles as spherical beads of various materials (glass, steel, lead, plastic) [51–53, 57–59], nearly spherical particles (e.g. peas) [55], grains with irregular shape (e.g. sand) [49], or slightly anisometric grains (wheat, corn, soybeans, poppy seeds, oat) [54, 56]. The fact that the flow rate was found to be constant for a wide range of materials facilitated the characterization of the outflow as a function of the orifice diameter D. The flow rate Q in a three-dimensional (3D) silo was found to vary approximately as $D^{5/2}$, where the best fit was obtained either using an effective orifice diameter in place of D, taking into account the grain size d [20, 44, 49], or taking into account the slight density decrease near the orifice with decreasing orifice size [51]. This so-called Beverloo scaling was experimentally tested in various systems and was shown to work even at increased or decreased gravitational acceleration [60].

It is also known that the weight of the material in the silo is partly supported by the frictional contacts with the walls. As a consequence, the basal pressure p_b (i.e. the normal stress measured at the bottom of the silo) saturates with increasing fill height h. This phenomenon was first systematically investigated by Janssen [18, 61], who confirmed the earlier measurements of Huber-Burnand [62], Hagen [49, 63], and Roberts [64]. The so-called Janssen effect is also present when the contacts are mobilized (experiments with moving walls) [19, 65] and the $p_b(h)$ curve is best described by a combination of a linear section (hydrostatic behaviour) at the bottom of the silo and an exponential saturation in the upper section [65, 66], where the saturation length is comparable to the silo diameter D_{silo}.

The height-independent constant basal pressure would serve as a good argument for the constant flow rate as several authors mentioned [45, 46, 48, 50, 51, 67]. For comparison, in a cylinder filled with a liquid the discharge rate is clearly determined by the pressure (compare, for example, the clepsydra), which is linearly increasing with the height of the liquid column. In the low viscosity limit, the conservation of energy leads to a flow rate Q proportional to $\sqrt{h}$ (Torricelli's law). For large viscosities, dissipation dominates near the outlet, leading to $Q \propto h$. Investigations on granular flows showed, however, that the discharge rate is independent not only on h, but also on the silo diameter D_{silo} in case $D_{silo} > 2.5D$ and $D_{silo} > D + 30d$ [68, 69]. Thus, a simple relation between Q and p_b has to be dropped, since according to the above described Janssen effect, p_b clearly increases with D_{silo}. Pacheco-Martinez et al. also showed [52] that slightly vibrating the hopper wall one can get hydrostatic conditions in the pressure profile (i.e. Janssen screening disappears), but when the orifice is opened, Janssen screening reappears, and the silo still discharges the same way as without vibration. Other recent experiments showed that different filling protocols might lead to different pressure profiles, but the flow rate was found to be independent of the basal pressure [57, 70].

The mechanism leading to a constant discharge rate of a granular material is still the subject of active research. Detailed experimental and numerical investigations are carried out to analyze the flow near the orifice, where the nature of dissipation clearly changes. There is a region with paraboloid or hemispherical shape below which dissipation strongly drops. This was first identified by Hagen [63]. Based on this, Brown and Richards introduced the concept of a free-falling arch signifying the region where energy dissipation decreases to a minimum [68]. At this surface, the stress in flow direction vanishes and from here the grains are freely falling [71]. Similar reasoning lead to the development of an alternative approach called the hourglass theory, which predicts the discharge rate quantitatively [72, 73]. Recent works tested and refined these ideas [44, 51, 56, 67, 74, 75]. Among these, Darias et al. derived differential equations based on energy balance and the so called $\mu(I)$ rheology [75]. Their results are compatible with the Beverloo law, and the authors found an increase in the flow rate when the interparticle friction is reduced. They also validated their theory numerically by 3D Discrete Element Model (DEM) simulations.

Other recent investigations tested the limitations, i.e. identified conditions where the flow rate is not constant anymore. Introducing an interstitial fluid clearly changes the dynamics, resulting in an increased flow rate near the end of the discharge process [59, 76]. Recently, this effect was shown to be present – although with a much smaller amplitude – in dry granular flows of glass beads in case the particles were sufficiently small ($d < 1$ mm) [58]. For $d = 2$ mm glass beads, the flow rate was again found to be constant [59]. Another investigation pointed out that applying a large stationary external force leads to an increased flow rate during the discharge of a dry granular material [77].

Some of the earlier numerical investigations mentioned that decreasing the frictional damping leads to height dependent (i.e. not constant) flow rates [78, 79]. Another numerical work reported strongly changing pressure conditions, but only slightly increasing flow rates with decreasing wall friction [80]. Using discrete element simulations, Balevicius indicated decreasing flow rates with increasing interparticle friction in a quasi-2D system with limited size, and a time dependent flow rate [81]. In the above-mentioned recent work by Darias et al. [75] on a 3D system, a time dependent (slightly decreasing) flow rate is noticeable for their lowest value ($\mu = 0.1$) of the friction coefficient. Langston et al. [82] investigated the case of frictional grains ($\mu = 0.6$) and found that the discharge rate was rather insensitive to the stiffness of the interparticle interactions. In a different numerical approach, Staron et al. implemented a plastic rheology in a 2D Navier-Stokes solver (following the so called $\mu(I)$ rheology or constant friction) [13], which showed a transition from granular-like (constant flow rate) to liquid-like (decreasing flow rate) behaviour with decreasing friction below about $\mu = 0.3$.

In the present work, we show that the discharge behaviour of low friction soft hydrogel beads strongly differs from the case of hard frictional grains described by a constant flow rate. We quantify the difference in laboratory experiments by measuring the flow rate and the normal force exerted on the bottom of the silo during the discharge process for both low friction soft and frictional hard grains. We perform numerical (Discrete Element Method) simulations to explore the effect of grain softness and surface friction on the flow rate as well as on the stress conditions inside the silo. Our work was motivated by recent investigations on clogging statistics of soft particles in two-dimensional hoppers [83–85] and X-ray tomographic measurements on the flow field of soft particles in a three-dimensional hopper [86, 87], all of which noticed a fill height dependence of the clogging probability or the flow properties.

2.2 Experimental system

An acrylic cylindrical silo with inner diameter $D_{\text{silo}} = 144$ mm and height $H = 800$ mm was used. The bottom plate was physically disconnected from the silo with a gap of approximately 1 mm, and it was held by a load cell enabling a continuous monitoring of the force F_{b} exerted on the bottom (see Fig. 2.1). Two types of filling protocols were used: pouring the grains into the silo with faster (500 cm^3/s) and slower (50 cm^3/s) speed. Lower pouring rates resulted in slightly (a few percent) denser packing of the granular bed (see Fig. 2.1 for the data). The silo was discharged through a circular orifice of diameter D in the middle of the bottom plate. The typical discharge time was in between 50–100 s. During discharge, both the force F_{b} exerted on the bottom of the silo and the discharged mass were continuously measured by the load cells at a sampling rate of 1 kHz. The data series were then smoothed by a convolution with a Bartlett (triangle) window of a width of 1 s to reduce noise. The data for the discharged mass were differentiated and smoothed again with the same smoothing procedure to obtain the flow rate Q. The value of Q is presented in grains/s. For this purpose, the average unit mass of the individual grains was determined by measuring the mass of 200 grains. The evolution of the fill height h during discharge of hard grains was calculated from the discharged mass data assuming a linear relation between the height and the mass in the silo. For soft grains, pressure induces compression of the material, so the discharged mass–fill height relation was approximated by a third order polynomial which was previously calibrated.

Four granular samples have been used in the experiments: nearly spherical pea seeds (supplier: Gyari-Mag BT, Hungary), two samples of spherical glass beads (with diameters in the range of 2.85 mm $< d <$ 3.45 mm and 6.7 mm $< d <$ 7.3 mm, both from Sigmund-Lindner GMBH, Germany), and spherical hydrogel beads (Happy Store, Nanjing, China) (see Fig. 2.1). For the glass bead samples, we used two versions: clean and lubricated. Lubrication was achieved by spraying the glass beads ($\approx$ 20 kg) before pouring them into the silo as well as the inner surface of the silo with about 500 ml of silicone oil (Motip). The table also indicates the packing fractions resulting after fast or slow filling of the silo. For the hydrogel beads, the packing fraction depends on the magnitude of the contact forces, thus it changes with height [86].

Three samples (peas, clean glass beads with $d = 3.15$ mm and $d = 7$ mm) are considered frictional hard grains with a friction coefficient of about 0.3–0.5, while the hydrogel balls are soft and have very small interparticle friction coefficient. By measuring the Hertzian contact diameters, the Young's modulus Y_m of our hydrogel spheres was found to be between 30 and 50 kPa [83], with a slightly softer outer part than the core. This is similar to the results of other measurements with hydrogel beads, which yielded a Young's modulus of $Y_m \approx 20$ kPa [88]). In earlier studies, the interparticle friction coefficient of hydrogel beads was found to be $\mu_p < 0.03$ [89]. We will show below that the discharge of the low friction soft hydrogel particles is very different from the frictional hard grains. This motivated us to reduce the surface friction of our glass bead samples by spraying silicone oil on the surface of the beads as well as on the silo wall.

The friction coefficient for hard surfaces with a lubricating layer depends on the normal force and the sliding velocity [90], so we carried out experiments on inclined planes to measure this friction coefficient. In the *first set* of experiments, a wooden block of a mass of 188 g was used with three glass beads glued on it serving as three legs. The inclination angle was determined at which the block was sliding

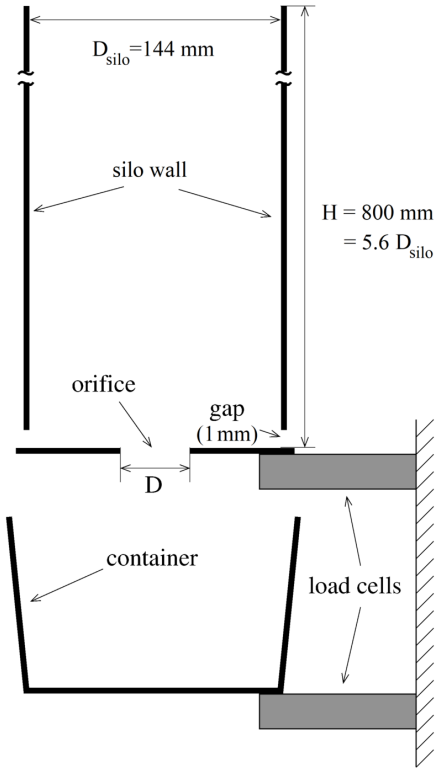

	peas	glass beads	glass beads	hydrogel beads
	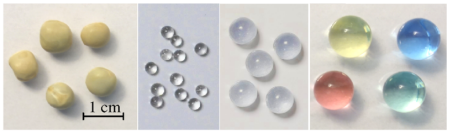			
d (mm)	6.92	3.15	7	9.2
ρ_p (g/cm^3)	1.3	2.5	2.5	1.0
Y_m (Pa)	$5{\cdot}10^7$	$5{\cdot}10^{10}$	$5{\cdot}10^{10}$	$4{\cdot}10^4$
φ_{fast}	0.63	0.63	0.63	0.72–0.78
φ_{slow}	0.68	0.65	0.65	

Figure 2.1: Sketch of the experimental setup and photographs of the samples, with the grain diameter d, particle density ρ_p, and Young modulus Y_m indicated below. The initial packing fractions in the silo corresponding to fast and slow filling, φ_{fast} and φ_{slow} are also given.

without acceleration on an acrylic flat surface (similar to the silo wall). The friction coefficient was determined as the tangent of the inclination angle. For clean glass beads and a clean surface, the friction coefficient was $\mu_{\text{clean}} = 0.44$, while for lubricated glass beads and a lubricated surface, we got a considerably reduced value $\mu_{\text{lubricated}} = 0.015$. The surface of the hydrogel beads is naturally wet, so for these grains the same measurement was repeated without any lubricant, and resulted a friction coefficient of $\mu_p = 0.02$. We note that the typical normal force in these tests was much larger (a few hundred times) than the weight of a single grain. In the *second set* of experiments, a thin plastic foil was used instead of the wooden block, thus the sliding object essentially had the weight of the three beads. In this case the measured sliding friction coefficient of the clean glass beads was $\mu_{\text{clean}} = 0.27$ for the smaller ($d = 3.15$ mm), and $\mu_{\text{clean}} = 0.18$ for the larger ($d = 7$ mm) beads. For lubricated glass beads, stationary sliding was observed for a wide range of the plane inclinations $35^o < \theta < 60^o$ for $d = 3.15$ mm, and $11^o < \theta < 20^o$ for $d = 7$ mm, corresponding to friction coefficients of $0.7 < \mu < 1.7$ and $0.19 < \mu < 0.36$ for small and large beads, respectively. The stationary sliding speed was typically a few cm/s, it increased with θ. Thus, for the case of glass beads for typical sliding velocities observed in our silo during discharge the friction coefficient at lubricated contacts changes considerably with the normal force. For certain contacts it can be similarly small to the case of soft hydrogel beads, for other contacts its value is much larger, it is similar to that of dry glass bead contacts.

2.3 Numerical system

Discrete Element Method (DEM) simulations were performed using LIGGGHTS [17], a general granular simulation software. The DEM algorithm resolves the particle–particle interactions, and integrates both the translational and rotational motion of each particle. The interaction force $\vec{F}_{ij}$ between two contacting particles i and j was computed using the Hertz-Mindlin model with no-slip condition, the default nonlinear implementation of LIGGGHTS [2]. This numerical scheme allows the estimation of the elastic and damping interaction parameters given the Young modulus Y_m, Poisson's ratio ν of the material, the normal restitution coefficient e_n and friction coefficient μ of the particles. Moreover, the magnitude of the elastic tangential force $|\vec{F}^t_{ij}|$ is constrained by the normal one, $|\vec{F}^n_{ij}|$, satisfying the Coulomb constraint $|\vec{F}^t_{ij}| < \mu|\vec{F}^n_{ij}|$. The effect of rolling resistance and resistance to torsion were not taken into account.

We use a cylindrical silo with similar dimensions as the experimental system, spherical beads with a polydispersity of the grain diameter of $\pm 10\%$ for hard beads and monodisperse for the case of soft particles. Test runs indicated that for the case of hard grains, polydispersity was necessary, as for a monodisperse system increased velocity fluctuations were observed (most probably due to local spatial ordering). No such differences were observed for the case of soft grains. The discharge process was simulated for various values of the material parameters by systematically changing the Young modulus, the normal restitution coefficient e_n and friction coefficient μ, while a constant particle density $\rho_p = 1000$ kg/m^3 and Poisson's ratio of $\nu = 0.45$ was used in all cases. For the case of hard grains we used $Y_m = 5 \cdot 10^8$ Pa which results in a negligible Hertzian normal deformation $\delta_n/d \sim (p_b/Y_m)^{2/3} = 4 \cdot 10^{-4}$ for a basal pressure of $p_b = 4$ kPa. For soft grains, we used $Y_m = 1.25 \cdot 10^5$ Pa yielding $\delta_n/d \sim (p_b/Y_m)^{2/3} = 10^{-1}$. The particle-wall interaction was modeled using the same contact parameters used for particle-particle interaction. The time steps were estimated to be less than $t_c/40$, where t_c is the contact time.

For the preparation of the initial state of the simulations, the positions of the particles were generated using the random sequential deposition model in order to avoid overlaps between particles. For each configuration (interparticle friction and material stiffness), the procedure was realized using two protocols: one with an interparticle friction coefficient of $\mu_F = 0.5$ and one with zero interparticle friction. This was done to mimic the fast and slow filling procedures in the experiment, respectively. Here, filling the silo with zero interparticle friction resulted in a slightly higher initial packing. After filling, the orifice is opened and the material starts to flow out of the container.

Similarly to the experiments, we monitored two macroscopic quantities during the outflow process. First, the flow rate was calculated using the number of particles exiting the silo in fixed time intervals of 0.1 s. Second, the vertical component of the total force acting on the bottom surface was calculated. The mean height of the column was estimated averaging the highest particle locations within 8 equally spaced intervals in the radial direction.

2.3.1 Coarse-grained continuum description

In order to extract the averaged macroscopic fields from the DEM data, a coarse-graining (CG) micro-macro formulation can be derived from the classical laws of conservation [9, 91–93]. Thus, this procedure

leads to expressions for macroscopic density, velocity and stresses, in terms of particle properties and the contact interactions.

Starting with the DEM data for the positions and velocities of the particles, the microscopic mass density of a granular flow $\rho(\vec{r},t)$ can be defined [9, 91–93] at time t as

$$\rho\left(\vec{r},t\right)=\sum_{i=1}^{N}m_i\phi\left(\vec{r}-\vec{r}_i(t)\right), \tag{2.1}$$

where the sum runs over all the particles within the system and $\phi\left(\vec{r}-\vec{r}_i(t)\right)$ is an integrable coarse-graining function, which was chosen to be a 3D Gaussian function with standard deviation equal to the mean particle radius $d/2$. In the same way, the coarse-grained momentum density function $\vec{P}(\vec{r},t)$ is defined by

$$\vec{P}(\vec{r},t)=\sum_{i=1}^{N}m_i\vec{v}_i\phi\left(\vec{r}-\vec{r}_i(t)\right), \tag{2.2}$$

where $\vec{v}_i$ represents the velocity of particle i. The macroscopic velocity field $\vec{V}(\vec{r},t)$ is then defined as the ratio of momentum and density fields,

$$\vec{V}(\vec{r},t)=\vec{P}(\vec{r},t)/\rho(\vec{r},t). \tag{2.3}$$

In order to define the mean stress field, we have used a very elegant and mathematically consistent definition of mean stress $\bar{\sigma}_{\alpha\beta}$ introduced by Goldhirsch [9]. Following this approach, the total stress field $\sigma_{\alpha\beta}$ is composed by the kinetic stress field $\sigma^k_{\alpha\beta}$ and the contact stress field $\sigma^c_{\alpha\beta}$. They are defined as follows. The mean contact stress tensor reads as

$$\sigma^c_{\alpha\beta}(\vec{r},t)=-\frac{1}{2}\sum_{i=1}^{N}\sum_{j=1}^{Nc_i}f_{ij\alpha}r_{ij\beta}\int_0^1\phi(\vec{r}-\vec{r}_i+s\vec{r}_{ij})ds, \tag{2.4}$$

where the sum runs over all the contacting particles i,j, whose centers of mass are at $\vec{r}_i$ and $\vec{r}_j$, respectively. Moreover, $\vec{f}_{ij}$ accounts for the force exerted by particle j on particle i and $\vec{r}_{ij}\equiv\vec{r}_i-\vec{r}_j$.

The kinetic stress field reads as

$$\sigma^k_{\alpha\beta}(\vec{r},t)=-\sum_{i}^{N}m_iv'_{i\alpha}v'_{i\beta}\phi\left(\vec{r}-\vec{r}_i(t)\right), \tag{2.5}$$

where $\vec{v}'_i$ is the fluctuation of the velocity of particle i, with respect to the mean velocity field.

$$\vec{v}'_i(t,\vec{r})=\vec{v}_i(t)-\vec{V}(\vec{r},t). \tag{2.6}$$

Once the total stress tensor $\sigma_{\alpha\beta}(\vec{r},t)=\sigma^k_{\alpha\beta}(\vec{r},t)+\sigma^c_{\alpha\beta}(\vec{r},t)$ is found, the pressure at any location $p(\vec{r},t)=\frac{1}{3}Tr(\sigma_{\alpha\beta}(\vec{r},t))$ can be calculated.

Based on the previous theoretical framework, we implemented a post-processing tool which allowed us to examine all the micro-mechanical properties of the particulate flow. Taking benefit of the cylindrical symmetry of the system, one can average quantities within the azimuthal direction. As a result, the obtained macroscopic fields are in cylindrical coordinates r and z. We will denote averaged quantities as

$$X(r,z,t)=\frac{1}{2\pi}\int_0^{2\pi}X(\vec{r},t)d\varphi. \tag{2.7}$$

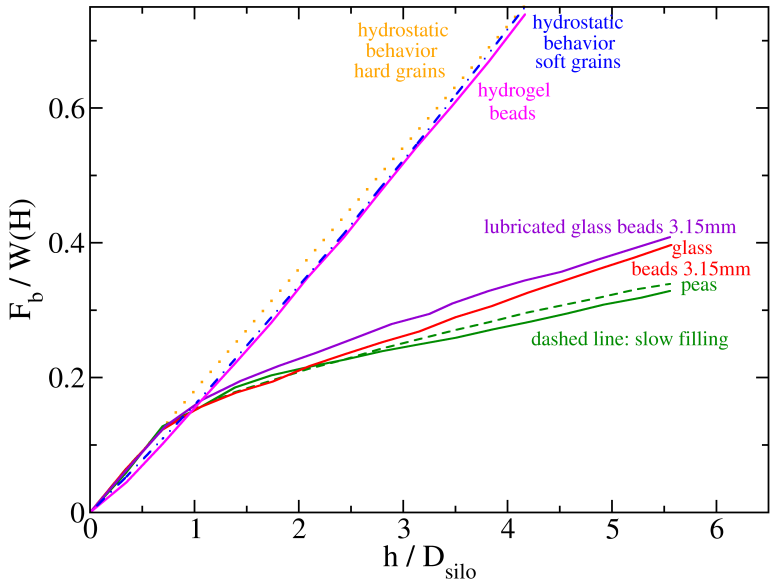

Figure 2.2: Experimental filling procedure: basal force F_b as a function of the fill height h. For normalizing the basal force we use the total weight $W(H)$ of the sample which fills the silo entirely.

2.4 Results

2.4.1 Filling the silo

As discussed in the introduction, it is long known that for a frictional granular material the force F_b at the bottom of a silo deviates from the hydrostatic behaviour, as part of the weight is supported by frictional contacts with the silo walls [18, 61]. This effect is clearly seen for the frictional samples in Fig. 2.2, where we normalize the basal force F_b by the weight of the material $W(H)$ corresponding to a full silo. For peas, two curves are presented, corresponding to the preparation protocols with filling speeds of 500 cm^3/s (continuous lines) and 50 cm^3/s (dashed lines). The slower filling procedure (leading to denser packing) resulted in slightly higher pressure at the bottom of the silo, i.e. in this case contact forces with the silo wall are weaker. In these measurements the silo was filled in 16 steps, and the filling height was measured visually in each step taking benefit of the transparent silo wall.

For hydrogel beads, the curve is very close to the hydrostatic behaviour, which is coherent with the very low friction coefficient ($\mu_p < 0.03$) of these particles. Note that for this material the packing fraction increases with pressure, especially at low pressures. This leads to the fact that for such a compressible material the hydrostatic curve is not a straight line but its slope increases with h/D_{silo}, especially at filling heights $h \leqslant D_{silo}$. For this material, we filled the container only up to a height of 60 cm ($h/D_{silo} = 4.17$), since at complete filling (80 cm) the pressure at the bottom of the silo occasionally caused breaking of some beads, pushing fragments into the gap between silo and bottom plate.

The F_b curve for the lubricated glass beads is not similar to that of the hydrogel beads, but almost the same as that of the dry glass beads. This is due to the complex nature of lubrication, which is characterized by a contact force dependent friction coefficient as demonstrated in section 2.2. Moreover the thin layer of silicone oil also results in a cohesive interaction at the grain-grain or grain-wall contacts. The magnitude of the cohesive force can reach the weight of a grain. We have observed, that

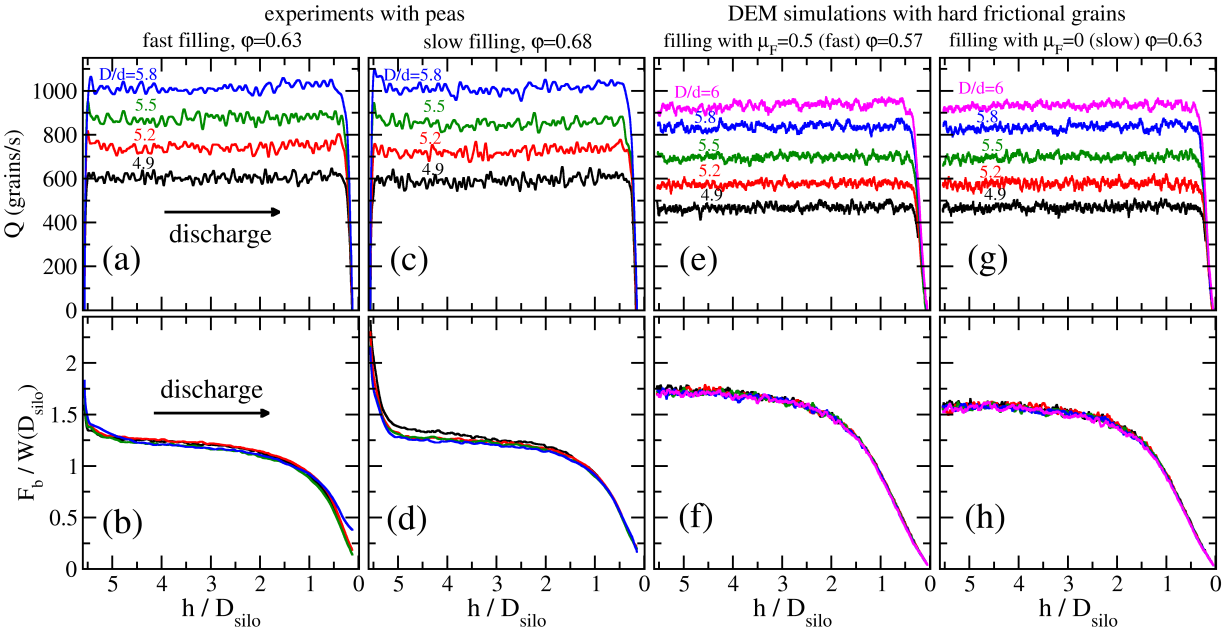

Figure 2.3: Silo discharge of hard frictional grains: (a-d) experiments with peas and (e-h) DEM simulations with spherical grains with friction coefficient of $\mu = 0.3$, Young's modulus of $Y_m = 5 \cdot 10^8$ Pa (inelastic) and a restitution coefficient of $e_n = 0.9$. The top panels show the evolution of the flow rate Q, while the bottom panels present the normal force F_b exerted on the silo bottom during the discharge process. The value of F_b was normalized by the weight $W(D_{silo})$ of the material corresponding to a filling height of the diameter of the silo. The two types of initial conditions (slow and fast filling of the silo) result in very similar discharge processes both in experiment and simulation. The initial fill height was $h_0/D_{silo} = 5.56$, while the initial packing fraction φ is indicated at the top. Each curve represents the average of 4 measurements. The silo diameter was $D_{silo}/d = 20.8$ (experiments) and $D_{silo}/d = 15$ (simulations) with mean particle diameters of $d = 6.92$ mm in both.

after discharge a few grains remain on the wall, and slide down only very slowly.

2.4.2 Silo discharge: comparison of experiments and simulations

The discharge curves, i. e. the time evolution of the flow rate Q and the force F_b exerted at the bottom of the silo during discharge are presented for peas in Fig. 2.3(a-d) for both types of initial preparation (slow and fast filling). As is seen, both the flow rate Q and the basal force F_b had a very similar time evolution for the two types of preparation. Looking at the top panels, we see that the flow rate was basically constant during discharge, even when the pressure conditions at the bottom of the silo changed during the process. The flow rate curves are the same for the two types of initial conditions, i.e. changing the initial density did not affect the discharge rate.

The bottom panels show that the basal force first decreased relatively quickly to the same level for both initial conditions. This drop is partly attributed to the activation of the force network transferring weight to the container walls. After this initial transient – which was finished when about 5% of the total mass was discharged – the basal force decreased only slightly until h was approximately $2D_{silo}$, and

then a faster decrease rate set in. We note that the F_b curves measured for different orifice diameters D in Figs. 2.3(b) and (d) overlap, thus the basal force does not depend on the discharge rate.

We now compare the above experimental observations with the results of DEM simulations for hard beads with Young's modulus of $Y_m = 5 \cdot 10^8$ Pa and a restitution coefficient of $e_n = 0.9$. Similarly to the experiments, these results have been obtained with frictional grains (friction coefficient: $\mu = 0.3$) for both cases: filling with $\mu_F = 0.5$ and $\mu_F = 0$, corresponding to fast and slow filling, respectively. As we see in Fig. 2.3(e-h), the numerical data reproduce all the features observed in the experiments: constant flow rate despite the changes in the basal force, same basal force curves for different orifice sizes (i.e. for different discharge rates), and very similar values of the measured parameters for the two initial conditions. There is only a slight quantitative difference between experiment and simulation: the flow rate is a bit lower and the basal force is a bit higher in the simulations.

The discharge of low friction, soft hydrogel beads is remarkably different from the traditional granular discharge demonstrated above with peas and numerical simulations for hard frictional grains. As seen in Figs. 2.4(a-b), the basal force F_b decreases nearly linearly (close to the hydrostatic conditions), and more importantly, the flow rate also decreases gradually during discharge. Another important thing to note is that for hydrogel beads clogging is only observed at much smaller orifice sizes, i.e. the silo discharge is continuous for the relatively small orifice sizes given in Figs. 2.4(a-b), which is in accordance with earlier experimental observations [87].

In order to model the experimentally observed behaviour of soft low friction grains, we performed a systematic numerical (DEM) study by changing the interparticle friction, the Young's modulus Y_m, and the coefficient of restitution of the particles. By adjusting these parameters, the experimental data for hydrogel beads were best reproduced with $\mu = 0.03$, $Y_m = 1.25 \cdot 10^5$ Pa and $e_n = 0.5$ (see Fig. 2.4c-d). First, choosing $\mu = 0.03$ ensures a quantitative match between the experimental and numerical values of the basal force F_b during discharge (compare Figs. 2.4b and d). Second, the numerical flow rate data (Fig. 2.4c) nicely reproduce the experimentally observed linearly decreasing trend qualitatively, but are about 70% higher than the experimental values (Fig. 2.4a). Increasing the Young's modulus and decreasing the restitution coefficient both decrease the flow rate, with the Young's modulus having a stronger effect. For this we use $Y_m = 1.25 \cdot 10^5$ Pa, which is about 3 times larger than the average nominal value. This is in accordance with recent results by Brodu et al. who showed, that when such soft grains have multiple contacts, the resistance of the material against pressure becomes stronger, as deformation of the grain due to the force at a given contact increases the contact force on the other side of the grain [94]. Better match between the flow rates of experiment and simulation could not be obtained, since further increase of Y_m (say by a factor of 2) lead to clogging. The value of $Y_m = 1.25 \cdot 10^5$ Pa results in a typical Hertzian normal deformation of $\delta_n/d \sim (p_b/Y_m)^{2/3} = 10^{-1}$ for a silo with a basal pressure $p_b = 4$ kPa. As said above, changing the value of the restitution coefficient has a smaller effect on the flow rate, the value of $e_n = 0.5$ was estimated from drop and bouncing experiments.

In an attempt to test the effect of friction on hard grains' discharge rates, we performed experiments with two more pairs of samples: clean (dry) and lubricated glass beads (using silicone oil) with diameters of $d = 3.15$ mm and $d = 7$ mm. As described in the experimental section, lubrication reduces the surface friction for certain contacts, and at the same time introduces new effects resulting from cohesive forces. As expected, clean glass beads show very similar discharge characteristics (see Figs. 2.5 (a-b) and (e-f)) to the above described peas. For the lubricated systems, the results are slightly different for the

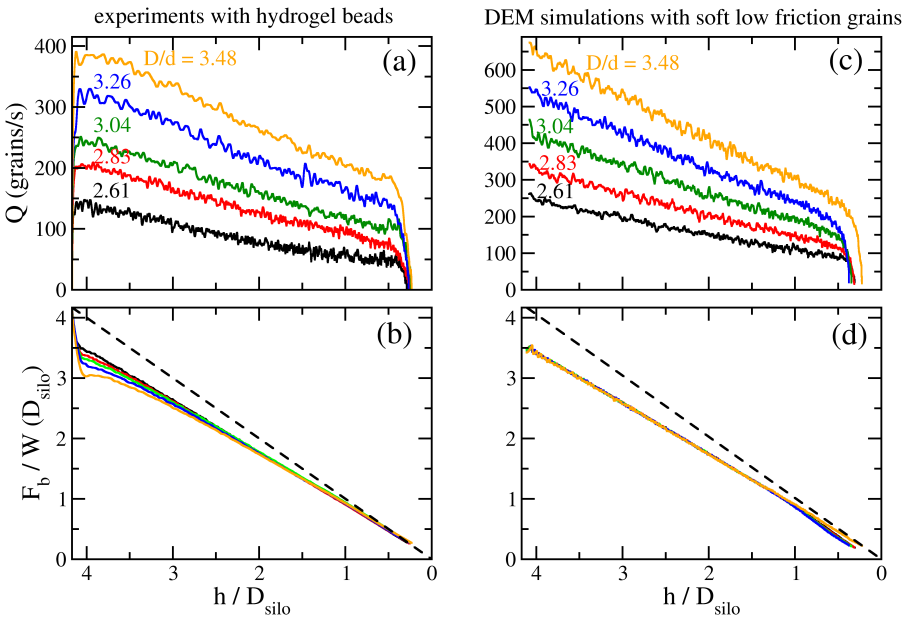

Figure 2.4: Silo discharge of soft low-friction grains: (a-b) experiments with hydrogel beads and (c-d) DEM simulations with spherical grains with friction coefficient of $\mu = 0.03$, Young's modulus of $Y_m = 1.25 \cdot 10^5$ Pa and a restitution coefficient of $e_n = 0.5$. The top panels show the evolution of the flow rate Q while the bottom panels present the basal force F_b in the silo during the discharge process. The value of F_b was normalized by the weight $W(D_{silo})$ of the material corresponding to a filling height of the diameter of the silo. The dashed lines correspond to the hydrostatic condition. Experimental curves represent averages of 10 measurements, numerical data correspond to the average of 4 runs. Geometric parameters: $D_{silo}/d = 15.65$, $h_0/D_{silo} = 4.17, d = 9.2$ mm.

smaller ($d = 3.15$ mm) and larger ($d = 7$ mm) grains. For the small grains, we observed the same flow rates for clean and lubricated systems (compare Figs. 2.5 (a) and (c)), only the basal force was a bit larger for the lubricated system. For the large beads, the discharge rate at a given orifice size is clearly larger for the lubricated system (Fig. 2.5(g)) than for the dry system (Fig. 2.5(e)), but it is still constant in time, like for the small glass beads. Note that for the 7 mm beads, lubrication lead to a much stronger increase of the basal force than for the smaller ones.

2.4.3 Effect of friction coefficient for hard and soft grains: DEM results and coarse-graining analysis

Fig. 2.6 demonstrates how the discharge behaviour changes when the interparticle friction is varied systematically. Two types of particles are examined: hard ($Y_m = 5 \cdot 10^8$ Pa, $e_n = 0.9$) and soft ($Y_m = 1.25 \cdot 10^5$ Pa, $e_n = 0.5$), while all other simulation parameters are kept constant. We see that decreasing friction coefficient leads to a gradual change from the granular-like behaviour with constant flow rate towards a behaviour characterized by a linearly decreasing flow rate. The most important finding is, that this change is much stronger for soft grains (Fig. 2.6b) than for hard grains (Fig. 2.6a),

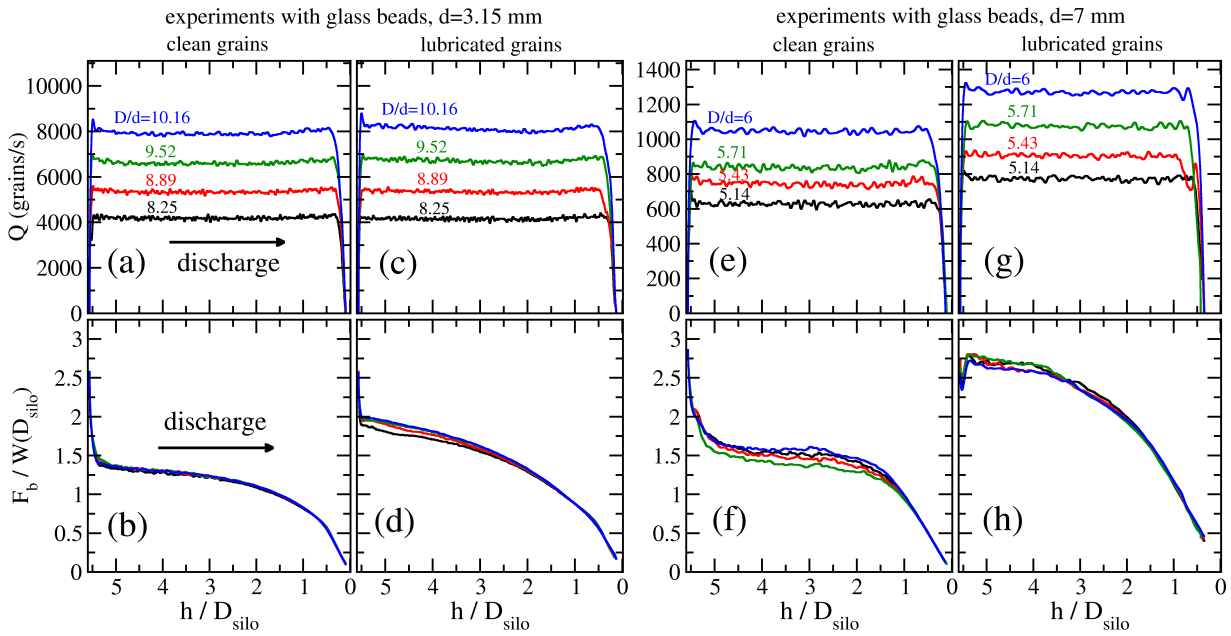

Figure 2.5: Silo discharge with clean and lubricated glass beads of (a-d) $d = 3.15$ mm and (e-h) $d = 7$ mm. Top panels show the flow rate Q while bottom panels correspond to the normalized basal force $F_b/W(D_{silo})$ as a function of height h during the discharge process. All curves represent the average of 4 measurements. Other parameters: $h_0/D_{silo} = 5.56$, $D_{silo}/d = 45.7$ (for beads with $d = 3.15$ mm) and $D_{silo}/d = 20.6$ (for beads with $d = 7$ mm).

even though the curves for F_b do not differ that much for hard and soft grains (compare Figs. 2.6d and e). Thus, for soft grains decreasing interparticle friction leads to noticeable deviation from the granular-like behaviour, while for hard particles such deviation is expected only for frictionless grains. The height dependence of F_b during discharge is similar for hard and soft grains, meaning that the vertical force transmitted to the wall does not depend significantly on the stiffness of the grains. The two experimental scenarios for the lubricated (low friction) glass beads with $d = 3.15$ mm and $d = 7$ mm correspond to the hard grain simulation results with about $\mu = 0.2$ and $\mu = 0.12$, respectively. For frictional beads (e.g. $\mu = 0.5$) the behaviour of hard and soft grains is very similar with a slightly (1.17 times) larger flow rate for soft grains. The effect of the interparticle friction coefficient on the flow rate is summarized in Figs. 2.6(c,f). Panel (c) shows the average value of the flow rate Q (for those cases when it is constant during discharge), while panel (f) shows the net gradient $\langle dQ/dh \rangle \cdot D_{silo}$ of the flow rate (obtained by a linear fit in the range of $D_{silo} < h < h_0$) as a function of μ for both hard and soft grains.

We can extract further data from the DEM simulations, e.g. more information about the stresses inside the silo. For this purpose, we use the coarse-graining methodology, which allows us to build the macroscopic fields of the packing fraction $\varphi(r,z,t) = \rho(r,z,t)/\rho_p$ (particle density ρ_p), velocity $\vec{V}(r,z,t)$ and stress tensor $\sigma(r,z,t)$, with all quantities averaged in the azimuthal direction. Since there is one-to-one correspondence between time and column height, similarly to previous figures we will use the latter instead of the time parameter: $X(r,z,t) \equiv X(r,z,h)$. In the following, we base our analysis on the average of four simulation runs.

It is interesting to calculate the vertical stress σ_{zz} above the orifice, averaged in a cylindrical region

(marked with red in Fig. 2.6i). We normalize σ_{zz} by the hydrostatic pressure $p_h = 4W(D_{\text{silo}})/(D_{\text{silo}}^2\pi)$ corresponding to the weight W of a column of grains with a height of $h = D_{\text{silo}}$, similarly to the normalization of the basal force F_{b}. The evolution of this normalized vertical stress $\tilde{\sigma}_{zz} = \sigma_{zz}/p_h$ is shown in Figs. 2.6g-h. We find a stronger difference in $\tilde{\sigma}_{zz}$ between the case of hard and soft grains compared to the difference observed for the basal force. In fact, the $\tilde{\sigma}_{zz}$ curves change much less with μ for hard grains than for soft grains, just like the flow rate curves. Thus, it is natural to look for correlation between the flow rate and $\tilde{\sigma}_{zz}$. Figures 2.6j-k present the flow rate Q as a function of $\tilde{\sigma}_{zz}$. While the data show a rather weak $Q(\tilde{\sigma}_{zz})$ dependence for hard grains, the increasing trend in $Q(\tilde{\sigma}_{zz})$ is clearly stronger for soft grains. The net gradient of the flow rate $\langle dQ/d\tilde{\sigma}_{zz}\rangle$ (obtained by a linear fit of the curves in Figs. 2.6j-k) is shown in Fig. 2.6l. Thus, for the case of soft grains, (i) the local vertical stress $\tilde{\sigma}_{zz}$ above the orifice changes more during the discharge process and (ii) the value of $\tilde{\sigma}_{zz}$ has a stronger impact on the outflow rate than for hard grains. Both facts (i) and (ii) contribute to the stronger $Q(h)$ dependence observed for soft grains.

Figure 2.7 demonstrates the strong differences in the distributions of the volume fraction, velocity and pressure for soft and hard beads with a friction coefficient of $\mu = 0.03$. For soft beads we present data for two orifice diameters $D/d = 3.04$ and $D/d = 6.5$ corresponding to the data presented in Fig. 2.4 and Fig. 2.6, while for hard beads the data correspond to $D/d = 6.5$. Figures 2.7(a-b) show color-maps exemplifying the volume fraction field $\varphi\,(r,z,h)$ obtained in the simulations, for low friction soft particles ($\mu = 0.03$, $Y_m = 1.25 \cdot 10^5$ Pa and $e_{\text{n}} = 0.5$). Note, these parameters reproduce the experimental flow rate data for hydrogel beads qualitatively (see Figs. 2.4 (c-d)). The color-maps indicate that the volume fraction field $\varphi\,(r,z,h)$ is non-uniform, and in the top region the value of φ resembles the random close packing limit $\varphi \approx \varphi_{\text{RCP}}$. Examining lower regions, the system is more compressed and $\varphi\,(r,z,h)$ increases until it reaches a maximum. Further down, it decreases again upon approaching the orifice. On the other hand, Fig. 2.7(c) hows that the volume fraction field is much more homogeneous for the case of hard grains ($Y_m = 5 \cdot 10^8$ Pa and $e_{\text{n}} = 0.9$). Investigating the color-maps of the velocity field $v\,(r,z,h)$, for soft grains (Fig. 2.7(d-e)) we find that the velocity inside the silo is very uniform, with parallel streamlines. For hard grains (Fig. 2.7(f)) stronger inhomogeneities are observed in the velocity field with lower velocity near the walls and higher velocity in the central part of the silo, leading to a surface distortion (dip) at the top of the granular column. We emphasize again, that the simulations for soft and hard beads were performed with the same friction coefficient $\mu = 0.03$. Finally, Figures 2.7(g-i) display color-maps representing the spatial pressure profile $p(r,z,h)$, obtained using the coarse-grained stress tensor, $p(r,z,h) = \frac{1}{3}Tr(\sigma_{\alpha\beta}(r,z,h))$. The cases for soft and hard grains are very different. The case of soft grains (Fig. 2.7(g-h)) is characterized by a gradual increase of the pressure with depth and relatively small variation in the radial direction. For hard grains (Fig. 2.7(i)) horizontal variations are very strong and the change of pressure in the vertical direction is small in the central part of the silo. Thus, a large fraction of the weight of the granular column is supported by a few layers of grains near the wall. This is the reason for the small variation of the vertical stress $\tilde{\sigma}_{zz}$ right above the orifice during the discharge process (Fig. 2.6(g)). We also note, that the three diagonal components (vertical, radial and tangential) of the stress tensor (not presented here) show larger differences for hard grains, than for low friction soft particles and that our coarse-graining methodology has a limitation in accurately resolving the micro-macro transition near the walls. Thus, for hard grains with a low friction coefficient ($\mu = 0.03$), Janssen screening is still effective, resulting in only a very slight change of the vertical

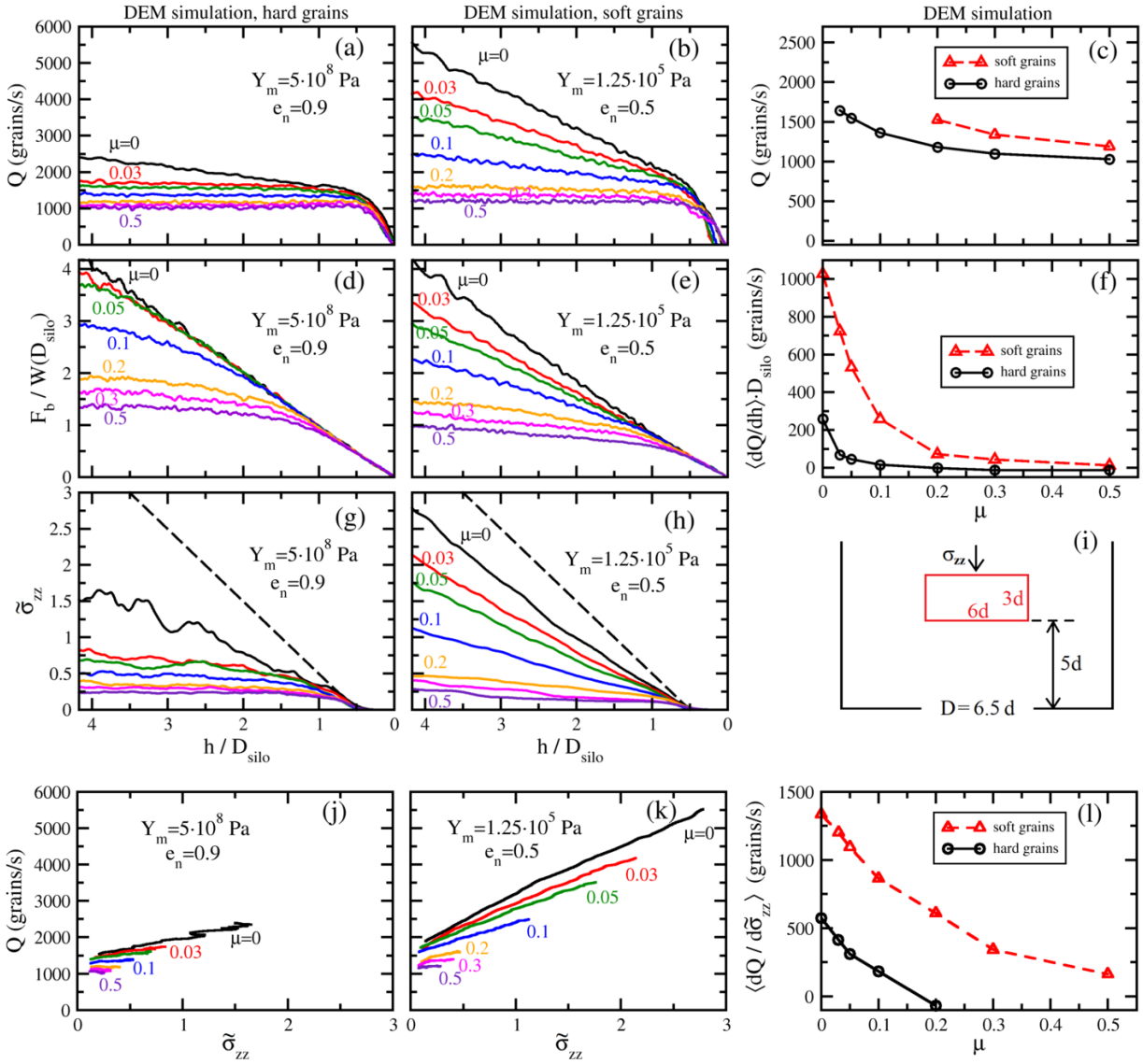

Figure 2.6: DEM simulations of silo discharge for various values of the interparticle friction coefficient μ. Panels (a,d) show the evolution of the flow rate Q and the normalized basal force $F_b/W(D_{silo})$ during discharge of hard particles with a Young modulus of $Y_m = 5 \cdot 10^8$ Pa and a restitution coefficient of $e_n = 0.9$ and (b,e) soft particles with $Y_m = 1.25 \cdot 10^5$ Pa and $e_n = 0.5$. Each curve corresponds to the average of 4 simulation runs. Geometric parameters: $D/d = 6.5$, $D_{silo}/d = 15.65$, $h_0/D_{silo} = 4.17$, $d = 9.2$ mm. (c) Initial constant flow rate and (f) the net gradient $\langle dQ/dh \rangle \cdot D_{silo}$ of the flow rate in the range of $D_{silo} < h < h_0$ from panels (a) and (b) as a function of the interparticle friction coefficient μ. (g-h) The normalized vertical stress $\tilde{\sigma}_{zz}$ measured in the region above the orifice marked with red in panel (i). The dashed line corresponds to the hydrostatic condition. (j-k) The flow rate Q as a function of $\tilde{\sigma}_{zz}$. Panel (l) presents the net gradient $\langle dQ/d\tilde{\sigma}_{zz} \rangle$ for both hard and soft grains.

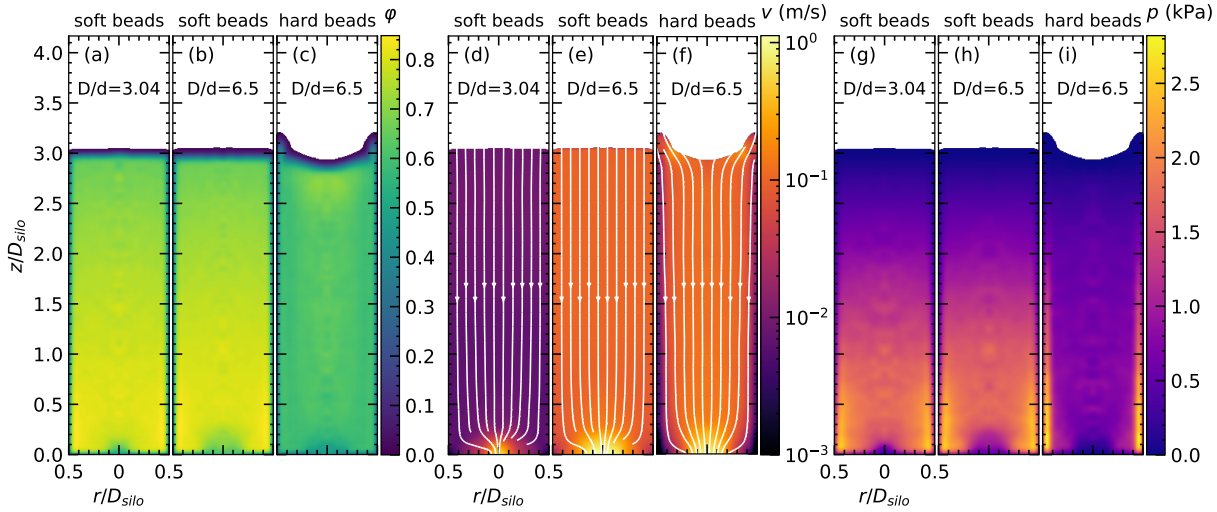

Figure 2.7: Comparison of the discharge characteristics of hard and soft beads with friction coefficient of $\mu = 0.03$: (a-c) color-maps of the volume fraction $\varphi\,(r,z,3D_{\text{silo}})$, (d-f) the velocity field $v\,(r,z,3D_{\text{silo}})$ and (g-i) spatial pressure profile $p(r,z,3D_{\text{silo}}) = \frac{1}{3}Tr(\sigma_{\alpha\beta}(r,z,3D_{\text{silo}}))$, obtained using the coarse-graining methodology. Panels (a-b, d-e, g-h) correspond to the discharge of soft, while (c, f, i) to the discharge of hard particles with orifice sizes of $D/d = 3.04$ and 6.5, as indicated on the plots. Note that the state shown here for soft grains with small orifice size ($D/d = 3.04$) corresponds to the red curves in Fig. 2.8 and the color-maps for large orifices ($D/d = 6.5$) were obtained for the same parameters as the corresponding red curves of Fig. 2.6(a-b). In the computation, we use a truncated Gaussian coarse-graining function $\phi(\vec{r})$ with coarse-grained scale $w = d/2$. In all graphs, z and r are rescaled with the diameter of the silo D_{silo}. We use white color in all color-maps where the packing fraction is less than a cutoff value of 1%.

stress above the orifice during the discharge process. This explains why the flow rate correlates with $\tilde{\sigma}_{zz}$ but not with F_b for the case of hard grains.

The above described observations are in accordance with previous experimental investigations which also revealed strong differences in the flow field between the case of plastic and hydrogel beads using X-ray Computed Tomography [86, 87]. There the vertical velocity inside the 3D silo was found to be more homogeneous for low-friction soft hydrogel beads than for hard frictional plastic beads, and a decrease of the flow velocity was also observed with decreasing filling height using Ultrafast X-ray Computed Tomography [87]. Altogether, our current numerical data for the pressure distribution $p(r,z,h)$ for the case of soft grains with weak pressure change in the radial direction and a smooth pressure change along the symmetry axis of the silo allows us to perform some further analysis. Namely, $p(r,z,h)$ gradually increases from the top of the bed along the symmetry axis, it has a maximum close to the orifice, and further down it decreases rapidly (see the color map at Figs. 2.7(g-h)), forming a measurable vertical pressure gradient right above the orifice. In the following, we will look for a correlation between the flow rate and this pressure gradient.

2.4.4 Connection between the flow rate and pressure gradient near the outlet for soft, low-friction particles

Aiming to explain the system's macroscopic response, in terms of its micro-mechanical properties, Fig. 2.8 focuses the attention on the profiles of $\varphi(z,h) \equiv \varphi\,(r{=}0,z,h)$ and $p(z,h) \equiv p(r{=}0,z,h)$ along the vertical direction, for soft grains with $\mu = 0.03$ at the center of the silo with an orifice of $D = 3.04d$. The data illustrated in Fig. 2.8 result from a spatial average within a cylindrical region of one particle diameter in size, and they were obtained at different instants in time, corresponding to subsequent stages of the discharge process. Figure 2.8(a) shows the profiles of the volume fraction $\langle\varphi\,(z,h)\rangle$. In the top region, the volume fraction always reproduces the random close packing value. These linear sections are simply shifted with respect to each other, which shows that the density increases linearly with the depth, denoting the compression of the system. However, density gradient remains practically invariant during the whole discharge process. In all cases, the mass density shows a maximum close to the orifice, but its value drops as time passes and the column gets shorter. Moreover, further down the dilatancy of the flow becomes evident, the volume fraction is reduced, and at the orifice, $\varphi(0,h)$ depends on the column height h. A very similar trend appears for the mean pressure profiles $\langle p(z,h)\rangle$ computed at different instants in time (see Fig. 2.8(b)). Starting from the column surface the pressure increases hydrostatically with depth, and reaches a maximum value $p_m(h)$ at a certain vertical distance $L(h)$ from the orifice. Note that the pressure in the center of the orifice $p(0,h)$ is nonzero, since the particles are still compressed at that point.

In order to address the forces acting on a representative volume element at the orifice, we fitted 6th order polynomials to the pressure profiles $\langle p(z,h)\rangle$ along the vertical direction (Fig. 2.8(b)). Then, we located the distance of the maximum $L(h)$ from the orifice position, as well as the maximum pressure $p_m(h)$ (red dots) on these smoother curves, as a function of the column height h (shown in Fig. 2.9(a)). The pressure gradient at the orifice was estimated, using a linear approximation, by $\frac{\Delta p}{L}(h) = (p_m(h) - p(0,h))/L(h)$. Two interesting things deserve to be commented here. First, during a large part of the discharge process, the position $L(h)$ of the maximum pressure does not depend on the column height (see inset of Fig. 2.9(a)). Accordingly, the pressure gradient at the orifice (see Fig. 2.9(b)) decreases linearly. Later on, however, finite size effects become more significant.

The coarse-grained continuous fields allow us to perform a theoretical analysis, to predict the linearly decreasing flow rate that was obtained numerically for low friction soft particles and experimentally for hydrogel beads (see Fig. 2.4). Our arguments rest on the momentum balance that is established in steady state conditions at the orifice, where the sum of the pressure gradient $\frac{\Delta p}{L}(h)$ and the density of body gravitational force $\rho_p\varphi(0,h)g$ are balanced by the beads' resistance to motion. Thus, assuming that the system acts like a viscous fluid in having a linear response to forcing, the mean vertical velocity at the orifice can be predicted as

$$v_z(D,h) = K(D)\left(\frac{\Delta p}{L}(h) + \rho_p\varphi(0,h)g_z\right), \tag{2.8}$$

where $K(D)$ is a hydraulic coefficient that increases with decreasing effective viscosity of the system and increasing permeability of the orifice region. Thus, the mass flow rate at a circular orifice of size

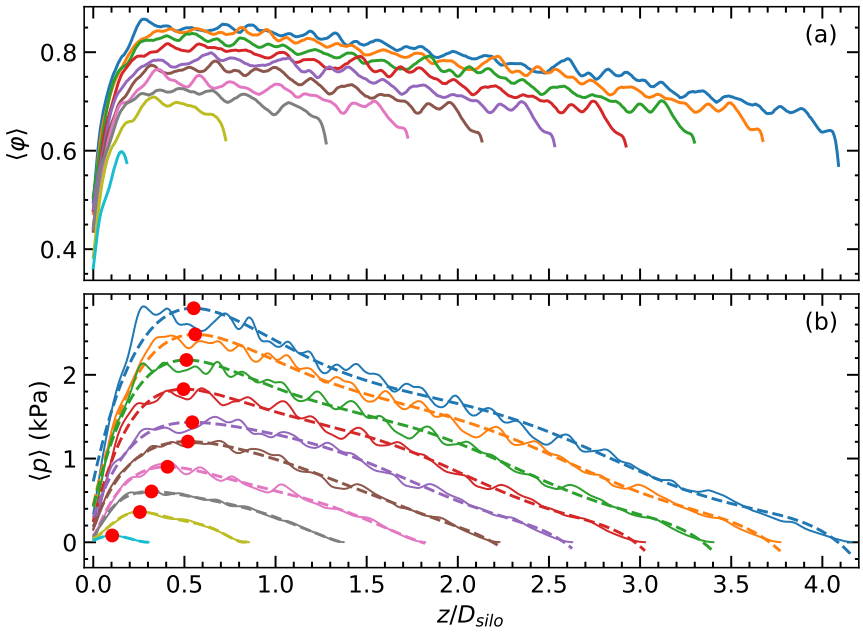

Figure 2.8: The profiles of (a) mean volume fraction $\langle \varphi\,(z,h)\rangle$ and (b) mean pressure $\langle p(z,h)\rangle$ obtained along the middle vertical slice of the silo. The curves correspond to successive instants of the discharge process. In both graphs, z is rescaled with the diameter of the silo D_{silo} and the relative size of the orifice is $D/d = 3.04$. In each case, the height of the column is given by the last point of the curve, approximately. In panel (b), dashed curves are the 6th order polynomial fits for the corresponding mean pressure (solid), while the red dots mark the maxima of these fits.

D reads

$$Q(D,h) = \rho_p \varphi(0,h) A_c v_z(D,h) = \rho_p \varphi(0,h) \pi \frac{D^2}{4} K(D) \left(\frac{\Delta p}{L}(h) + \rho_p \varphi(0,h) g_z \right). \tag{2.9}$$

Figure 2.10 compares the linearly decreasing trend of the flow rate with height, obtained numerically for low-friction soft particles, with the theoretical prediction of Eq. (2.9). Moreover, the inset of Fig. 2.10 shows the estimate of the hydraulic parameter $K(D)$, which is the only fitting parameter used in the analysis. The agreement of the comparison is remarkable, especially during the first part of the discharge process, where the position $L(h)$ of the maximum pressure does not depend on the column height (see inset of Fig. 2.9(a)) and the pressure gradient depends linearly on the column height. Besides, we found that $K(D)$ increases with increasing orifice size. Note, the value of $K(D)$ should be proportional to the permeability of the orifice and inversely proportional to the effective viscosity of the material. The appearance of a linear response – when the friction is low – could be a natural consequence of the local interactions between the particles. Namely, for deformable particles with low friction viscous normal damping has a more important role in energy dissipation than tangential frictional displacement, and the macroscopic shear stress is proportional to the relative velocity of the neighboring particles, and so indirectly to the shear rate. Our analysis notably sheds light on the nature of the flow of a granular material consisting of soft low-friction particles. Indeed, its behavior is remarkably different from the

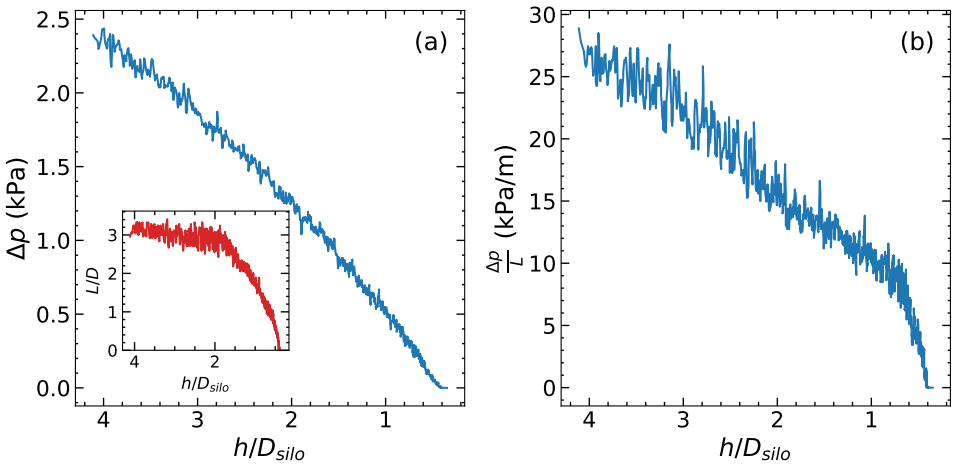

Figure 2.9: (a) Example of the pressure drop $\Delta p(h) = p_m(h) - p(0,h)$ near the orifice as a function of the column height h. In the inset, the location of the maximum $L(h)$ respective to the orifice position is plotted as a function of the column height. In (b), the estimation of the pressure gradient $\frac{\Delta p}{L}(h)$ at the orifice as a function of the column height is shown. All data obtained for the orifice diameter $D/d = 3.04$.

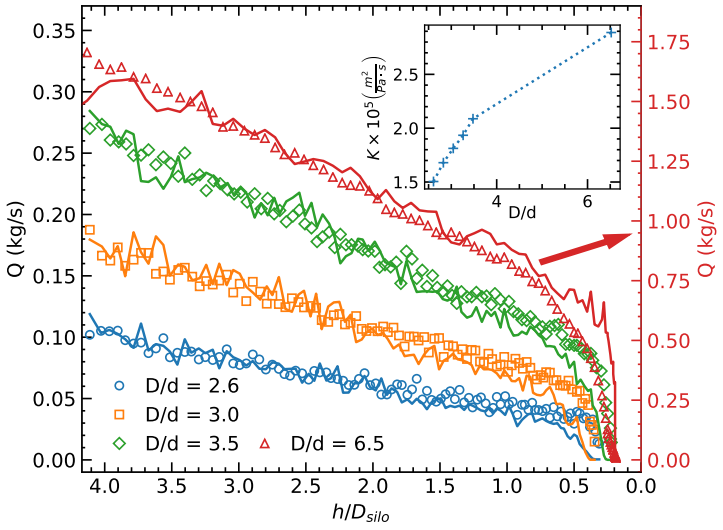

Figure 2.10: Evolution of the flow rate Q obtained numerically with particles of $\mu = 0.03$, $Y_m = 1.25 \cdot 10^5$ Pa, and $e_n = 0.5$ (symbols), for various values of the orifice diameter D. The bed height h is rescaled with D_{silo}. The numerical data are compared with the prediction of Eq. (2.9) (lines), where the pressure gradient $\frac{\Delta p}{L}(h)$ and the volume fraction $\varphi(0,h)$ at the orifice are derived from the coarse-grained fields. Inset: the hydraulic coefficient K as a function of orifice diameter D/d. In the main figure, the y-axis labels at the right correspond to the data for $D/d = 6.5$ (red), those at the left refer to the other three datasets.

'traditional' granular discharge, where, at the orifice, the pressure gradient is practically constant during the discharge process and, as a result, the volumetric flow rate does not depend on the column height [74].

2.5 Summary

Our experimental and numerical investigations clearly show that changing particle stiffness has a strong effect on gravity driven granular flow out of a container with a small outlet in the flat bottom. Namely, decreasing the interparticle friction has much stronger effect for soft grains than for hard grains. For *soft grains*, with Young's modulus of the order of 10 times the basal pressure, numerical simulations predict that the character of the discharge process gradually changes with decreasing interparticle friction: Grains with high friction coefficient flow with a constant flow rate (granulate-like behaviour), while for grains with low surface friction, the flow rate systematically decreases with the height of the granular bed. This is noticeably different for *hard grains*, with Young's modulus of the order of 10^5 times the basal pressure, where basically a constant flow rate is observed except for the special limit case of frictionless grains. This is nicely demonstrated by the effect of lubricating the glass beads, where reducing the friction coefficient already resulted in a gradual decrease of the basal force during discharge, but the constant flow rate still persisted (traditional granulate-like behaviour). For frictional grains, the difference between the discharge of hard and soft particles is smaller. Both cases are characterized with a constant flow rate, which is only slightly larger for soft grains. This is in accordance with earlier findings [82], where for frictional grains ($\mu = 0.6$), a moderate change in the stiffness (typically 1 order of magnitude) lead to no significant change in the flow rate. The evolution of the total normal force exerted at the bottom of the container during discharge shows much smaller differences between hard and soft grains.

Using DEM data combined with a coarse-graining methodology allowed us to compute all the relevant macroscopic fields, namely, linear momentum, densities and stress tensors. Such analysis reveals a considerably different pressure field for hard and soft grains with low friction coefficient. For low friction hard grains, Janssen screening is still observed with increased vertical stress near the walls, while for low friction soft grains this effect is much weaker. For low friction soft particles the local vertical stress above the orifice changes more during discharge, and it has a stronger effect on the flow rate, than for low friction hard grains. Thus, dynamic arch formation which is a key element in setting a constant flow rate for hard grains is much less effective for low friction soft grains. The fact that the critical orifice size below which clogging is observed was found to be much smaller for low friction soft grains [83–85] is in accordance with the above described observations. For low friction soft grains, instead of the Janssen screening, the pressure inside the silo is linearly increasing with distance from the top surface and has a maximum right above the orifice. The value of this pressure maximum gradually decreases during the discharge process, and can be related to the decreasing discharge rate. Based on the momentum balance in the region of the orifice, we propose a phenomenological formulation for soft particles with low friction coefficient. This suggests that for such materials, dissipation is dominated by viscous friction near the orifice. This model predicts a very similar decrease of the flow rate with decreasing fill height as found in our experiments with hydrogel beads. We note, that incorporating a multiple-contact approach (such as in Ref. [94]) to the DEM simulations is expected to further improve

the quantitative match between experiment and simulation data, which might be the subject of future work.

Acknowledgements

The authors acknowledge discussions with A. Ashour and V. Kenderesi. Financial support by the European Union's Horizon 2020 Marie Skłodowska-Curie grant "CALIPER" (No. 812638), by the NKFIH (Grant Nos. OTKA K 116036 and 134199), by the DAAD/TKA researcher exchange program (Grant No. 274464), and by the BME IE-VIZ TKP2020 program is acknowledged. R.C. Hidalgo acknowledges the Ministerio de Economía y Competitividad (Spanish Government) Projects No. FIS2017-84631-P, MINECO/AEI/FEDER, UE.

Chapter 3

Silo discharge of mixtures of soft and rigid grains

Jing Wang*, Bo Fan*, Tivadar Pongó*, Kirsten Harth, Torsten Trittel, Ralf Stannarius, Maja Illig, Tamás Börzsönyi, Raúl Cruz Hidalgo

*shared first authorship

Soft Matter **17** 4282 (2021) DOI: 10.1039/D0SM01887B

We study the outflow dynamics and clogging phenomena of mixtures of soft, elastic low-friction spherical grains and hard frictional spheres of similar size in a quasi-two-dimensional (2D) silo with narrow orifice at the bottom. Previous work has demonstrated the crucial influence of elasticity and friction on silo discharge. We show that the addition of small amounts, even as low as 5%, of hard grains to an ensemble of soft, low-friction grains already has significant consequences. The mixtures allow a direct comparison of the probabilities of the different types of particles to clog the orifice. We analyze these probabilities for the hard, frictional and the soft, slippery grains on the basis of their participation in the blocking arches, and compare outflow velocities and durations of non-permanent clogs for different compositions of the mixtures. Experimental results are compared with numerical simulations. The latter strongly suggest a significant influence of the inter-species particle friction.

Highlighting research from the CALIPER consortium groups (www.caliper-itn.org) of Prof. Ralf Stannarius, Magdeburg, Dr Tamás Börzsönyi, Budapest, and Prof. Raúl Cruz Hidalgo, Pamplona.

Silo discharge of mixtures of soft and rigid grains

Study of silo discharge of elastic granular particles and of their mixtures with rigid particles of the same shapes and sizes. Both experimental investigations and numerical simulations are presented. The viscoelastic properties of the grains generate qualitatively new features in the flow characteristics and clogging behaviour.

As featured in:

See Ralf Stannarius *et al.*, *Soft Matter*, 2021, **17**, 4282.

ROYAL SOCIETY OF CHEMISTRY

rsc.li/soft-matter-journal

Registered charity number: 207890

3.1 Introduction

Storage of granular materials in silos and hoppers has an evident advantage over other containers for the processing of these materials in agriculture, chemical industry, construction industry and many other branches: Material is stowed into the container through a top orifice, yet it can be withdrawn from the storage device through an orifice at the bottom simply using gravity forces. No additional mechanical device is needed to maintain the outflow. However, one of the problems with these storage bins is congestion of the orifice, so-called clogging, which can occur even if the orifice diameter is much larger than the largest spatial extension of the individual grains. Particles can form stable arches (in 2D) or domes (in 3D) above the outlet and block further outflow. Intervention from outside is required to re-trigger discharge. From a physical point of view, this process is insufficiently understood even today, despite of hoppers being in use for millenia in human history. The flow of grains, even in the simplest form of hard monodisperse spheres, has retained many mysteries. Even the simplest problem of the outflow of monodisperse ensembles of spheres is still an active field of research. Through large enough orifices, such grains flow at constant rates given by geometrical and physical parameters. Flow rates have been derived from theoretical models [20, 44, 51, 69] and the predictions were tested in numerous experiments (e.g. [21, 51, 58, 76, 95, 96]). When the outlet diameter is small (less than about 5 particle diameters) [25, 97, 98], hard spheres tend to form clogs after some time at the orifice. These block further outflow until they are destroyed by shaking the container, by applying air flushes or by other mechanical disturbances. Spontaneous arch formation [99, 100], the preceding kinetics [74], as well as the inherent force distributions [101, 102] have been analyzed in the literature. Identical hard spheres are an idealized special system that has been considered in most of the experimental and theoretical studies. Since there are no principal differences between clogging of 2D and 3D silos, the former are often preferred in experiments because they offer the study of the inner dynamics and structure formation in the container with non-invasive observation methods.

Recently, it was found that soft particles with low friction differ considerably from common hard, frictional grains in their static and dynamic behavior in silos [83, 84]. The critical ratio ρ of orifice size and particle size below which clogging sets in is much smaller than for rigid grains. In addition, non-permanent, intermittent clogs are observed which spontaneously dissolve after some time. Such features are otherwise observed only in vibrated silos [29, 103], in colloidal systems [104–106] or in active matter [100]. In the earlier experiments with soft, slippery hydrogel grains, it remained unexplained whether the softness of the particles (elastic modulus of the order of a few dozen kPa) or the low friction coefficient (in the order of 0.03), or a combination of both causes the quantitative differences to hard, frictional grains. Previous work on pure monodisperse hydrogel sphere (HGS) ensembles [85] has identified the viscoelastic properties of these spheres as one important feature that causes qualitatively new features of the discharge through narrow orifices.

In practice, homogeneous granular ensembles are often the exception, even in industrial processes. One usually deals with materials that are non-uniform in size, shape, surface structure, or other properties. This motivated us to study mixtures of particles that differ in their elastic and frictional properties but are otherwise very similar. It turns out that an addition of even small portions of rigid particles to HGS ensembles has dramatic influence on silo discharge behavior.

This paper describes an experimental and numerical study of the effects of doping soft HGS ensem-

bles with hard, frictional particles of the same size and weight. We will add up to 10 % of the latter to the pure hydrogels and focus on three aspects:
(1) What is the influence of doping on the silo discharge characteristics?
(2) How is the concentration x_{hf} of hard grains in the mixture represented in the composition of the blocking arches? This will allow us to extract the probabilities that hard or soft grains complete a blocking arch and cause clogging.
(3) Does the composition of the mixtures affect the outflow rates?

A quasi-two-dimensional setup with one layer of beads between two vertical glass plates is used. The mass of the discharged material is recorded by means of a balance beneath the orifice. Particle arrangements and flow inside the container are monitored by video imaging. In addition, numerical simulations are performed and compared to the experiment.

3.2 Experimental setup and materials

The setup consists of a flat container of 80 cm height, 40 cm and slightly more than 6 mm depth. In the images shown in Fig. 3.1, vertical aluminum rails that support the front and rear glass plates hide 3 cm of the container interior on the left and right sides. Only 34 cm are visible. At the bottom, a rectangular opening of variable width can be adjusted with two horizontal sliders.

The container is filled with a mixture of soft, low-friction hydrogel spheres and hard frictional (HF) plastic airsoft ammunition. The concentration of HF plastic grains is low, typically 5% or 10%. We define the aspect ratio ρ as the quotient of the orifice D and the particle diameter d. In the present study, this ratio is in the range $1.7 < \rho < 2.2$. We note that at such small orifice sizes a pure sample of hard frictional grains would almost immediately clog. At large enough orifice sizes ($\rho > 3$), the behaviour of our mixtures is practically identical to the pure hydrogel samples.

Both species have densities of approximately 1020 kg/m^3. The 6 mm diameter airsoft beads were obtained from commercial providers. They are made from plastic, are perfectly monodisperse and they are hollow. The latter feature is irrelevant here. The friction coefficient of the airsoft beads is 0.3. They are incompressible and can be considered rigid. The hydrogel spheres were obtained in dried state from a commercial provider (*Happy Store, Nanjing*). They were swelled in salted water with a NaCl concentration that determined the final radius of approximately 6.5 mm, with a polydispersity of about 3 %. The mass of each hydrogel sphere is about 0.15 g. They have a friction coefficient one order of magnitude lower than the HF spheres, but the elastic modulus is of the order of only 50 kPa to 100 kPa. These particles are incompressible as well, but they deform slightly in the silo under the weight of the overlying grains (see Fig. 3.1, bottom). A rough estimate is that the Hertzian contacts between hydrogel spheres at the bottom of the container indent the grains by approximately 1.3 mm under the weight of the full silo.

The 2-dimensional (40 x 80 cm) cell can accommodate about 10,000 grains corresponding to a weight of ≈ 1.5 kg. The cell is extended at the top with an additional 3-dimensional container, which can hold extra granular material.

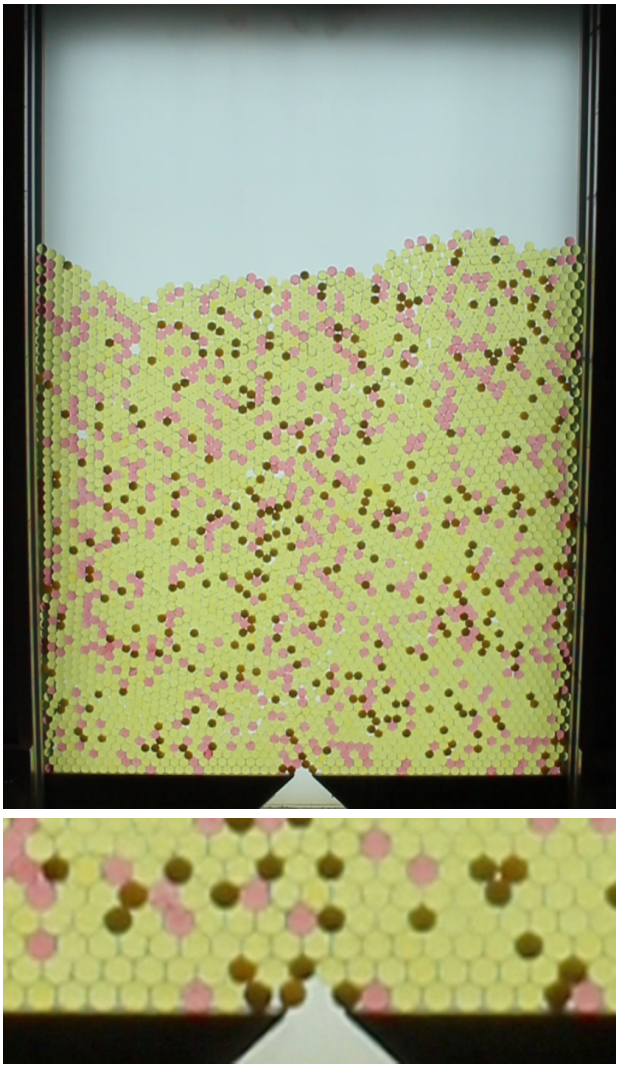

Figure 3.1: Top: Image of the container filled with a mixture with 10 % hard frictional beads. Yellow and pink colored hydrogel spheres are equivalent, airsoft bullets appear dark. Bottom: Zoom into the region near the orifice at the bottom, in a clogged state. The orifice in these images is $D = 11$ mm, slightly less than two particle diameters.

3.3 Avalanches and clogging probabilities

Avalanche sizes are a key figure of merit for silo discharge. Figure 3.2 shows an example of the discharged mass curve for a mixture of hard and soft spheres, filled into a silo with a narrow orifice. Plateaus in this curve either represent non-permanent interruptions of the flow that dissolve spontaneously, or clogs that were destroyed by air flushes (arrows).

The mean number of grains discharged during an avalanche is directly related to the probability that a particle completes a blocking structure at the orifice. In the geometry we use in our experiments, with ρ of the order of 2, these clogs are formed by very few grains, four on average. Thus, the experiment provides favorable conditions to observe the microscopic dynamics (on the particle level) at the opening, and on the other hand, the choice of the soft hydrogel material guarantees the formation of comparably

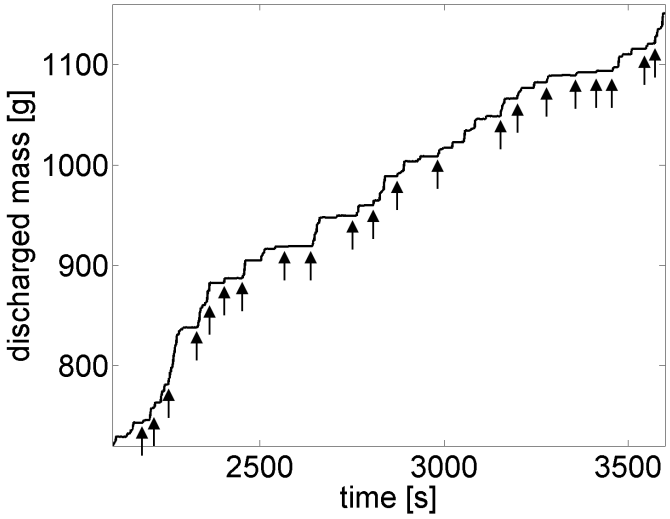

Figure 3.2: Part of a measured time dependence $m(t)$ of the mass of granular material discharged from a quasi-2D silo. The mixture contained 10 % of rigid air soft balls with 90 % hydrogel spheres, both with 6 mm diameter. The orifice size was 11 mm. Some clogs (plateaus) dissolved spontaneously, clogs labeled by arrows were destroyed by an air flush through the orifice.

large avalanches for a reasonable statistics at these small aspect ratios. The relation between the probability of particles completing a clog at the outlet and the size of avalanches is given in Appendix A.

In the experimental determination of avalanche sizes, one encounters a problem which is related to a peculiar feature of the hydrogels identified already in the pure system [85]: The soft, viscoelastic material has the tendency to form interruptions of the outflow that can dissolve spontaneously after some time, particularly for small orifice sizes. In Figure 3.2, some plateaus indicate non-permanent interruptions of the flow that dissolve spontaneously. There is no clear criterion to discriminate the end of an avalanche and the beginning of a non-permanent clog from mere fluctuations of the outflow rate. If one analyzes the time delays between subsequent grains passing the orifice, there is no obvious threshold that may serve to identify and mark non-permanent clogs, and distinguish them from fluctuating outflow. Short interruptions of the outflow are continuously distributed. Technically, it is therefore justified to regard an outflow process as one single avalanche, unless a permanent clog is reached. In Fig. 3.2, the nearly 3 minute period after the air flush at $t = 2980$ s represents an example of an avalanche that has intermittent non-permanent breaks.

For practical reasons, one may nevertheless be interested in the distribution of phases where the material is flowing and phases where the outflow is interrupted. This is the standard procedure for the description of living or externally agitated systems (e. g. [107]). Thus, we introduce an *ad hoc* criterion, the interruption of the outflow lasting one second or longer, to separate avalanches. However, it was shown earlier that the arbitrary selection of a threshold may influence the statistics considerably [105]. Since we treat all mixtures with the same model, our arbitrary choice of the threshold may be still justified.

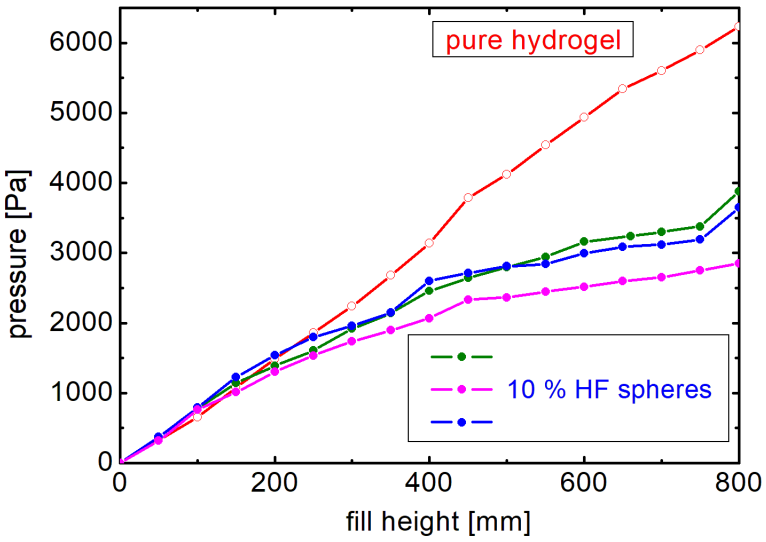

Figure 3.3: Pressure at the bottom of the container at the position of the outlet for pure hydrogel system (open circles), and three independent measurements of a mixture with 10% HF spheres (filled circles) (cf. numerical simulation data in Fig. 3.16). Lines guide the eye.

3.4 Experimental results

3.4.1 Pressure characteristics

It was shown earlier that the low-frictional hydrogel shows an almost hydrostatic characteristics $P(h)$ of the pressure P at the bottom of a quasi-2D container filled up to a height h [83]. In contrast, the hard, frictional grains exhibit the typical saturation of the pressure [18] at a fill height of several cm [83]. Figure 3.3 shows that the pressure characteristics of the pure hydrogel sample is changed significantly by addition of a small amount x_{hf} (10 %) of HF spheres. The pressure in the mixtures clearly deviates from hydrostatic behavior. The data were obtained by measuring the force on a short (4 cm) horizontal bar that replaced part of the bottom container border. The weight of the material in upper layers is at least partially transferred to the container walls. The pressure characteristics differ slightly in individual runs, but the general trend is seen in all three graphs. This continuous pressure increase with fill height has direct consequences for the discharge characteristics of the mixtures, as will be demonstrated below.

One consequence of the increasing pressure towards the bottom of the silo in combination with the low elastic modulus of the hydrogels is that the packing fraction ϕ increases towards the bottom. The closest packing of spheres with diameter d in a quasi-2D hexagonal lattice within a layer of thickness d is $\phi_{\mathrm{max}} = \pi/\sqrt{27} \approx 0.604$. This is indeed the mean packing fraction of pure hydrogel spheres, since they form a nearly defect-free hexagonal lattice in the depth of the granular bed. At the bottom, they even reach packing fractions up to about 0.65 where they are squeezed out of their original sphere shape. In the very top layers, owing to imperfections, the packing fraction drops to about 0.5. This may

have some consequences for the outflow rates discussed in the next section.

3.4.2 Flow rate and clog duration

Fig. 3.4a demonstrates how the character of the outflow is altered by changing the size of the orifice for a given mixture. One can see that the material flows practically uninterrupted through the largest orifice, with 13 mm width, until the fill level has lowered to about 20 ... 25 cm. In the silo with 12 mm orifice width, clogs interrupt avalanches of the order of 100 g (nearly 1000 particles), while in the silo with 11 mm opening, avalanches are on average one order of magnitude smaller. The fill-height dependence of the occurrence of plateaus (non-permanent clogs) in the graphs is the consequence of a pressure-dependent blocking probability of individual soft grains passing the outlet, see Appendix A.

The presence of a small fraction of hard frictional particles influences the outflow dynamics by having an impact on the statistics of clogs (permanent or non-permanent) as well as on the flow rate between clogs. The outflow curves are shown in Fig. 3.4(b) for 3 samples with hard frictional sphere contents x_{hf} of 0, 0.05 and 0.1. The orifice width was $D \approx 11.5$ mm. The flow rate (between clogs) depends on the composition of the sample (fraction of HF spheres) and other parameters, such as the filling height and orifice size. We will further investigate the dependence of the flow rate as well as the duration of non-permanent clogs on the number of HF spheres in the proximity of the orifice.

For a visualization of the evolution of the flow rate (during avalanches) during the whole discharge process, Fig. 3.4(b) was trimmed by removing all clogs longer than 1 s. The result is shown in Fig. 3.4(c). The local slope of these curves gives the instantaneous discharge rate at any moment. This rate is shown in Fig. 3.5(a) as a function of the bed height h. In accordance with our earlier observations in a 3D silo [87], the flow rate for pure hydrogel decreases with decreasing filling height. For the sample with 5 % HF grains, the height dependence is much weaker, while for the sample with 10 % HF grains this trend has essentially vanished. Thus, adding a small amount of frictional hard beads to a hydrogel bead ensemble has a strong effect on the discharge kinetics of a 2-dimensional silo. Increasing the concentration of frictional hard grains, we quickly recover the typical behavior of granular materials characterized by a height independent (constant) flow rate.

It is obvious that Beverloo's original equation that relates the geometry of the particles and outlet to the discharge rate is not exact for the hydrogels and at least the 5 % HF spheres mixture since their discharge rates depend upon pressure at the outlet. Here, the low friction coefficient of the hydrogel may play a role [75], but the primary cause is the pressure dependence caused by the grain elasticity. Astonishingly, addition of 10 % of rigid grains fully removes this pressure dependence.

For an analysis how the flow rate depends on the orifice size D, and for comparison of all three mixtures, we present data of the height range between 40 cm and 45 cm in Fig. 3.5b. As expected, the flow rate W decreases with D. An increased concentration of hard grains clearly reduces the flow rate, particularly at small orifice sizes. A dependence as predicted by Beverloo's model in 2D, $W = C\phi\rho_0 h\sqrt{g}(D - kd)^{1.5}$, with the grain diameter d, the density ρ_0 of the grains, packing fraction ϕ, cell thickness $h \approx d$ and adjustable constants k and C may be fitted for all three samples, but this is not surprizing because of the small D/d range and the free parameters k and C. The product $\rho_0\phi h$ amounts to approximately 3.7 kg/m^2. From Fig. 3.5b, one finds $k \approx 1.6$, which is larger than the commonly reported value of about 1.4. The constant C to fit the graphs in Fig. 3.5b ranges from 3.5 for

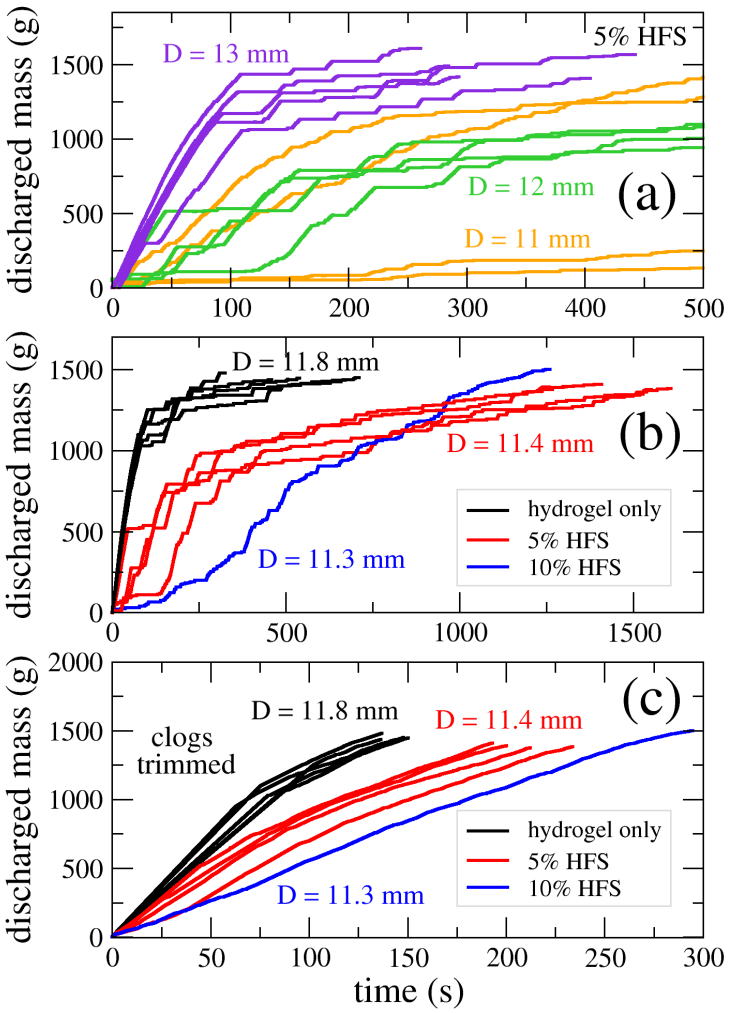

Figure 3.4: (a) Time dependence of the discharged mass for a sample containing 5% hard frictional spheres (HFS) for 3 values of the orifice width D. It is evident that the probability of clogging increases strongly with lower ratios of orifice width to particle diameter. (b) Time evolution of the discharged mass for 3 different samples: pure hydrogel, and mixtures containing 5% or 10% HF spheres. The orifice size D is indicated on the figure. The horizontal sections correspond to the clogs. (c) Same data as panel (b) but with clogs longer than 1 s trimmed. The flow rate is measured as the local slope of these trimmed curves.

the 90 % sample to about 6 for the pure hydrogels. This proportionality factor C accounts, for instance, for details of the orifice geometry. Considering Fig. 3.5a, one has to conclude that this factor depends upon the instant fill height, viz. the pressure at the container bottom, in the pure hydrogel and the 5 % HF spheres samples. This is also evident from the flow rate of the pure hydrogel sample as a function of D for three different height ranges, shown in Fig. 3.5(c).

Next, we analyze the dependence of the flow rate on the number of HF grains in the vicinity of the orifice. We consider a region with the shape of a half circle with a radius of 5 d above the orifice. For large bed heights ($h > 37.5$ cm) the flow rate is clearly decreasing when we have more than 3 hard grains in this region, i. e. the presence of hard, frictional grains near the bottleneck has a noticeable

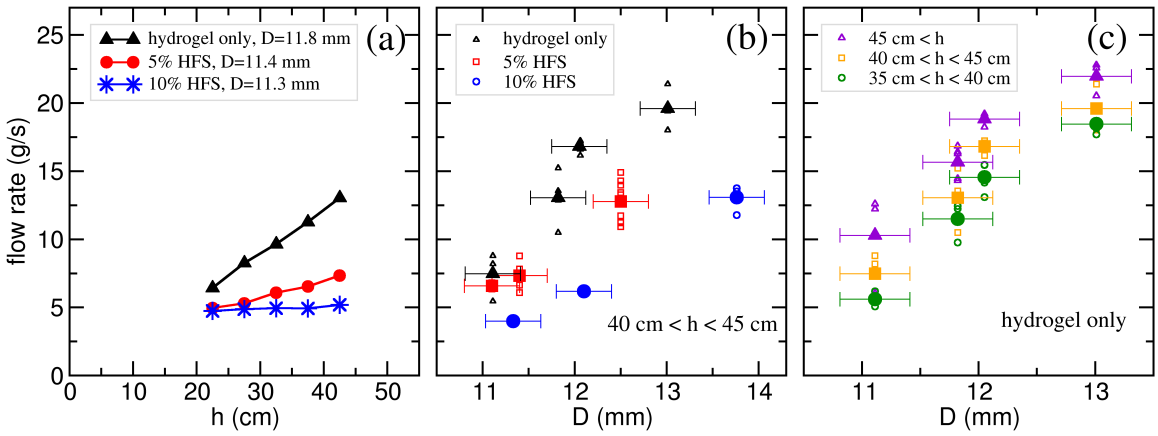

Figure 3.5: (a) Flow rate as a function of the bed height h for pure hydrogel and for mixtures with 5% and 10 % HF spheres. (b) Flow rate as a function of orifice size D for all 3 samples for a bed height of 40 cm $< h <$ 45 cm and for (c) pure hydrogel samples at various bed heights h. Small open symbols represent individual experiments, large filled symbols show averages of the respective data sets (on average 4 experiments).

effect on the outflow (see Fig. 3.6). For $h < 37.5$ cm, no such decrease was detected. When the pressure at the bottom is already very low, the addition of hard grains has little effect on the outflow dynamics. The explanation is straightforward: the elasticity of the hydrogel plays a role primarily when there is high pressure at the orifice. When the silo is filled by a 40 cm high granular bed, the pressure is approximately 3 kPa, and this pressure can deform the soft particles at the orifice by roughly 10 % of their diameter. When the fill height and consequently the pressure lowers, the deformations are much less intense and the hydrogels gradually approach the mechanical properties of still low-frictional but hard grains.

3.4.3 Non-permanent clogging

Similar to earlier observations with pure hydrogel sphere ensembles [85], the system shows non-permanent clogging. This is seen, for example, in the mass curve shown in Fig. 3.2. The plateaus are signatures of stopped outflow. In the experiment shown, with 11 mm orifice size and the silo emptied to about one fourth, roughly every second congestion of the orifice ends spontaneously, without external interference by air flushes or other. The reason for that is identified in the viscoelastic properties of the hydrogel. While the orifice is blocked, there is still motion in the upper parts of the silo that may cause an imbalance of forces in the blocking arches, with a considerable delay of up to several seconds. Figure 3.7b demonstrates this delay. The granular material still reorganizes in the upper regions of the container after the outflow has already stopped. During a period of 1.75 seconds, no grain leaves the orifice but the material in the upper parts rearranges slowly. The blocking structure dissolves after 1.75 seconds. We have plotted the configuration immediately after the clog started on the right hand hand side of the figure, behind the solid line. Comparison with the state at the end of the clog evidences the shift of the grains during the congestion.

The viscoelastic character of the hydrogel is the reason for the slow dynamics of these processes. It

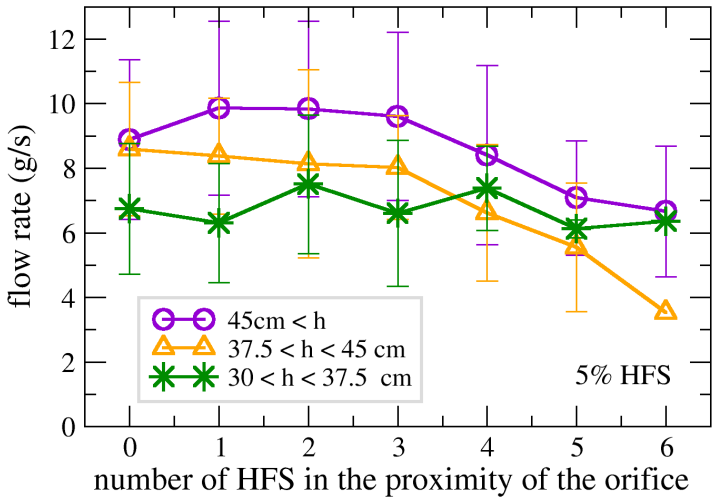

Figure 3.6: Flow rate as a function of the number of HF grains in the proximity (5 particle diameters) of the orifice. Data taken for 30 cm$< h <$ 80 cm. Data points represent 18 measurements on average, error bars stand for the standard deviation.

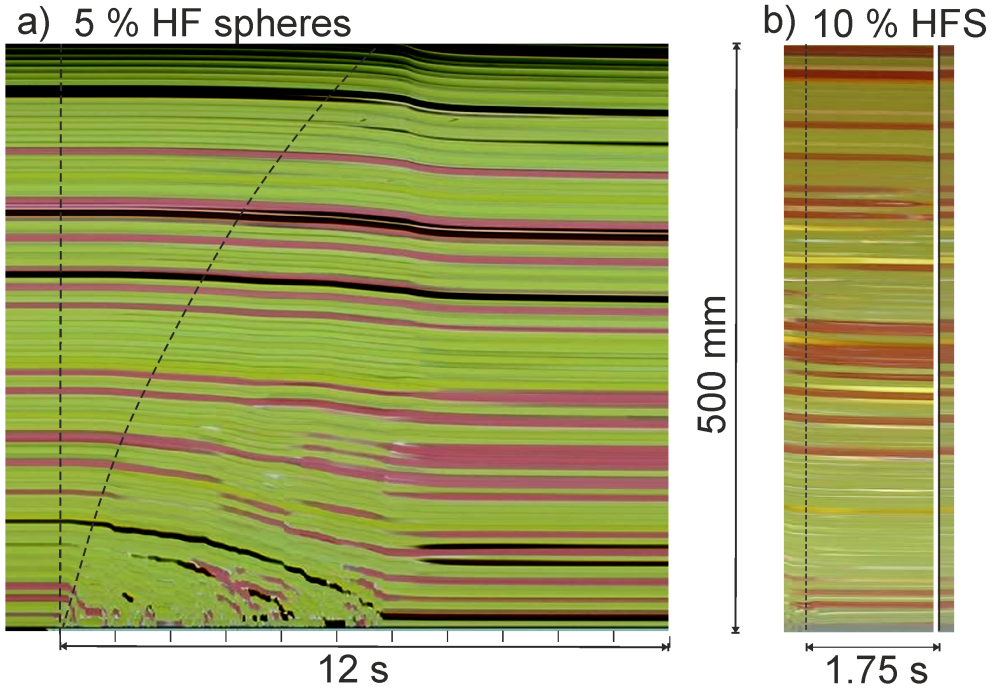

Figure 3.7: Space-time plots of a vertical cross section of the silo in the central axis above the orifice ($D = 12$ mm). a) Mixture with 5 % HF spheres. The grains start to flow only locally at the orifice after it is opened (vertical dashed line). The reaction of the material in the upper part is delayed considerably (bent dashed line). b) After the orifice at the bottom clogs (dashed line), the material (with 10 % HF spheres) in the upper part still reorganizes for several seconds. The state immediately after the outflow stopped is re-plotted behind the white gap, to visualize the changes during the clogged state.

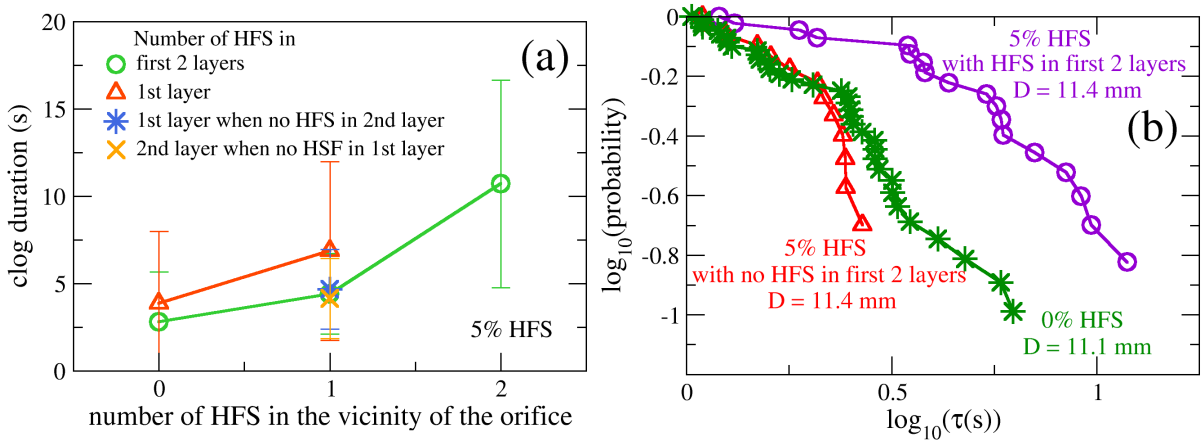

Figure 3.8: (a) Clog duration as a function of the number of high friction spheres (HFS) in the vicinity of the orifice. The data sets correspond to cases when only the first layer, or the first 2 layers are considered. Data points represent 13 clogs on average, error bars stand for the standard deviation. (b) Probability of non-permanent clogs longer than τ as a function of τ on a log-log scale.

is even more evident immediately after the outlet of the freshly filled container is opened for the first time, as shown in Fig. 3.7a. The flow at the orifice sets in immediately, while the motion of the grains far above the orifice is delayed by up to several seconds. Note that in silos filled with hard grains, there is practically no such delay. This phenomenon has been reported for pure hydrogel samples before [85]. The delay times can vary slightly between individual runs of the experiment. Compared to the pure hydrogel samples, the addition of few percents of hard grains even seems to slightly enlarge the average delay times.

We analyze now, how the duration of non-permanent clogs depends on the number of hard frictional spheres (HFS) in the vicinity of the orifice. As we see in Fig. 3.8(a), the clog duration increases with an increasing number of HFS. Hard frictional beads in the first and second layer both have an effect on the clog duration, with a slightly larger influence of the first layer. Another way to quantify how hard frictional beads in the vicinity of the orifice influence the duration of non-permanent clogs is to plot the probability that the clog is longer than a specific time interval τ. This is shown in Fig. 3.8(b) as a function of τ in a log-log plot. The curve characterizing a pure hydrogel sample is very close to the curve of a mixture with 5% HFS, when no HFS are present in the first 2 shells above the orifice. However the curve is considerably shifted for those clogs, when HFS are present in this region. Thus, the stability of blocking arches clearly increases when hard frictional grains are present in them. This can be understood intuitively.

3.4.4 Arch structure analysis

An advantage of the 2D bin with narrow orifice widths is that only few types of clog structures are formed. First, we characterize these clogs by the number of particles involved in the first layer. The most frequently encountered structure in all three orifice sizes is the nearly symmetric four-particle arch, as seen in Fig. 3.1, bottom. Also, the nearly symmetric two particle clogs are encountered more often than the other structures when the orifice width is two sphere diameters or less. Some typical

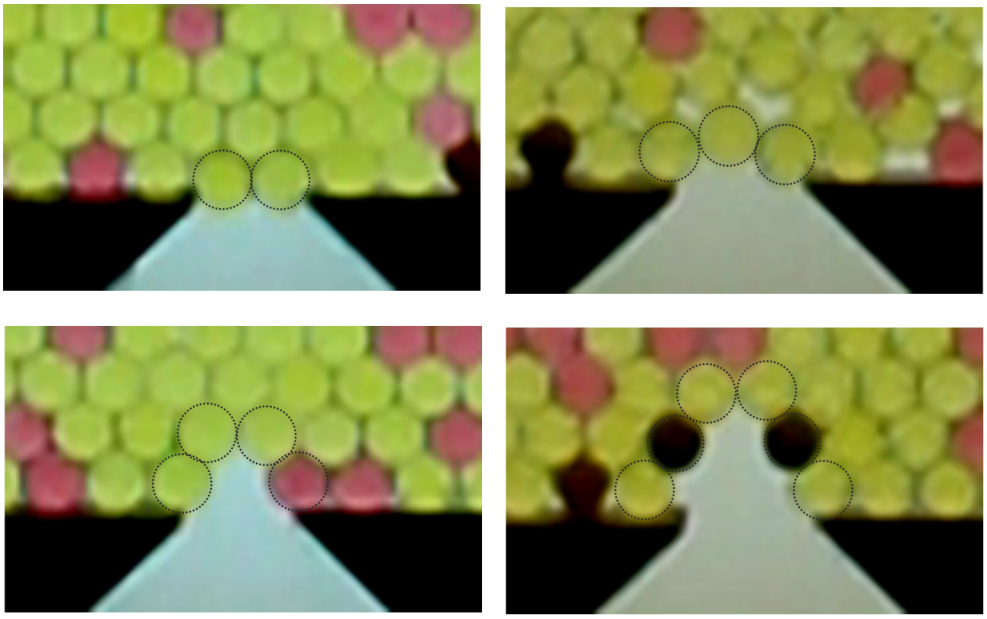

Figure 3.9: Typical structures of blocking arches. The 2 and 4 particle arches were taken from snapshots of clogged states of the 11 mm orifice videos, the 3 and 6 particle arches from 13 mm orifice videos.

structures are shown in Fig. 3.9.

Figure 3.10 shows the statistics of clog structures grouped by the number of particles in the blocking arch for three orifice sizes and two mixture compositions. Here, we analyzed blockages that lasted 1.5 second or longer, and we did not distinguish between temporary congestions and permanent clogs that had to be destroyed by air flushes. Clogs with more than 5 particles do practically never form, three-particle clogs and five-particle clogs were found more often in the larger openings. Four-particle arches represent more than 80 % of all blocking structures. Therefore, we focus primarily on the latter in our further analysis. Within the statistical error, there are no significant differences between the two mixtures.

We will now analyze the composition of these blockages, primarily of the most frequent four sphere arches. Figure 3.11a shows the relative amount X_{hf} of hard grains in the blocking structures, separately for four sphere arches and all others. White numbers the number of arches of the respective type that occurred, summed over all evaluated experiments. We do not distinguish here between the individual positions in the arches. The particle that finalizes the blockage may have arrived from above or from a side. Horizontal dashed lines indicate the percentage x_{hf} of hard grains in the mixture. The result is that hard grains are present in the blocking arches nearly two times more frequently than globally in the sample. This holds, within the statistical uncertainty, for both mixtures with $x_{\mathrm{hf}} = 0.05$ and 0.1, and for all three orifice sizes. In arches with other than four components, the HF grains are even more strongly over-represented, yet the statistical error is much larger for these numbers because of the smaller number of arches found.

One can make the simple assumption that X_{hf} and x_{hf} are related by the approximation

$$X_{\mathrm{hf}} = \frac{x_{\mathrm{hf}} p_{\mathrm{hf}}}{x_{\mathrm{hf}} p_{\mathrm{hf}} + (1 - x_{\mathrm{hf}}) p_{\mathrm{hyd}}}. \tag{3.1}$$

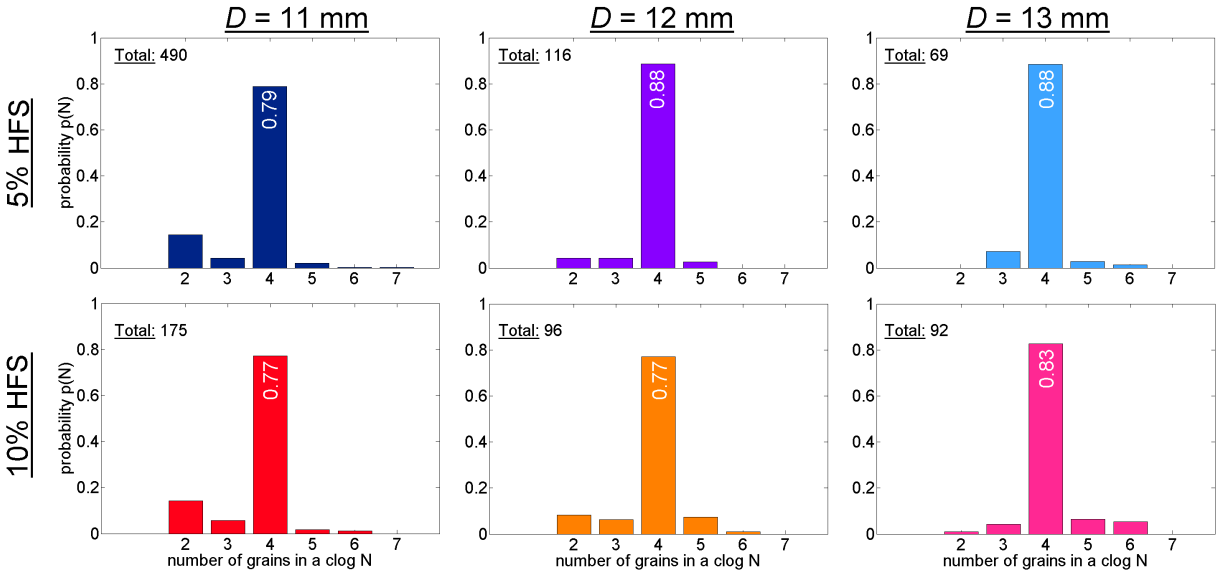

Figure 3.10: Number of particles forming the blocking arches at the orifice for two mixture compositions and three orifice sizes. It is seen that neither the composition of the mixtures nor the variation of the orifice width influences the dominance of 4 particle clogs. Clogs consisting of 2 particles are much less probable in the larger orifices, which is intuitively clear.

This equation allows us to get a rough estimate of the ratio of the blocking probabilities p_{hf}/p_{hyd} of hard and elastic components of the mixture:

$$\frac{p_{hf}}{p_{hyd}} = \frac{X_{hf}(1-x_{hf})}{x_{hf}(1-X_{hf})} \tag{3.2}$$

Taking the values of x_{hf} of the mixtures and a factor of $X_{hf} \approx 2x_{hf}$, one obtains $p_{hf}/p_{hyd} \approx 2.2$. Hard grains are nearly twice as probable to get stuck in a blocking structure at the orifice, independent of D for all orifice widths studied here. It is also interesting to check how often hard spheres appear in the next layer of grains above the blocking arch. This is analyzed in Fig. 3.11(b). As expected, the occurrence of hard spheres is not significantly enhanced there, the slight deviation from x_{hf} is within the statistical error.

With the relative frequency of X_{hf} of around 0.21 in four-particle arches in the 10 % HF spheres mixtures, assuming that the occupations of site of the blocking arch are independent of each other, one would expect that approximately 41 % of all arches contain one hard grain, and 18 % two hard grains. Actually, the experimentally determined share is somewhat smaller but within the statistical error. On the other hand, in the 5 % mixtures one has $X_{hf} \approx 0.1$, which leads to expected 29 % of blocking arches containing a hard particle. This is in good agreement with the experiments. When one analyzes the 4-sphere arches in more detail, one finds a statistically significant larger share of HF spheres at the two lateral positions (more than 60 %) than at the two upper, central positions. The reason may be that the blocking by hard grains is nearly twice as effective when they are in contact with the ground plate, where they can efficiently hinder lateral motion of grains.

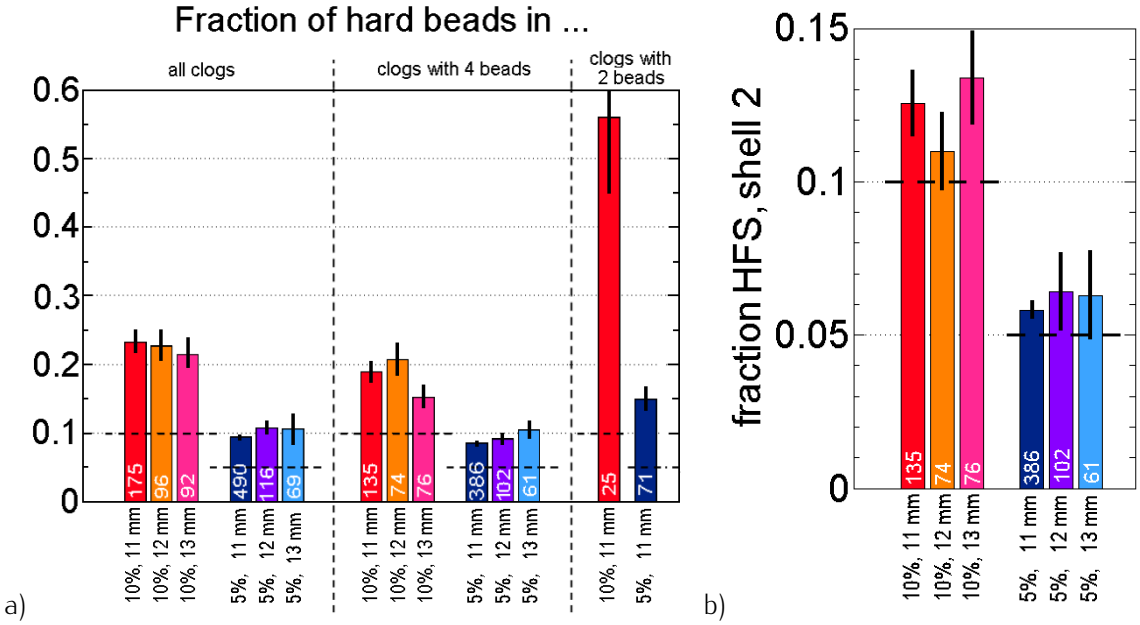

Figure 3.11: Statistics of the occurrence of HF spheres in the blocking arches in the experiments. The white numbers indicate the number of events compiled in the column. a) Composition of the arch, viz. the first coordination shell above the orifice; fractions X_h of hard beads compared to the bulk concentrations x_h (dashed lines). The left section includes all clogs of at least 1.5 s duration. In the middle, the statistics for 4-sphere arches is shown. On the right, data of 2-sphere arches are collected. b) Concentration of HF spheres in the second coordination shell, averaged over all clogs.

3.5 Numerical analysis

3.5.1 Numerical Model

The numerical simulations were carried out with the open source Discrete Element Method (DEM) granular simulation software LIGGGHTS [17]. For the calculation of the inter-particle force $\vec{F}_{ij}$, a Hertz-Mindlin contact model was chosen [108], including a normal $\vec{F}_{ij}^{\,n}$ and tangential $\vec{F}_{ij}^{\,t}$ component, both modeled as a short-range spring dashpot interaction. The elastic and damping particle-particle interaction coefficients are well reproduced by the model, given several input parameters, such as, the Young's modulus Y, the restitution coefficient e_n and the friction coefficient μ. Furthermore, the Coulomb friction constraint is applied. The tangential force is cut off so that $|\vec{F}_{ij}^{\,t}| < \mu|\vec{F}_{ij}^{\,n}|$ is satisfied. The used integrator resolving the particle positions and velocities, was chosen such that in a purely elastic collision, energy would be conserved. In other words it is stable. Besides, as a simplification, we assumed the contacts between particles to be independent of each other. However, it has been shown in the past [94] that when soft particles are densely packed, a force model taking into account multiple contacts better captures the experimental response. We partly compensated this effect, using the upper bound value of Young's modulus (experimental estimation), for the soft low frictional particles.

The numerical geometry mimics the experimental setup, i. e. the width of the flat container is 40 cm, the thickness of the cell is 6.12 mm, only slightly larger than the particle diameter $d = 6$ mm. The two species of particles have the same size. Thus, the system is monodisperse. However, the

mechanical properties of the constituents differ notably in their stiffness and friction. For the contact between soft low-friction spheres we set a Young modulus of $Y_{\text{hyd}} = 100$ kPa and a friction coefficient of $\mu_{\text{hyd–hyd}} = 0.02$. Note that these values are consistent with earlier studies [94]. Besides, ball bouncing experiments led to a rough estimation of the hydrogels' restitution coefficient, resulting $e_{n_{\text{hyd–hyd}}} = 0.5$, approximately.

The contact between two airsoft bullets (hard, frictional) was mimicked using a Young modulus $Y_{\text{hf}} = 500$ $Y_{\text{hyd}} = 50$ MPa, $\mu_{\text{hf–hf}} = 30 \cdot \mu_{\text{hyd–hyd}} = 0.6$ and $e_n = 0.8$. In order to discriminate the effect of friction, we pursued simulations with three distinct inter-species frictions $\mu_{\text{hf–hyd}} = 0.05,\ 0.2$, and 0.3. The friction with the walls was set equal to the particle–particle friction i.e. $\mu_{\text{hf–wall}} = \mu_{\text{hf–hf}}$ and $\mu_{\text{hyd–wall}} = \mu_{\text{hyd–hyd}}$, but the friction of hydrogel-like particles with the bottom plate was assumed to be similar to that with the frictional species, $\mu_{\text{hyd–bottom}} = \mu_{\text{hyd–hf}}$. Using these parameters, we detected a maximum particle overlap of around 10% in terms of the particle diameter. Those particles were usually found in the bottom of the system when the silo is full.

The used set of orifice widths was $D = 11, 12, 13$, and 14 mm corresponding to aspect ratios of $\rho = 1.83, 2.0, 2.17$, and 2.33. Similar to the experiments, we are able to observe the clogging, intermittent and continuous flow regimes using this range of orifice widths. A simple procedure was implemented in order to resolve the occurring clogs. The number of particles exiting the container was checked every second, in case it was found to be zero, particles located only 5 mm away from the center of the orifice were removed from the simulation. Additionally, particles located in the vicinity of the hole were moved upwards within 0.1 s, imitating an air flush. Simulations for each set of parameters were run four times with different random initial packings, which are taken into account in Section 3.5 in order to improve the accuracy of results.

Despite the simplicity of the interaction model, used to describe the particle-particle and particle-wall collision, the numerical results confirm that the presence of a small fraction of hard frictional particles notably impacts the outflow dynamics. The contact between different species, characterized by a friction coefficient $\mu_{\text{hyd–hf}}$, turns out to be an important parameter of the model.

3.5.2 Flow rates

In a first step, we examine the outflow as a function of the mixture composition, fixing the size of the orifice and using $\mu_{\text{hyd–hf}} = 10\,\mu_{\text{hyd–hyd}}$. Figure 3.12(a) displays results obtained for a system containing only soft, low-friction particles, and systems with 5%, and 10% of hard frictional particles, the remaining spheres being soft, with low-friction. As noticed, the addition of even a small number of hard frictional grains leads to a significant reduction of the mass discharged for the same period of time. The homogeneous system of soft, low-friction particles discharges much faster while adding hard frictional particles induces the formations of clogs, where the particle flow is interrupted randomly. Moreover, similar to the experimental scenario, both the frequency and the duration of the clogs increase with the increasing fraction of hard, frictional particles. For clarity, Fig. 3.12(b) also shows the analysis of the mass vs. time curves, after removing the periods of time in which the flow rate is zero (between avalanches). These data allow us to numerically obtain the evolution of the mass flow rate dm/dt in time, as well as to analyze its dependence on the filling height and orifice size.

For further analysis, it is necessary to accurately resolve the time evolution of the granular bed height.

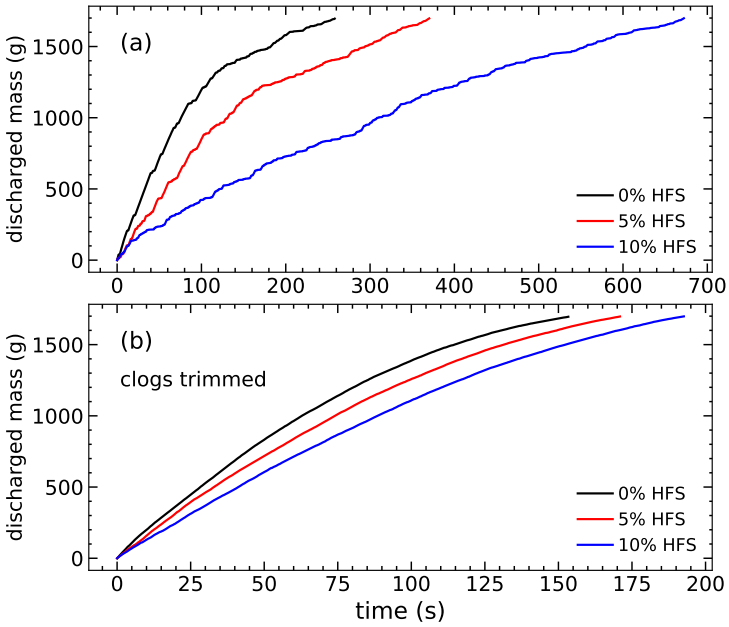

Figure 3.12: Discharge characteristics calculated numerically for $D = 11$ mm, $\mu_{\text{hyd–hf}} = 0.2$. The top graph shows the original data, the bottom graph presents the same data adjusted by trimming the phases of stopped outflow.

The mean bed height $h(t)$ is obtained by sampling ten equally sized vertical slices, and locating the highest particle h_k in each of them. Then, the value of $h(t)$ is found as the average of that set. For this purpose, we use the trimmed data as shown in Fig. 3.12b, thus $h(t)$ is a function of the trimmed time. Figure 3.13a exemplifies results of this procedure for a system with 5% of hard frictional particles $\mu_{\text{hyd–hf}} = 2.5\ \mu_{\text{hyd–hyd}}$, and orifice diameter $D = 12$ mm. The main figure shows the height versus time behavior, while the inset illustrates the evolution of the height versus mass remaining in the container during discharge. The latter slightly deviates from a straight line due to the compression of particles, contrary to usual hard granular media where the height is approximately linearly proportional to the mass in the silo. In addition, the dependence of the mass flow rate $\frac{dm}{dt}$ on the column height can also be deduced numerically, see for example Fig. 3.13(b).

Figure 3.14 summarizes our systematic study of the mass flow rate $\frac{dm}{dt}$ versus height h, performed numerically. Specifically, we executed simulations varying the system composition and the friction coefficient between both particle types, $\mu_{\text{hyd–hf}}$, keeping the orifice diameter of $D = 12$ mm constant. In general, the numerical outcomes reflect similar trends as the experimental ones, (see Sec. 3.4.2). First, the numerical model reproduces that the mass flow rates for mixtures and for the homogeneous system of soft, low-friction particles strongly decrease with decreasing filling height in the experiment. In addition, we also detect numerically that this trend is affected significantly when the mixture composition changes: already a small amount of hard frictional particles notably influences the discharge process. Furthermore, as the concentration of hard frictional particles is increased, the changes in flow rate become weaker, and the system tends to recover the "classical granular response" of a height-independent mass flow rate.

Additionally, we numerically explore the impact of the inter-species friction coefficient $\mu_{\text{hyd–hf}}$ on

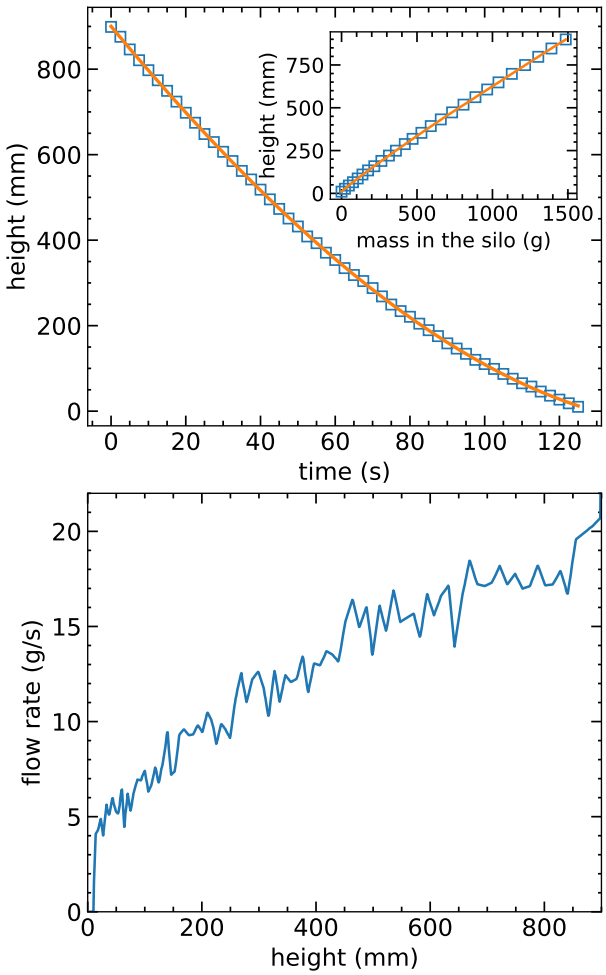

Figure 3.13: Discharge characteristics calculated numerically for $\mu_{\text{hyd–hf}} = 0.05$, $D = 12$ mm, 5% hard spheres. The top image shows the granular bed height $h(t)$ using the trimmed data, the bottom image gives the discharge rate as a function of the height. Small statistical fluctuations result from the computation procedure, while the trend of decreasing flow rate with lower bed height is systematic.

the results, keeping $\mu_{\text{hyd–hyd}}$ and $\mu_{\text{hf–hf}}$ constant. Figures 3.14(a), 3.14(b) and 3.14(c) illustrate outcomes corresponding to $\mu_{\text{hyd–hf}} = 2.5\mu_{\text{hyd–hyd}}$, $\mu_{\text{hyd–hf}} = 10\mu_{\text{hyd–hyd}}$, and $\mu_{\text{hyd–hf}} = 15\mu_{\text{hyd–hyd}}$, respectively. First, it is obvious that the value of $\mu_{\text{hyd–hf}}$ significantly impacts the magnitude of the mass flow rate $\frac{dm}{dt}$. Besides, the impact of the hard frictional particles is enhanced, as $\mu_{\text{hyd-hf}}$ increases. Thus, the system's response approaches a height independent mass flow rate.

Figure 3.15 shows the mass flow rate obtained for different orifice diameters. For clarity, the calculations have been performed with constant $\mu_{\text{hyd–hyd}} = 0.02$ and $\mu_{\text{hf–hf}} = 30\ \mu_{\text{hyd–hyd}}$ and exploring the impact of $\mu_{\text{hyd–hf}}$ on the results. The presented data correspond to averaged values over different time intervals, in terms of the displacement of the granular bed's surface. As expected, we detect that the mass flow rate increases with increasing orifice diameter. Similar to the experimental results, the data can be approximated in this narrow range by a linear increase. The specific values of the flow rate decrease significantly with the introduction of hard frictional particles. In addition, we also

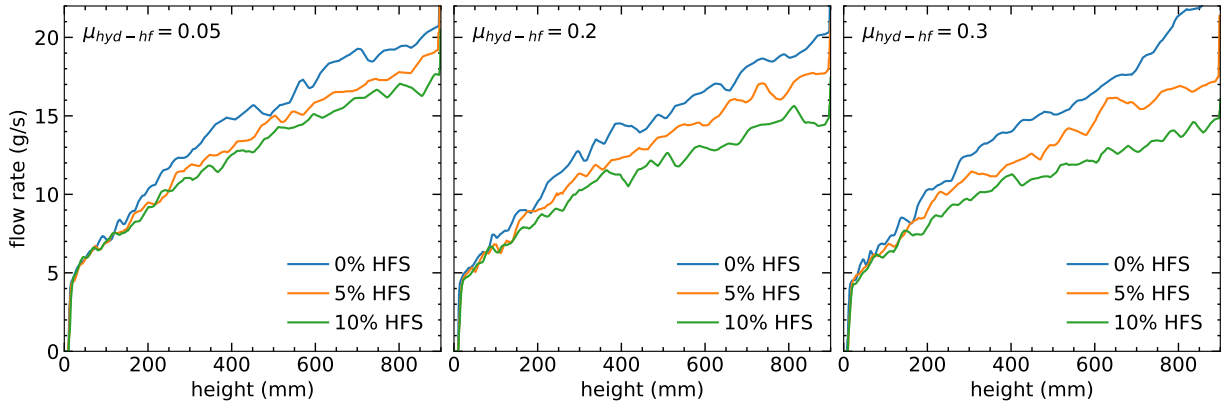

Figure 3.14: Numerically calculated flow rate as a function of bed height for different mixture ratios and an orifice size of $D = 12$ mm. The interspecies friction i.e. the friction between the HF and the soft, low-friction particles, reflected in $\mu_{\text{hyd–hf}}$, is different in the subfigures.

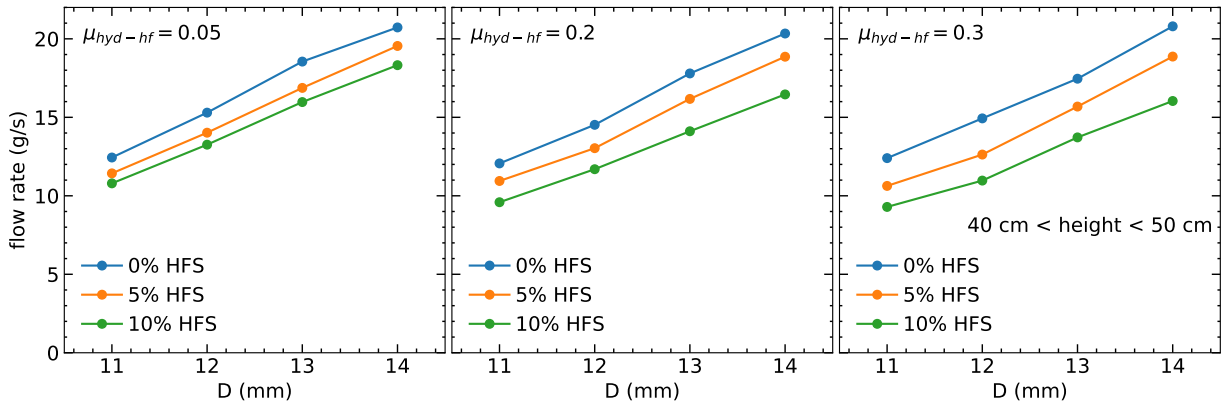

Figure 3.15: Average flow rate in a small range of bed height (40 cm $< h <$ 50 cm) as a function of orifice size. In these numerical simulations, the inter-species friction is increased from the left figure to the right $\mu_{\text{hyd–hf}} = 0.05;\ 0.2;\ 0.3$.

observe that the friction coefficient between particles of different types significantly affects the outflow dynamics. Specifically, the flow rate is notably reduced when increasing $\mu_{\text{hyd–hf}}$. This suggests that stable arches composed of different particle types play a significant role in the outflow dynamics. It is plausible that the increase of $\mu_{\text{hyd–hf}}$ enhances the stability of mixed arches, which is even noticed when $\mu_{\text{hyd–hf}} = 2.5\mu_{\text{hyd–hyd}}$.

3.5.3 Pressure characteristics

Section 3.4.2 and Ref. [85] include experimental results which indicate that changes of the mass flow rate with the height correlate with changes of the pressure at the bottom of the system. Figure 3.16 illustrates the numerical outcome of the pressure at the bottom of the silo, obtained for several mixture compositions and particle frictions $\mu_{\text{hyd–hf}}$. Note that for a homogeneous system composed of low-friction particles, the curve is very close to hydrostatic behavior (linear increase). The observed deviation is

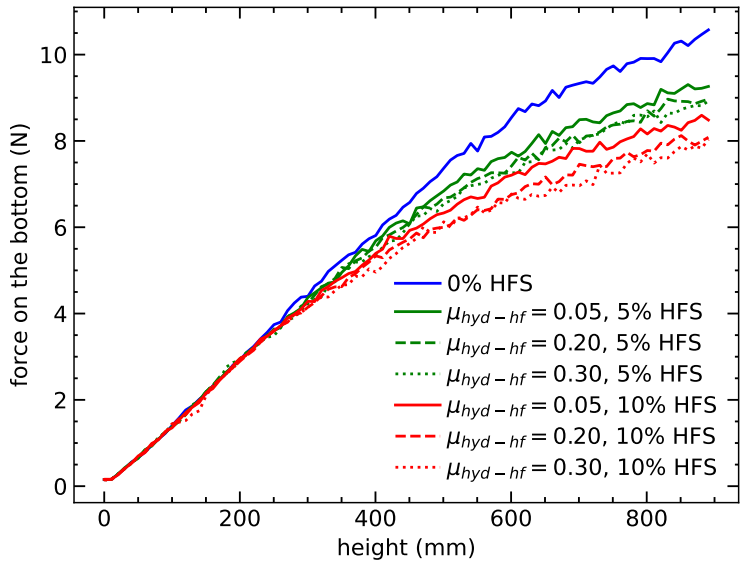

Figure 3.16: Force acting on the bottom plate as a function of the bed height (numerical data, orifice size $D = 12$ mm; cf. experimental data in Fig. 3.3).

consistent with the low but still nonzero friction coefficient ($\mu_{\text{hyd–hyd}} = 0.02$) of the particles. Similar to the experimental findings, the pressure at a given time (or granular bed height) changes significantly in the simulations if hard frictional particles are added, and the system response deviates from hydrostatic behavior. This shows that the presence of hard and frictional particles induces scattering of the stress transmission with respect to the direction of gravity. As a result, the stress transmission to the container walls is enhanced. Once again, we find that the value of $\mu_{\text{hyd–hf}}$ is highly relevant, as the previously described trend enhances with increasing $\mu_{\text{hyd–hf}}$.

3.5.4 Flow intermittency and structure of the arches

The statistics of the passing times δt, defined as the time lapse between the passing of two consecutive particles through the orifice also reveals interesting features of the clogging process. In Fig. 3.17, we illustrate the probability distributions $p(\delta t)$ obtained in systems with different compositions for comparison. The first issue is the notable presence of very fast events, which are less likely when a small amount of hard frictional particles is added. Similar to the experimental trend of the clogging statistics, the tail of the distribution also gets slightly fatter if one increases the percentage of hard grains in the mixture. The distribution also shows a well defined peak at $t_d \approx 0.006$ s, regardless of the inter-species friction $\mu_{\text{hyd–hf}}$ (see Fig. 3.17 inset). In those specific cases, we find that the most probable vertical velocity of particles crossing the orifice is $v_d \approx 0.55$ m/s, significantly larger than the corresponding *free fall* value $\sqrt{2gR}$. This numerical result indicates that the up-down pressure gradient at the orifice region notably affects the particle outflow. Moreover, it also suggests that on average two consecutive particles leave the silo within a vertical distance of approximately $D/2$.

After identifying the characteristic time of the passing times' statistics, we here define an infinite

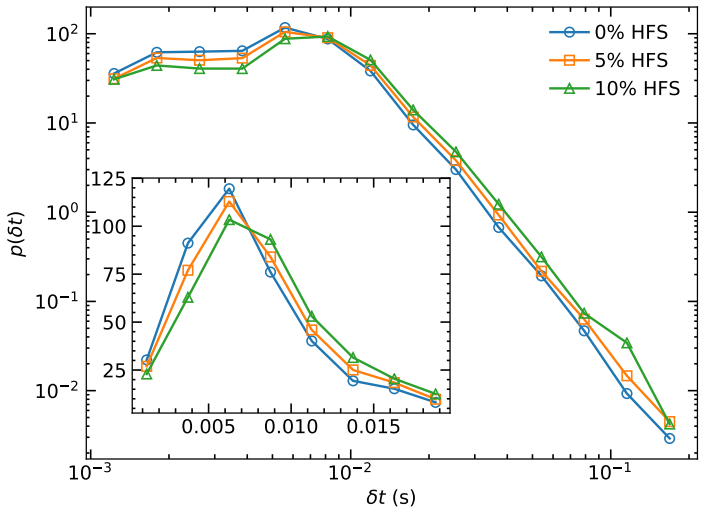

Figure 3.17: Probability density of the elapsed time between two particles passing in log-log representation. In these numerical simulations, the inter-species friction was $\mu_{\text{hyd-hf}} = 0.2$, while the orifice size was $D = 12$ mm. The inset shows the same data but in a smaller region with linear axes.

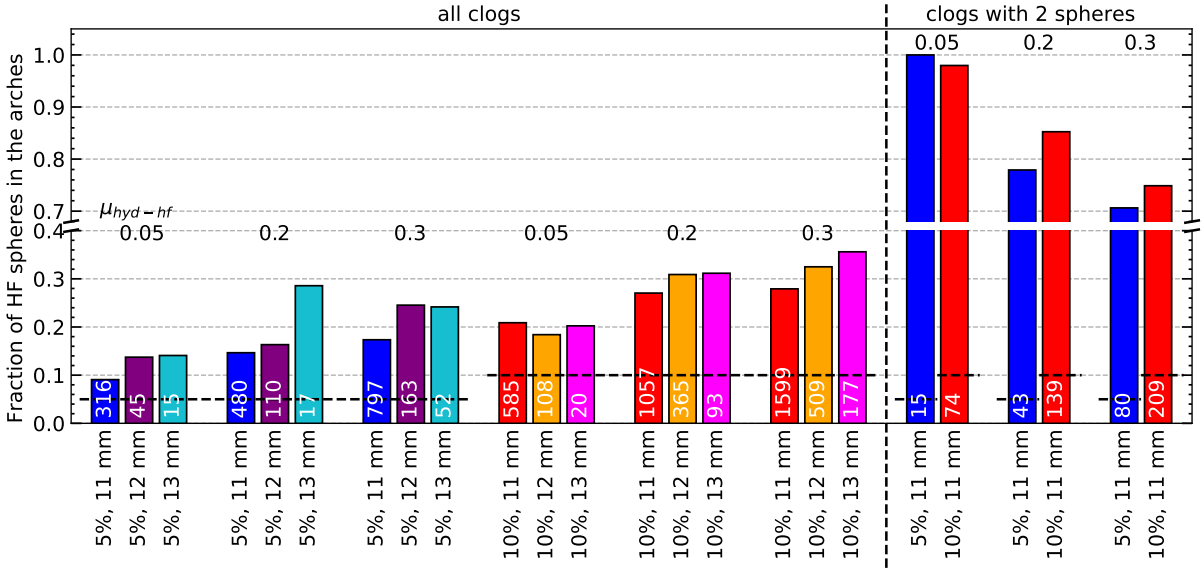

Figure 3.18: Statistics of the fraction of HF spheres in the blocking arches in clogged states in numerical simulations. The bars represent the mean fraction of HF spheres in the arches compared to the bulk concentration (dashed horizontal lines). At the right of the vertical dashed line, the clogs composed of only 2 spheres are considered, while on the left all occurrences are included. Under each bar, the percentage of HF spheres in the silo and the orifice size are indicated. The inter-species friction $\mu_{\text{hyd-hf}}$ is shown. The white numbers indicate the number of events compiled in the column (cf. Fig. 3.11 for experimental data)

passing time when $\delta t = 1$ s, for practical reasons. After that, the system is considered permanently clogged, and a stable arch blocks the orifice. Fig. 3.18 illustrates the statistics of the occurrence of hard frictional spheres in the blocking arches. One of our main findings is that in all cases, the fraction of hard frictional particles forming arches was higher than their bulk fraction, indicated by the horizontal dashed line. We achieved the closest match to the experimental results for all clogs when an inter-species friction $\mu_{\text{hyd-hf}} = 0.05$ was chosen. Seemingly, the larger the orifice size is, the more frequently hard frictional particles occur in arches, while the number of blocking events decreases. Consistently, the increasing inter-species friction also enhances the occurrence of hard frictional spheres in arches considering all clogged states, which again shows its relevance. To gain better insight, we separately examined clogged states with arches composed of only two particles: In these cases, the arches are overwhelmingly often made up of two hard frictional spheres. Moreover, increasing the inter-species friction decreases the occurrence of hard particles in the arches. This effect can be easily explained by the transition from arches composed of two hard spheres to the configuration with one hard and one soft sphere.

3.6 Discussion and Summary

Our results clearly show that the addition of a small percentage of hard grains to an ensemble of soft, low-friction spheres has dramatic consequences for the flow through a narrow orifice and the clogging statistics in a quasi-2D silo. First, one finds that the outflow rate of pure soft grain ensembles through narrow orifices depends upon the pressure at the silo bottom, which is in contrast to Beverloo's model for hard grains. Second, one observes that the addition of a few percent of hard spheres restores the pressure-independent outflow characteristics predicted by Beverloo (Fig. 3.5(a)). Moreover, the discharge rates of all mixtures approach each other at low container fill heights (Fig. 3.5a). The reason is obviously that the elasticity of the soft grains is less important when the pressure near the orifice is low, then their deformability can be neglected. On the other hand, at high fill levels of the silo, the increased pressure at the bottom can deform the soft grains and squeeze them through the orifice efficiently. Therefore, the outflow rate at a fill height of 40 cm (pressure ≈ 3 kPa) is approximately 2.5 times higher for the pure hydrogel sample than for the 10% mixture. This cannot be explained by the smaller friction coefficient [75] of the hydrogel compared to the hard frictional spheres, since the concentration of the latter is small. The effect of the number of hard frictional grains in the vicinity of the orifice on the flow rate is in accordance with the above described observations. At higher fill levels ($h > 37.5$ cm), the flow rate is found to decrease when the number of HFS is larger than 3 in the proximity (5 d) of the orifice (Fig. 3.6). At low fill levels, when the pressure near the orifice is low, increasing the number of HFS around the orifice does not affect the flow rate significantly.

We note that a comparison of outflow rates with those of a pure hard sphere ensemble is not possible because the latter will permanently clog at orifice widths smaller than $2d$, with mean avalanche sizes well below 10 particles.

Even though the probability of two hard grains reaching the orifice simultaneously and blocking the outlet is very low, we find a substantial influence of hard frictional particle doping on the clogging statistics, both in experiment and simulations. The probability that a hard frictional particle is involved in the formation of the blocking arch is, on average, twice as large as for soft hydrogel spheres in

the mixtures. However, the time evolution shown in Fig. 3.4 shows that the effective discharge is considerably delayed by frequent intermittent stagnations of the flow in the doped mixtures.

The material forms non-permanent clogs which are resolved after some delay, because of slow reorganizations of the packing structure in the granular bed within the complete container above the orifice. This reorganization occurs on a timescale of a few seconds, as illustrated by Fig. 3.7(a). Interestingly, the probability distribution of clog durations is very similar for a pure hydrogel sample and a 5% mixture if no HFS are present in the first two layers above the orifice (Fig. 3.8(b)). The clog duration clearly increases when HFS are present near the orifice. This observation underlines the important role of hard frictional beads in the vicinity of the orifice.

Numerical simulations also shed light on the impact of the inter-species friction on the dynamic behavior of the granulate. For instance, the deviations in the flow rate between the different ensembles were enhanced when increasing $\mu_{\text{hyd–hf}}$ (see Fig. 3.14 and Fig. 3.15). Moreover, the total vertical force acting on the bottom wall is also slightly affected by this parameter (see Fig. 3.16). In general, increasing the friction between the two types of particles leads to more frequent clog events, and in those, the occurrence of HFS in the blocking arches is favored, significantly (see Fig. 3.18). One explanation of the much higher importance of $\mu_{\text{hf–hyd}}$ as compared to $\mu_{\text{hf–hf}}$ is the fact that owing to the low concentration of hard frictional grains, the probability of direct contacts of two hard grains is substantially smaller than that of a HF sphere and a hydrogel neighbor.

It is worth mentioning, that the contact model used in our study does not quantitatively reproduce the characteristic time of the unstable clogs obtained experimentally with low-frictional hydrogels. In fact, the Hertz-Mindlin contact model is more suitable for reproducing the behavior of hard grains, where clogs are typically very stable. However, both experiment and simulations are in good qualitative agreement, and allow a comprehensive analysis of the system from complementary points of view. This study demonstrates that the behavior of mixtures of grains with different frictional and elastic properties cannot be described by a simple interpolation of dynamic parameters, but that already the presence of a low percentage of one of the species can alter the dynamics substantially. In many practical situations, for instance in agriculture, but also in natural phenomena like mud or debris flow, the coexistence of grains of very different sizes and mechanical properties is the rule, not the exception. It adds a new level of complexity that has been studied only scarcely in the past. Here, we have peeked into this complex field by restricting our study to monodisperse materials, in a quasi-2D geometry. We also restricted the discussion to small doping percentages. This is a considerable simplification of relevant practical cases, but it shines a light on the various phenomena expected in such systems. Finally, further investigations should be carried out, addressing the significance of adding rigid grains in the evolution of the force chains and contact network.

Conflicts of interest

The authors declare no conflict of interest.

Acknowledgments

This project has received funding from the European Union's Horizon 2020 research and innovation programme under the Marie Skłodowska-Curie grant agreement CALIPER No 812638. The Spanish MINECO (FIS2017-84631-P MINECO/AEI/FEDER, UE Projects) and the Hungarian NKFIH (grant No. OTKA K 116036) supported this work. The authors acknowledge discussions with J. Dijksman and J. van der Gucht. The content of this paper reflects only the authors' view and the Union is not liable for any use that may be made of the information contained therein.

Appendix A

The statistics of avalanche size distributions for hard grain samples can be described following the model of Thomas and Durian [109]. They assume that the probability p that a clog is formed when the n-th particle is discharged is constant. Then, the probability that a clog stops an avalanche of size s is

$$p_s = (1-p)^{s-1}\, p = p \exp\left(-\frac{s-1}{s_0}\right). \tag{3.3}$$

(the first particle passes with probability one, otherwise there is no avalanche) with $s_0 = -1/\ln(1-p)$. The mean avalanche size $\langle s \rangle$ amounts to

$$\langle s \rangle = \sum_{s=1}^{\infty} s\, p_s = \frac{1}{p}. \tag{3.4}$$

This quantity is a characteristic parameter often used in the description of silo discharge statistics. For all practical situations (i. e. $\langle s \rangle \gg 1$), both quantities $\langle s \rangle$ and s_0 can be considered equal. Experimentally, it is easier to evaluate the cumulative probability $\Pi(S)$ of avalanches having a size larger than S

$$\Pi(S) = (1-p)^S. \tag{3.5}$$

(S particles have passed the orifice with probability $(1-p)$ each). The avalanche statistics is found straightforwardly from a fit of the exponent in $\Pi(S) = \exp\left(-\frac{S}{s_0}\right)$. In a mixture of hard and elastic grains, one can assign different blocking probabilities p_{hf} and $p_{\mathrm{e}} \equiv p_{\mathrm{hyd}}$ to the respective components.

For soft grains, the blocking probability is a function of the container fill height [83]. When the pressure at the orifice is high, p_{hyd} is small, and it increases with lowering pressure. The consequence is that the avalanche size distribution changes with fill height, the avalanches become shorter on average while the container empties. Yet in any case, p_{hyd} is considerably lower than for hard grains of the same diameter. Experiments with mixtures can provide the relative occurrences of hard and soft grains in the blocking arches, which yield a quantitative measure of relative blocking probabilities.

Chapter 4

Discharge of elongated grains in silos under rotational shear

Tivadar Pongó, Tamás Börzsönyi, and Raúl Cruz Hidalgo

Physical Review E, Accepted 16 August 2022

The discharge of elongated particles from a silo with rotating bottom is investigated numerically. The introduction of a slight transverse shear reduces the flow rate Q by up to 70% compared to stationary bottom, but the flow rate shows a modest increase by further increasing the external shear. Focusing on the dependency of flow rate Q on orifice diameter D, the spheres and rods show two distinct trends. For rods, in the small-aperture limit Q seems to follow an exponential trend, deviating from the classical power-law dependence. These macroscopic observations are in good agreement with our earlier experimental findings [Phys. Rev. E **103**, 062905 (2021)]. With the help of the coarse-graining methodology we obtain the spatial distribution of the macroscopic density, velocity, kinetic pressure, and orientation fields. This allows us detecting a transition from funnel to mass flow pattern, caused by the external shear. Additionally, averaging these fields in the region of the orifice reveals that the strong initial decrease in Q is mostly attributed to changes in the flow velocity, while the weakly increasing trend at higher rotation rates is related to increasing packing fraction. Similar analysis of the grain orientation at the orifice suggests a correlation of the flow rate magnitude with the vertical orientation and the packing fraction at the orifice with the order of the grains. Lastly, the vertical profile of mean acceleration at the center of the silo denotes that the region where the acceleration is not negligible shrinks significantly due to the strong perturbation induced by the moving wall.

4.1 Introduction

Granular materials are everywhere in nature and they are often used in industrial processes. Since long time, humans have employed containers like silos and bins to store them, so it is technologically important to understand their mechanical response under these specific boundary conditions. Thus, notable research efforts have been undertaken in this direction, where the ultimate aim is to derive the macroscopic response of a granular sample from the contact interactions of the whole particle ensemble [71, 110].

Developing technological solutions, several types of silo flow patterns have been detected. For instance, a *funnel flow* pattern is characterized by the initial particle flow in the central region of the silo. Consequently, funnel flow silos often have stagnant grains near the walls, leading to undesired in-service issues. In contrast, *mass flow* pattern provides a uniform outflow without a central flow channel, and the material flows down as a continuum column. Achieving mass flow condition is ideal, in particular, for mixtures of particles that are susceptible to segregation.

The dependence of the particle flow rate Q on the orifice diameter D also has a significant technological interest. Due to its simplicity, the most used expression is the well-known Beverloo's correlation: $Q \propto (D - kd)^{5/2}$ [20]. In the formulation d is the particle diameter and the parameter k enables a good fit of the experimental data for small orifices. In the large-orifice limit ($D \gg kd$), however, a simple power-law $Q \propto D^{5/2}$ is obtained. Recently, Janda et al. presented a different approach to predict the particle flow rate [21]. Examining the kinetic spatial profiles of density and velocity at the orifice of a two-dimensional (2D) silo, they obtained self-similar functions, when using the orifice size D as a characteristic length. This analysis led them to the formulation of the expression $Q \propto (1 - \alpha_1 e^{-D/\alpha_2}) D^{5/2}$ in which the term in the parentheses accounts for the scaling of the packing fraction and thus the density. They found the fitting parameters α_1, α_2 to be around $1/2$, and 6 particle diameters, respectively. In all the described approaches, the value of the exponent $5/2$ can be justified by arguing that once a particle reaches a distance D to the orifice, it starts accelerating. The region of accelerating flow is historically known as the *free fall arch region*.

To control the outflow in silos, several approaches have been used. Typically, the silos and hoppers have been perturbed, for instance, using electric fields to control the outflow of metallic beads [32], magnetic fields to introduce vibrations in the orifice region [33], or inducing a repulsive force between the grains [34, 35]. The impact of external vibration on the macroscopic flow rate of a silo is far from being understood. More than thirty years ago, Hunt et al. experimentally observed a flow rate enhancement when increasing the intensity of a horizontal vibration [26]. Vertical vibrations, however, produce a more complex response, showing a flow rate decrease when rising the dimensionless acceleration amplitude Γ. On the contrary, when using a higher oscillation frequency, f, a slight increase of Q against the same parameter was encountered [27]. Pascot et al. have recently obtained experimentally and numerically the existence of two different regimes when varying the oscillation amplitude A, and fixing the frequency [111]. In particular, when analyzing small orifices, it is accepted that introducing vibrations alters the arches' stability [28, 29], and the distributions of the unclogging times [30, 31].

Imposing an external shear is also a promising alternative to avoid the formation of stable arches in silos. In the past, the discharge of a cylindrical silo with rotating bottom was explored [36]. However, the authors only focused their attention on the dynamics of the system's surface [36]. Later on, Hilton

and Cleary [37] examined the impact of the external shear on the flow rate Q, finding that it is unaffected when a low shear rate is applied. However, after reaching a critical value, Q increases monotonically with the rotational frequency.

Very recently, the discharge of wooden rods from a cylindrical silo perturbed by a rotating bottom wall was investigated experimentally [41]. It was mainly found that, for small orifices, the flow rate deviates from the classical power-law correlation $Q \sim D^{5/2}$, and an exponential dependence $Q \sim e^{\kappa D}$ is detected. More interestingly, in the continuous flow regime, the introduction of transversal shear induced by the bottom wall's movement decreases the flow rate significantly [41] compared to spheres with similar effective dimensions [38]. Further, increasing the rotation rate results in an increase in the flow rate, which is more significant for smaller orifice sizes, where the flow is intermittent. Since elongated particles in a shear flow develop orientational ordering [112, 113], it is expected that changes in particle orientations due to the external shear will alter the discharge rate. The complex behavior observed in the experiments was not fully explained since the experimental approach has the limitation of not accessing the velocity field, the density distribution and the particle orientations inside the silo.

In this work, we introduce a numerical approach, which replicates the experimental scenario examined in Ref. [41], reproducing their main macroscopic observations. Our aim is to extract relevant features of the process, which were not accessible experimentally. Thus, our approach shed light on understanding, how silo discharge of nonspherical grains is influenced by an external transversal shear.

4.2 Numerical Model

The numerical simulation consists in, using a Discrete Element Method (DEM) implementation [114], modeling the mechanical behavior of elongated particles. The modeled system is a cylindrical flat silo with a diameter of $D_c = 2R_c = 19$ cm, and bottom wall with a circular orifice in the center, with diameter D. As a novelty, an external transversal shear is imposed by the rotation of the silo bottom wall (see Fig. 4.1).

We examine the silo discharge, varying systematically the particle elongation. For simplicity, we employ spherocylinders to model the experimental wooden rods (see Ref. [41]). The model defines pairwise forces between contacting particles. The particle-particle interaction is computed using an algorithm for interacting spheropolyhedra [115, 116]; in particular, an implementation on GPU architecture [114]. A spherocylinder is defined by the location of its two vertices and its sphero-radius $r = d/2$. The spherocylinder's surface is depicted by the set of points at a distance r from the segment which connects its two vertices. The contact detection between two spherocylinders involves finding the closest point between the two edges [117]. The overlap distance δ_n between two spherocylinders equals the overlap distance of two spheres of radius r, located at each edge. Then, the contact force is determined as the sum of the normal and tangential components $F_{ij} = F_n\hat{n} + F_t\hat{t}$. The normal unit vector $\hat{n}$ points from the center of one sphere to another, while the tangential $\hat{t}$ is parallel with the tangential velocity. The normal force is calculated by a simple linear spring-dashpot model $F_n = -k_n\delta_n - \gamma_n v_n^{\text{rel}}$ where k_n is a spring coefficient, γ_n a damping coefficient, δ_n is the overlap between two particles, and v_n^{rel} is the relative velocity in the normal direction. The tangential force represents the friction between two particles, it is also modelled with a spring-dashpot but taking into account the constraint of Coulomb friction: $F_t = \min\{-k_t\delta_t - \gamma_t v_t^{\text{rel}}, \mu F_n\}$. Here the first term represents a spring with coefficient k_t and

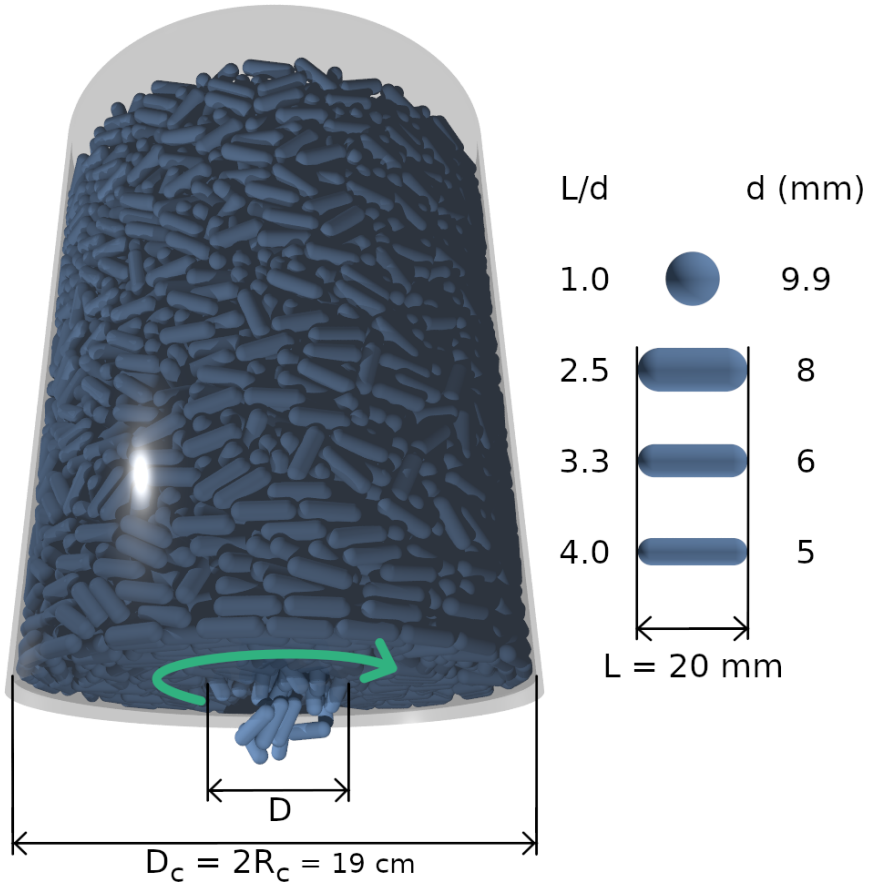

Figure 4.1: Visualization of the rotating bottom silo setup during the discharge of elongated particles of $L/d = 3.3$ (left). The system dimension replicates the experimental setup examined in Ref. [41]. On the right, we display the spherocylinders used within this work, together with their corresponding dimensions.

tangential deformation $\delta_t = |\delta_t|$ which is integrated from the following $d\delta_t/dt = v_t^{\text{rel}}$ where v_t^{rel} is the relative tangential velocity. The vector δ_t is kept parallel to the contact plane by truncation [118]. The second term is proportional to the tangential velocity with a coefficient γ_t, while the particle friction μ sets the constraint for the force.

The DEM algorithm integrates the equations of motion for both translational and rotational degrees of freedom, accounting for gravity g and the force F_{ij} acting between contacting particles. A velocity Verlet method [3] is used to integrate the translational, and a modified leapfrog [119] resolves the rotational ones.

As initial conditions, packing of monodisperse rods were created by letting a dilute granular gas settle inside the closed silo by gravity $g = 9.8$ m/s. The system is composed of $N = 10000$ particles, and only in the case of $L/d = 4.0$ N is set to 22500 to reach a bit higher initial packing (note that in this case the particle's volume is smaller). The discharge process starts by opening the orifice and simultaneously setting the rotation frequency of the bottom wall to one of the following values: $f = 0.0, 0.16, 0.32, 0.64, 0.96,$ and 1.28 Hz. Simulation time for the discharge was in the range of 1–7 hours depending on the flow rate, thus overall discharge time, particle shape and the type of GPU used

(NVIDIA GeForce RTX 2070 and 3080).

The simulation mimics the behavior of wooden particles, thus, the particle density ρ_p is set to 620kg/m^3, a spring stiffness $k_n = 2 \cdot 10^5\ m_p g/d$ is used [120]. Other model parameters were $e_n = 0.9, k_t = 2/7 k_n, \gamma_t = \gamma_n$ and $\mu = 0.5$. The normal damping constant is dependent on the coefficient of restitution e_n in the following way: $\gamma_n = \sqrt{\frac{2k_n m_p}{(\pi/\ln(e_n))^2} + 1}$ [121]. The time step is $\Delta t = 10^{-6}$ s, which is smaller than 2% of the contact time between two colliding particles [7].

The DEM algorithm provides the evolution of the trajectories of all the particles, and their contact network, with the desired time resolution. Post-processing this data employing a coarse-graining methodology enables a well-defined continuous description of the granular flows, via the packing fraction

$$\phi(r,t) = \frac{1}{\rho_p} \sum_i^N m_i \varphi(r - r_i(t)), \tag{4.1}$$

linear momentum $P(r,t)$, and velocity

$$V(r,t) = \sum_i^N v_i \varphi(r - r_i(t)) \tag{4.2}$$

fields [8, 9]. Here m_i, v_i are the mass and velocity of particle i, and $\varphi(r)$ is non-negative integrable function that serves to coarse-grain our particles. In particular, we use a truncated Gaussian function $\varphi(r) = A_\omega^{-1} \exp[r^2/2\omega^2]$, with A_ω^{-1} chosen so that the integral of $\varphi(r)$ over all the space results in 1, the cutoff distance is $r_c = 4\omega$ and $\omega = d^*/2$, where d^* is the sphere equivalent diameter $d^* = (\frac{3V_p}{4\pi})^{\frac{1}{3}}$, with V_p corresponding to the volume of the particle. Additionally, the contact $\sigma^c(r,t)$ and kinetic $\sigma^k(r,t)$ stress tensor fields are calculated in the following way:

$$\sigma^c_{\alpha\beta}(r,t) = -\frac{1}{2} \sum_{i,j}^N f_{ij\alpha} r_{ij\beta} \int_0^1 \varphi(r - r_i + s r_{ij})\, \mathrm{d}s, \tag{4.3}$$

$$\sigma^k_{\alpha\beta}(r,t) = -\sum_i^N m_i v'_{i\alpha} v'_{i\beta} \varphi(r - r_i). \tag{4.4}$$

While the former is computed by a line integral over $r_{ij} = r_i - r_j$ considering the force acting between particles i and j, the kinetic stress represents a granular temperature due to the multiplication of the velocity fluctuation terms $v'_i(r,t) = v_i(t) - V(r,t)$. In the case of elongated particles, the components of the mean orientational tensor O also provide very useful information during the analysis. We have used the following formula for its coarse-graining:

$$O_{\alpha\beta}(r,t) = \sum_i^N l_{i\alpha} l_{i\beta} \varphi(r - r_i), \tag{4.5}$$

where l_i is the unit vector representing the particle's direction. By definition, the diagonal elements of the orientation tensor are non-negative and fall between 0 and 1, representing the degree of alignment in the specific direction. In this way, the quantity expressing the nematic order S of the ensemble of particles is the largest eigenvalue of the O tensor. With our convention S takes values from $1/3$ (completely disordered) up to 1 (fully ordered). In this work, we discuss the orientation of the particles in the cylindrical coordinate system due to the specific symmetry of the silo. Furthermore, for all

the coarse-grained quantities we applied an averaging in the azimuthal direction in the following way: $X(r,z,t) = \frac{1}{2\pi}\int_0^{2\pi} X(r,t)\,\mathrm{d}\theta$. More details about the data post-processing can be found in Ref. [8–10, 118, 122].

In our analysis, we are interested in steady-state conditions, namely, the part of the process in which the flow is stationary. In the case of the static bottom, the discharge slows down near the end of the process due to the lack of particles outside the stagnant zone. While in the case of the quickly rotating bottom, when the height of the material in the silo goes below about R_c, the whole ensemble starts spinning faster. To exclude these initial and final effects, we focus on a time interval, where the flow is stationary in all cases. To have a better statistics, we ran simulations for each set of parameters, starting from three slightly different initial configurations, and apply time and ensemble averaging. Different seeds have been used for the random generator in order to construct different dilute granular gases at the beginning, which yielded distinct initial packings. In the case of small orifices with rotating bottom, we observed intermittent flow. To handle this, during the calculation of the flow rate we excluded the intervals larger than 1 s where there was no flow.

4.3 Results

4.3.1 Effect of rotational shear on the flow rate

Using a numerical approach, we aim to elucidate how the external transversal shear introduced by the bottom wall rotation impacts the discharge process. As mentioned earlier, a recent experimental work examined the flow of particles with aspect ratio $L/d = 3.3$ and $L/d = 2.5$. Here, we extend these findings by systematically varying L/d over a wider range. In line with the experiments, the length of the spherocylinder (measured from end-to-end) is the same $L = 20$ mm, in all the cases. However, the aspect ratio L/d is varied by changing the spherodiameter d. In particular, we investigate the behavior of grains with the following aspect ratios: $L/d = 1.0, 2.5, 3.3,$ and 4.0, whereby $L/d = 1.0$ refers to spherical particles. The diameter of the spherical particle is chosen so that its volume would be equal to the volume of a rod with $L/d = 3.3$: $d = d^*_{L/d=3.3} = 9.9$ mm, which is also the definition for their equivalent diameter.

In Fig. 4.2 we present the flow rate Q as a function of the bottom rotation frequency, obtained for several aspect ratios and orifice sizes. For comparison, the first panel includes the results corresponding to spheres with diameter $d = 9.9$ mm. As expected, we find that for small orifice diameters ($D/d^* \lesssim 5$), a stationary flow does not develop, in any of the cases. However, the imposition of an external transversal shear induces the particle flow. For the case of the spheres, we obtain a slight increase with increasing rotational frequency below $D = 48$ mm or even a weak nonmonotonic behavior ($\approx 5\%$ initial drop then $\approx 5\%$ increase) for the larger orifices which we consider. A more in-depth analysis of the behavior of the spheres in this system can be found in our earlier works [38, 123]. In contrast, elongated particles show a completely different behavior, regardless the particle aspect ratio, either the orifice size, applying external shear significantly reduces the particle flow rate in the range of examined frequencies. It is worth mentioning that at faster rotations the increase of the rotation frequency Q leads to a slight increase of the flow rate. Remarkably, these results nicely agree with the experimental analysis executed using wooden rods [41].

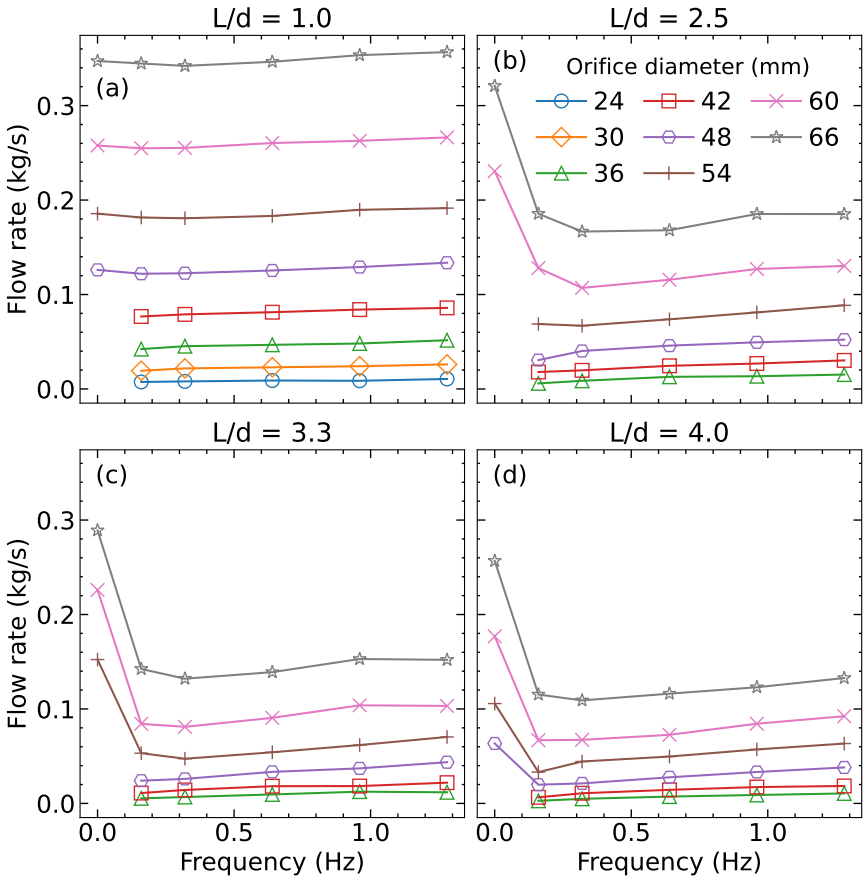

Figure 4.2: Discharge rate as a function of the base rotation frequency. The different panels show data for (a) spheres, and (b)-(d) spherocylinders with aspect ratios of $L/d = 2.5, 3.3, 4.0$ respectively. Each curve corresponds to a specific orifice diameter displayed in the legend.

Next, we extend the analysis, exploring the impact of the particle effective diameter d^*. The data presented in Fig. 4.2 suggest that Q generally reaches a minimum value in the range of rotational frequency of $0.16 - 0.32$ Hz. To quantify the drop, in Fig. 4.3(a), we plot the ratio of the minimum flow rate Q_{min} and the one corresponding to the stationary bottom $Q|_{f=0\ \text{Hz}}$. A general trend becomes apparent: the increasing aspect ratio of the particles causes a larger decrease in the flow rate. After the initial decrease in Q, an increase is observed for fast rotation speeds. In Fig. 4.3(b), we quantify this increase as the ratio of the flow rate at $f = 1.28$ Hz and at the minimum. This clearly shows that the relative increase gets larger as the grains are more elongated or as the orifice size is decreased. Since our particles have different effective diameters, we include two groups of curves in the figure: one with fixed absolute orifice sizes (dashed curves) and one with fixed orifice sizes relative to the effective diameter of the particles (lines). In both cases, our findings are very conclusive; the particle aspect ratio has a significant impact on the system flow rate, which could drop by even 70% for very elongated grains.

In the following, we examine the dependence of the flow rate Q on the orifice size D. In Fig. 4.4, we present data Q vs D, in a log-log plot; additionally, a dashed line representing the classic power-law function with an exponent of $5/2$ is included. One visible tendency is that the more elongated the

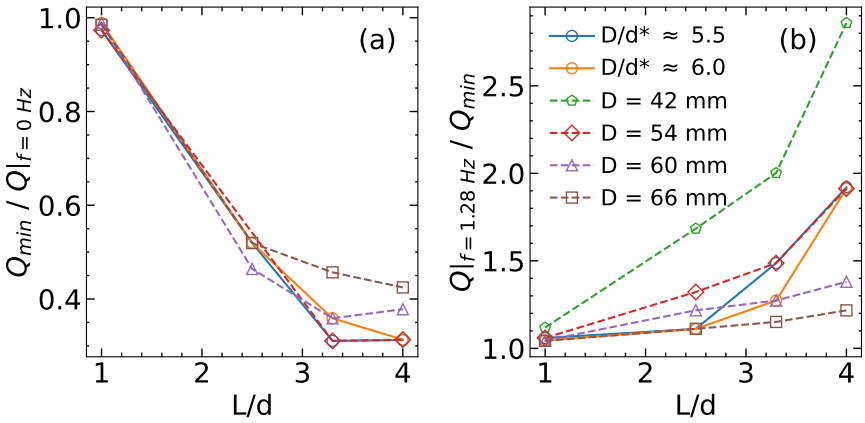

Figure 4.3: (a) Relative initial flow rate drop and (b) relative flow rate increase as a function of the particle aspect ratio. Here Q_{min} denotes the minimum of the flow rate in the frequency variable, $Q|_{f=0\ \text{Hz}}$ and $Q|_{f=1.28\ \text{Hz}}$ are the flow rates measured with the stationary bottom and with the fastest rotation rate, respectively. Lines correspond to data with fixed relative orifice diameter D/d^*, dashed lines display data for fixed absolute diameter sizes.

particles are, the lower the flow rate for a fixed orifice is. For the case of spheres, we observe a concave line in the plots, which is in agreement with earlier findings [38, 123]. This behavior can be explained by either the Beverloo law $Q \propto (D-kd)^{5/2}$ or $Q \propto (1-\alpha_1 e^{-D/\alpha_2})D^{5/2}$ type of dependence. In the cases of rods, in the limit of small orifices, we obtain power-law relation but with a larger exponent, although in the limit of large orifices, the power-law correlation $Q \sim D^{\frac{5}{2}}$ is also reproduced. Complementarily, in Fig. 4.5 we present the flow rate data in semilog plots. It highlights that the flow rate is also compatible with an exponential trend $Q \sim e^{\kappa D}$, when decreasing the orifice diameter. In general, the value of $\kappa_{\text{sim}} = 0.084$ mm^{-1}, fits with a good accuracy our observations. Remarkably, a similar trend was obtained experimentally in Ref. [41], reporting $\kappa_{\text{exp}} = 0.13$ mm^{-1}. However, it is worth mentioning that the range of examined orifice sizes is narrower than in the experiments [41], due to higher probability of clogging obtained numerically.

4.3.2 Continuum analysis of the particle flow

To gain insight into how the macroscopic properties of the flow are related to the flow patterns inside the silo, we employ a coarse-graining methodology, and derive the most relevant macroscopic fields from the data provided by the DEM simulations (see Sec. 4.2). In Fig. 4.6, the colormaps represent the spatial profiles of the packing fraction $\phi(r,z)$. The data presented in rows I-III correspond to rotation frequencies $f = 0.0, 0.32,$ and 1.28 Hz (up-down), respectively. The graphs included in each column illustrate the system at different stages of the process, the indicated time is measured from the beginning of the discharge. Although the computation is done in cylindrical coordinates, the fields represent spatial averages in the azimuthal direction $\phi(r,z)$, within a time window of 1 s, ± 0.5 s around the indicated time instant. Note that the fluctuations are larger in the center of the silo due to the cylindrical averaging having less data points there. Furthermore, the orifice region also shows larger noise; consequently, it should not be taken as representative of the whole discharge process.

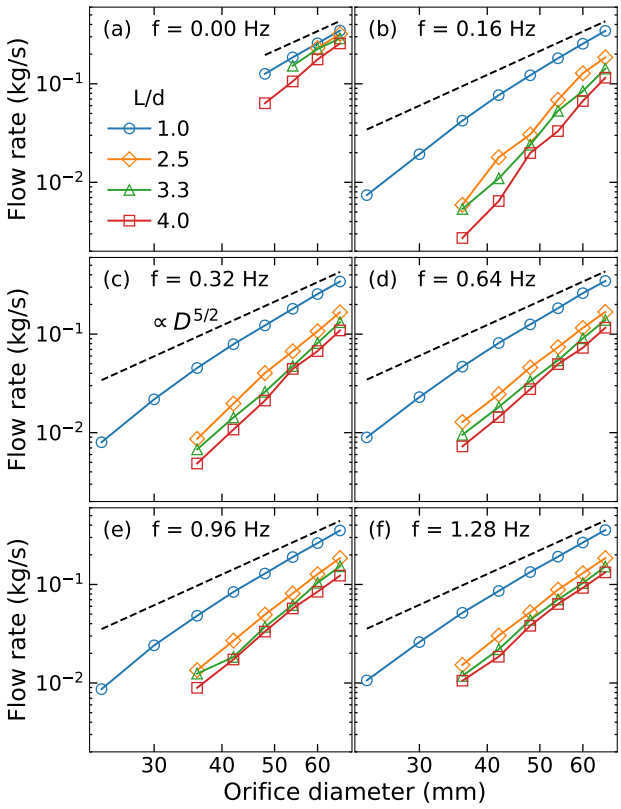

Figure 4.4: Log-log plot of the discharge rate as a function of orifice size. The different panels (a)-(f) correspond to different bottom rotation frequencies $f = 0, 0.16, 0.32, 0.64, 0.96, 1.28$ Hz respectively, as indicated inside them, while each curve presents data for a specific particle aspect ratio shown in the legend. The back dashed line represents a power-law function with an exponent of $5/2$.

As mentioned earlier, in Fig. 4.6 the silo with a fixed bottom wall is again used as a baseline, which denotes the presence of *funnel type* of flow pattern. It is worth mentioning that this pattern is more noticeable when examining more elongated particles (see the Supplementary Material Sec. 4.5). This is characterized by a low-density region at the center of the silo and by the presence of a stagnant zone close to the lateral walls. Moreover, a surface depression is formed in the central region. Interestingly, two significant changes occur when the bottom wall rotation is applied to the system: the top surface of the column becomes flat, and the funnel-shaped low packing fraction region disappears. A less visible change happens near the bottom wall, where the stagnant zone disappears, and the external shear causes a slight dilation (see below about $z/R < 0.4$). We also note that the low packing fraction region in the center near the orifice at $f = 1.28$ Hz shrinks compared to the $f = 0.32$ Hz case. The spatial distributions of other particle elongations show qualitatively the same response to the rotational shear (see Sec. 4.5). Similar to previous studies of flow of elongated particles [112, 112, 124], we also obtained a significant increase of the orientational ordering and the particle realignment in the sheared regions. These feactures were quantified using the orientational field $O_{zz}(r,z)$ and nematic order $S(r,z)$ fields (see Supplementary Material Sec. 4.5).

The flow pattern features are also highlighted by the color maps of the magnitude of the in-plane

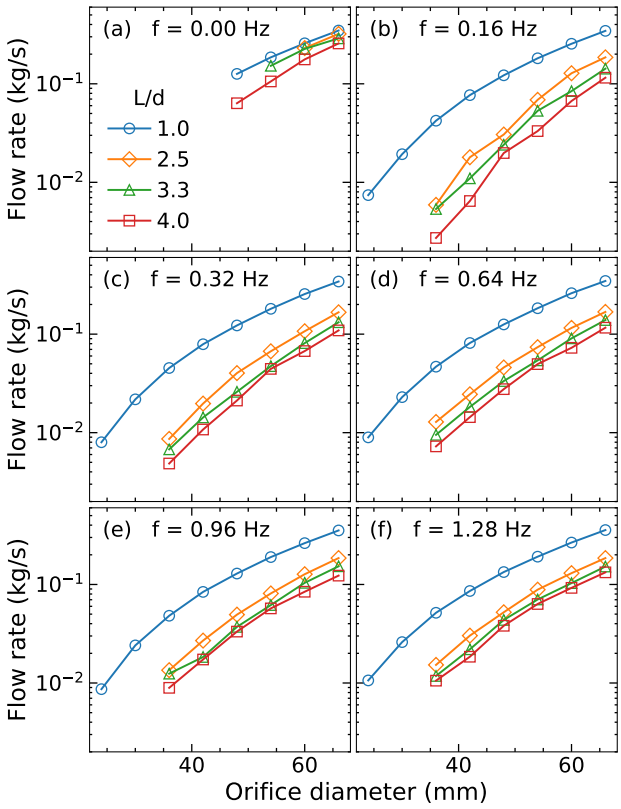

Figure 4.5: Semilog plot of the discharge rate as a function of orifice size. The different panels (a)-(f) correspond to different bottom rotation frequencies $f = 0, 0.16, 0.32, 0.64, 0.96, 1.28$ Hz respectively, as indicated inside them, while each curve presents data for a specific particle aspect ratio shown in the legend.

speed $v = \sqrt{v_r^2 + v_z^2}$ (see Fig. 4.7). For clarity, the panels also include the streamlines of $v(r,t)$, drawn with the radial and the vertical components. Columns and rows represent the same cases illustrated in Fig. 4.6. In the absence of external shear (stationary bottom wall), the velocity fields are rather heterogeneous, denoting a *funnel flow* pattern with strong velocity gradients in the radial direction. The streamlines are considerably curved, drawing a complex flow pattern. Moreover, at the center of the silo, the material speed $|v(r,t)|$, is significantly larger in comparison with the region close to the wall (stagnant zone), and $|v(r,t)|$ significantly increases in the region of the orifice.

Interestingly, the appearance of the *mass flow* pattern seems counterintuitive, since the rotation of the bottom induces the movement of the grains in the tangential direction. It would pair with an outwards pointing fictitious force in the rotating frame. Thus, it would imply that particles go to the lateral wall of the silo, similar to what happens to water when it is put into a rotating cylinder. As our results indicate (see Fig. 4.6), this is not the case, and it is explained by the low magnitude of the fictitious force. Instead, we argue that the *mass flow* pattern emerges since the stability of the stagnant zone is affected by the rotational shear. As a result, particles are mobilized by the momentum transfer of the bottom wall, inducing the system's dilatancy and the reduction of the effective friction. Consequently, the gravity action drives the homogeneous advective particle flow, and the material moves down the silo

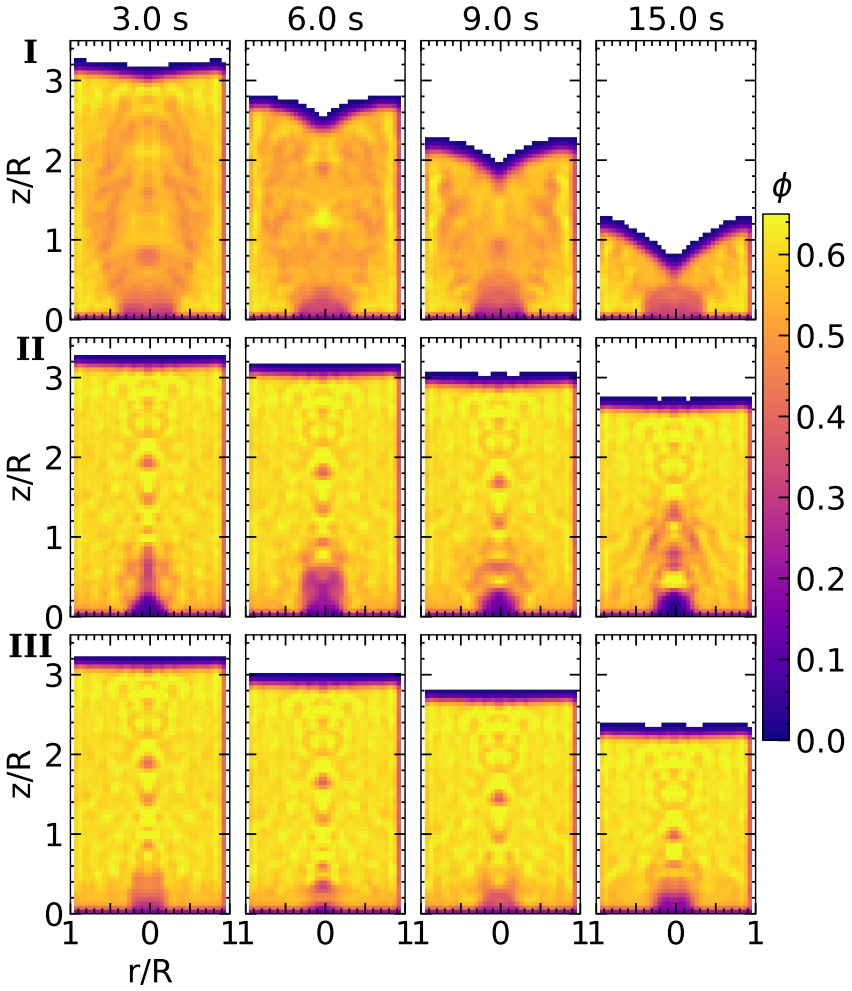

Figure 4.6: Color map representation of the spatial distribution of the packing fraction for elongated particles of $L/d = 3.3$, next to an orifice with size $D = 54$ mm. The rows correspond to $f = 0.0$, 0.32, and 1.28 Hz in order. The different columns show the packing fraction in different instants of time as indicated above.

as a column (see Fig. 4.7).

Next, we thoroughly investigate the cause of the sharp decrease in Q, when applying the external shear, focusing on the details of the particle flow in the region of the orifice. The volumetric flow rate Q through a surface is defined as the integral of the density times the velocity perpendicular to the surface $Q = \int \rho_p \phi(r) v(r)\, dA$. Thus, to better quantify and differentiate the roles played by $v(r)$ and $\phi(r)$ in relation to the flow rate, we have averaged these quantities in the area of the orifice during the stationary part of the flow, namely, computing the mean of the quantity $X(= v_z, \phi, O_{zz}, ...)$ using the formula $\langle X \rangle = \frac{\int X(r)\phi(r)\, dV}{\int \phi(r)\, dV}$. Here we use $\phi(r)$ as a weight to account for the different number of particles in different cells. The region of averaging is a 1 cm high cylinder which has its base at the orifice and its diameter is the same as the orifice size D. After this spatial integration, time and ensemble averaging is also applied. The panels in Fig. 4.8 illustrate the dependence of $\langle \phi \rangle$ and $\langle v_z \rangle$ on the rotational frequency f, obtained for particles with several aspect ratios at an orifice diameter of

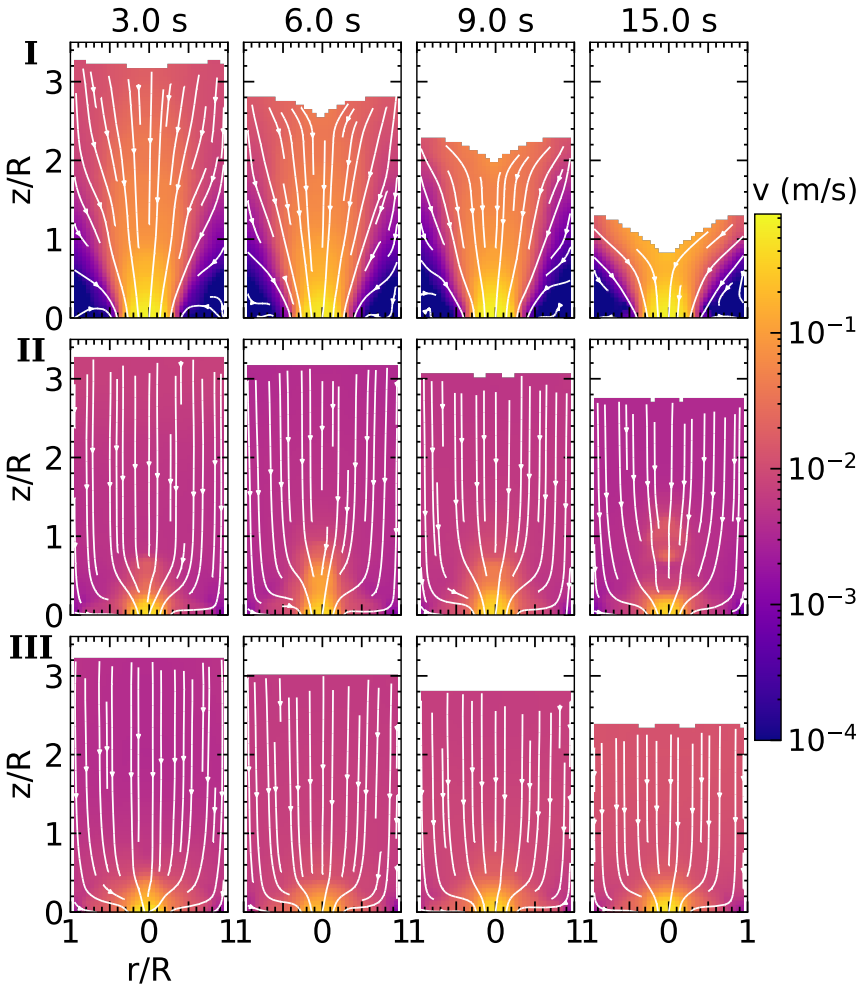

Figure 4.7: Coarse-grained velocity fields (excluding tangential component) inside the silo for spherocylinders with $L/d = 3.3$, next to an orifice with size $D = 54$ mm. The rows correspond to $f = 0.0$, 0.32, and 1.28 Hz in order. The different columns show the velocity maps in different instants of time, as indicated above. Additionally, the streamlines have been added with white on top of the color maps.

$D = 60$ mm. Interestingly, the evolution of $\langle\phi\rangle$ suggests a slightly increasing trend for spheres but a nonmonotonic behavior for rods, when varying f (see first panel of Fig. 4.8). However, the magnitude of the $\langle\phi\rangle$ variation does not justify the abrupt decay of the particle flow rate of the rods. Contrarily, when raising the rotational frequency f the particles notably slow down and a significant reduction of $\langle v_z\rangle$ is observed (see second panel of Fig. 4.8). In fact, it strongly correlates with the trend of $Q(f)$ (see Fig. 4.2), meaning that it is the larger contributing factor to the flow rate. Nevertheless the increase of the flow rate for $f > 0.3$ Hz can only be explained by the increase of $\langle\phi\rangle$. Additionally, the third panel of Fig. 4.8 displays the evolution of the averaged kinetic pressure $\langle p_k\rangle = Tr\left(\langle\sigma^k\rangle\right)$. The latter quantity is often interpreted as a granular temperature since it is proportional to the square of the velocity fluctuations. As observed in the figure, the behavior of $\langle p_k\rangle$ is also in line with the obtained trend for Q vs f, even resembling the slight nonmonotonic response reported earlier for spheres [123].

Furthermore, we also inspect the influence of the rotational shear on the particle orientation. Per-

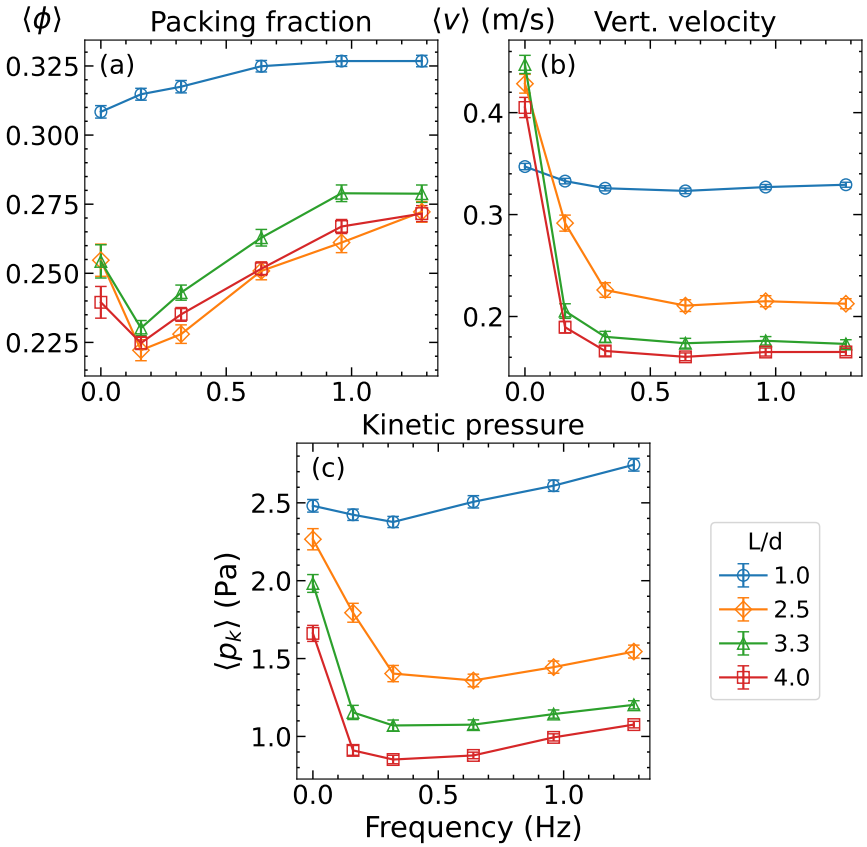

Figure 4.8: Macroscopic quantities averaged in the region of the orifice as a function of the rotation frequency: (a) packing fraction, (b) vertical velocity and (c) kinetic stress. Different curves correspond to different particle aspect ratios, as shown in the legend, all for the case of a fixed orifice diameter $D = 60$ mm.

forming the analysis, the attention focuses on the response of the diagonal components (in cylindrical coordinates) of the orientation tensor $\langle O_{ii} \rangle$, averaged in the region of the orifice. Figure 4.9 displays the diagonal elements, averaged in the same way as the quantities in Fig. 4.8, as well as the mean nematic order $\langle S \rangle$. To obtain a meaningful measure of the actual particle order, first we averaged the orientation matrix in the region of the orifice and using the largest eigenvalue of this matrix we carried out ensemble and time averaging to acquire $\langle S \rangle$. Interestingly, the graph indicates that in the absence of external shear ($f = 0$ Hz), the rods achieve an orientation parallel to the flow direction, which is indicated by the high value of $\langle O_{zz} \rangle$, in comparison with $\langle O_{rr} \rangle$ and $\langle O_{tt} \rangle$. However, there is an abrupt change in the orientation of the particles even when a weak rotation is applied. Specifically, the grains seem to prefer a more horizontal (radial) direction compared to the vertically aligned case with the stationary bottom. Interestingly, this effect is stronger for longer particles, denoting that more elongated particles seem to face the orifice with a larger effective size. Note that the decrease of $\langle O_{zz} \rangle$ is in the same order of magnitude as the increase in $\langle O_{rr} \rangle$ for small f. There are two contributing factors that can explain the latter. On one hand horizontal particles lying on the silo bottom are being pushed towards the orifice due to the mass flow pattern (see Fig. 4.7). On the other hand particles coming from above the orifice are more horizontally aligned (see Sec. 4.5) since they are not sheared (mass flow) until very

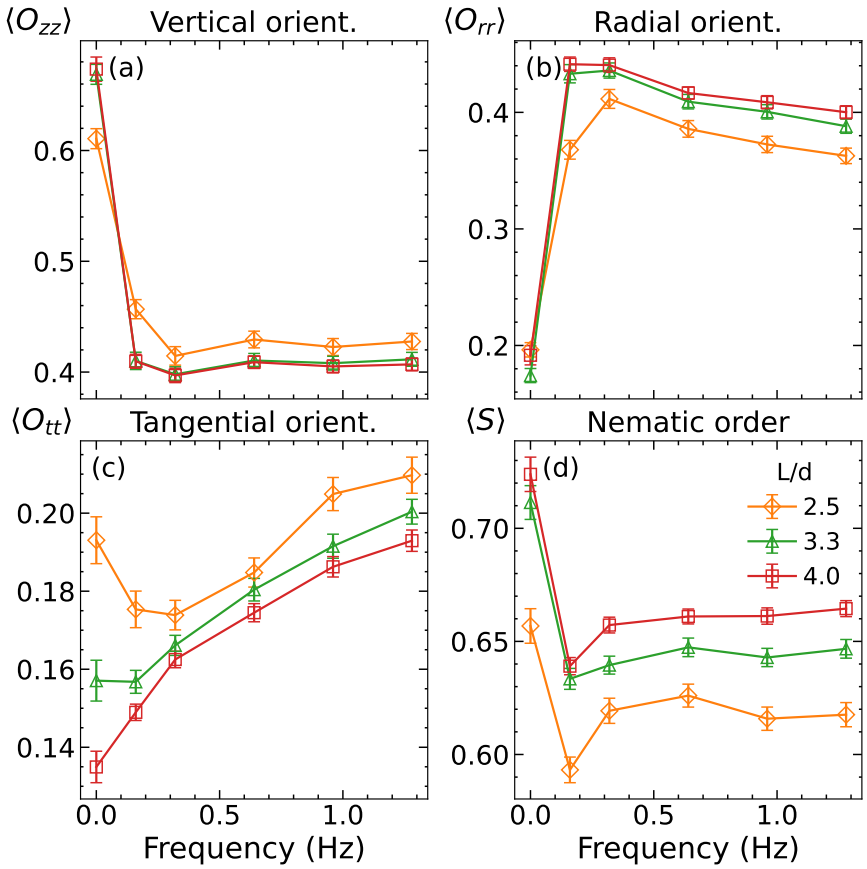

Figure 4.9: Mean value of the orientation quantities averaged in the region of the orifice: (a) vertical, (b) radial, (c) tangential orientation, and (d) nematic order. Different curves correspond to different particle aspect ratios as shown in the legend, all for the case of a fixed orifice diameter $D = 60$ mm. The inset shows the radial component of the orientation tensor.

near the orifice, while in the stationary bottom case, grains align more vertically due to the shear [125]. Once again, we can argue that this tendency totally correlates with the trend of the particle flow rate (see Fig. 4.2). The orientation in the azimuthal angular direction $\langle O_{tt} \rangle$ is of low magnitude but shows a nonmonotonic or increasing trend with increasing f, which can be accounted to the better alignment of grains due to the external shear. Curiously, the order of the particles $\langle S \rangle$ reduces when a slow rotation is applied but increases by further increasing the frequency, which is in correlation with the packing fraction $\langle \phi \rangle$. These findings suggest that the level of alignment and ordering of the particles determines the macroscopic volume fraction at the orifice, impacting indirectly the macroscopic flow rate Q.

In silo discharge, it is known that the particle dynamics in a distinct region above the orifice determines the exit velocity $v_z|_{z=0}$ [74]. Thus, the magnitude of $v_z|_{z=0}$ can be derived from the integral of the momentum balance equation. Figure 4.10 shows the profiles of mean acceleration $a_{\text{eff}}(z)$, obtained for several particle elongations; for comparison, the inset illustrates the data for spheres. We define $a_{\text{eff}}(z) = \langle \frac{\Delta v_i}{\Delta t_p} \rangle$, where $\langle \Delta v_i \rangle$ is the mean of velocity difference of individual particles in two consecutively printed time steps ($\Delta t_p = 50$ ms). The spatial averaging was computed in the middle of the silo along the vertical axis within a cylinder with diameter $D/2$, and the time averaging during the stationary part

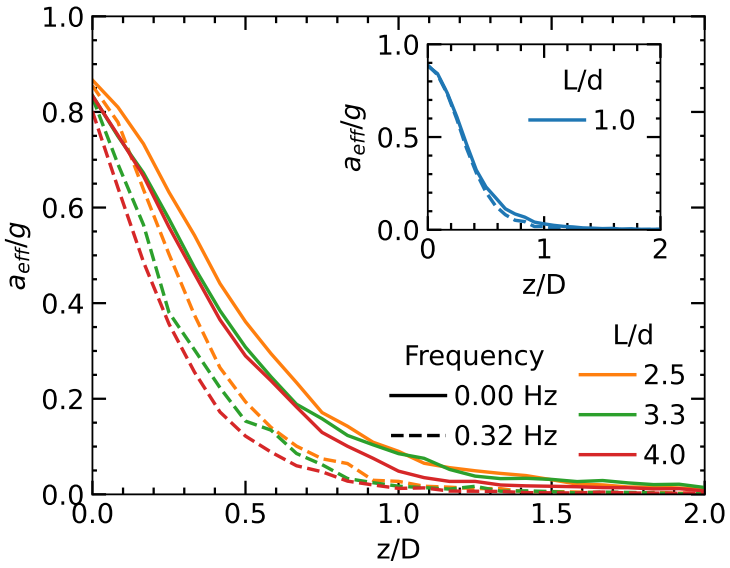

Figure 4.10: Relative vertical acceleration a_{eff}/g of particles in the middle of the silo along the vertical axis averaged in a cylinder with diameter of 3 cm. The x axis is normalized by the orifice size, which was $D = 60$ mm in this case. Solid lines correspond to stationary bottom, while the dashed lines for rotational with $f = 0.32$ Hz. The inset includes the case of the spheres for comparison.

of the flow. The graphs include the data corresponding to a rotational velocity of $f = 0.32$ Hz, and the stationary case. From these results, the message is conclusive. For flows of nonspherical particles, the rotational shear induces a sharper increase of the acceleration $a_{\text{eff}}(z)$ when approaching the exit (see dashed lines). This means that the region where the grains are accelerating is less extended for a silo under external rotational shear compared to the case of a silo with nonmoving bottom. In other words, the height of the so-called *free fall arch* region appears to be shrinking due to the applied rotational shear. As a result, the areas under the curves are significantly lower than those of the static cases (see continuous lines). Remarkably, it explains the abrupt decrease of the particle velocity (and flow rate) produced by the external rotational shear, obtained for elongated grains numerically and experimentally [41]. Examining flows of spheres (see inset of Fig. 4.10), however, the difference between the perturbed and nonperturbed case results is notably smaller. Consequently, the mean velocity at the orifice and the particle flow rate are only affected slightly. It is worth mentioning that the same behavior is observed when exploring other rotation frequencies (see Supplementary Material Sec. 4.5).

4.4 Summary

We executed a numerical analysis of the discharge of elongated particles from a silo with a rotating bottom. Interestingly, we obtain that introducing a small transverse shear might reduce the flow rate Q by up to 70% compared to a stationary bottom and by further increasing f, the value of Q increases. We find that the relative increase is much larger in the case of rods, specifically it is larger for longer rods and smaller orifices. These macroscopic observations are in very good agreement with our earlier experimental findings [41]. Stepping forward, we extend the analysis, enlarging the domain of particle

elongations and the effective particle diameters. Focusing attention on the dependency of the flow rate Q on the orifice diameter D, the spheres and rods show two distinct trends. In the cases of rods, in the limit of small apertures, we obtain power-law relation but with a larger exponent, although in the limit of large orifices, the power-law correlation $Q \sim D^{5/2}$ is also reproduced. However, the obtained results are also compatible with an exponential trend $Q \sim e^{\kappa D}$, when decreasing the orifice diameter. Very similar results have been recently obtained experimentally (see Ref. [41]). However, it is worth mentioning that the range of examined orifice sizes is narrower than in the experiments [41], due to the higher probability of clogging obtained numerically. The reason behind the exponential trend obtained experimentally [41] and numerically is nontrivial. However, in the small orifice limit, the particles flow out of the silo practically one by one, and the particle flow could be understood as a stochastic process with a constant probability of passing. Employing a coarse-graining methodology, we compute the most relevant macroscopic fields of the particle flow. Their analysis allows us to detect a transition from a funnel to a mass flow pattern as a result of the applied external shear. The averaged fields in the orifice region reveal that the initial decrease in Q is mainly attributed to the velocity changes. Besides, the increase of the packing fraction near the orifice explains the increase in Q for large rotation frequencies. Furthermore, the flow rate correlates with the particle orientation in the vertical direction and the packing fraction with the order of grains in the region of the orifice. Finally, we also found that the vertical profiles of mean acceleration at the center of the silo are notably affected by the rotation of the bottom wall. In flows of elongated rods, it is observed that the region where the acceleration is not negligible (so-called *free fall arch region*) shrinks significantly due to the perturbation induced by the moving wall.

4.5 Supplementary material

This supplementary material includes figures that are not essential for understanding our main arguments but may provide additional insight for the interested. The coarse-grained fields were computed as it is described in section II of the main document. Fig. 4.11a and Fig. 4.11b show the orientational field O_{zz} and nematic order field S, respectively. The illustrated data correspond to the same cases introduced in Figure 6 of the main document. Complementary, Figures 4.12 and 4.13 display the packing fraction and velocity fields of the discharge process for two elongations but for a slightly different orifice size ($D = 60$ mm) than what is presented in the article due to clogging in one case.

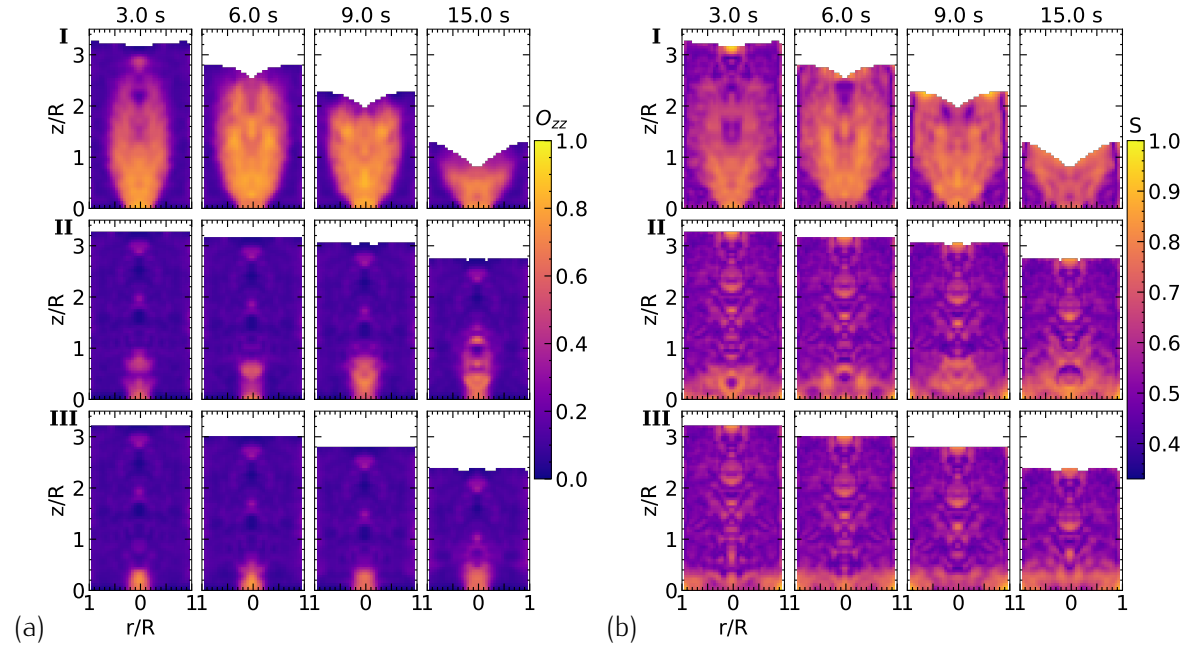

Figure 4.11: Color map representation of the particle vertical orientation O_{zz} (a) and nematic order S (b) for elongated particles of $L/d = 3.3$, next to an orifice with size $D = 54$ mm. The rows correspond to $f = 0.0, 0.32,$ and 1.28 Hz in order. The different columns show the data in different instants of time as indicated above.

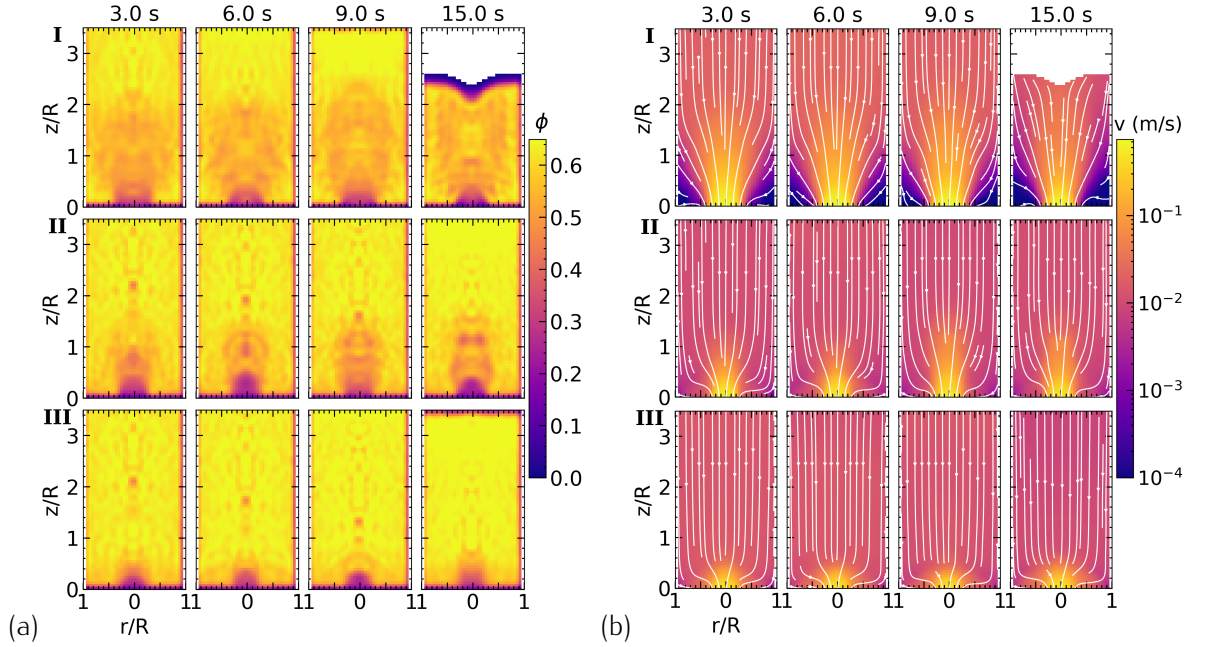

Figure 4.12: Color map representation of the packing fraction (a) and in-plane velocity (b) for elongated particles of $L/d = 2.5$, next to an orifice with size $D = 60$ mm. The rows correspond to $f = 0.0, 0.32,$ and 1.28 Hz in order. The different columns show the data in different instants of time as indicated above.

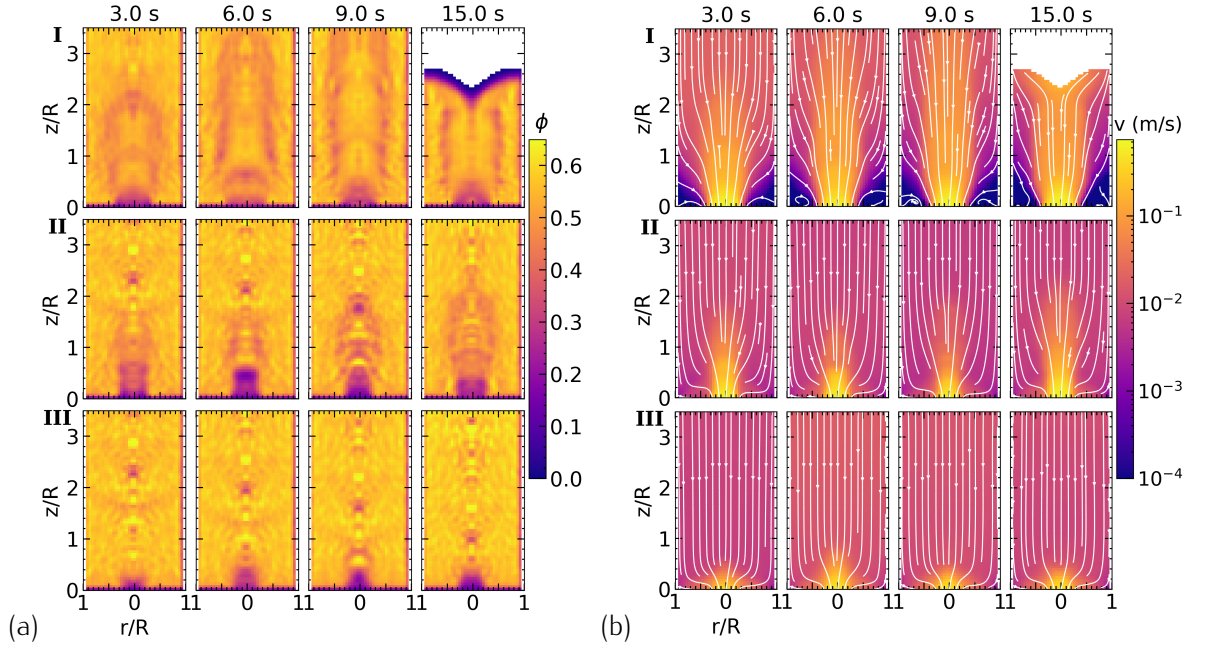

Figure 4.13: Color map representation of the packing fraction (a) and in-plane velocity (b) for elongated particles of $L/d = 4.0$, next to an orifice with size $D = 60$ mm. The rows correspond to $f = 0.0, 0.32,$ and 1.28 Hz in order. The different columns show the data in different instants of time as indicated above.

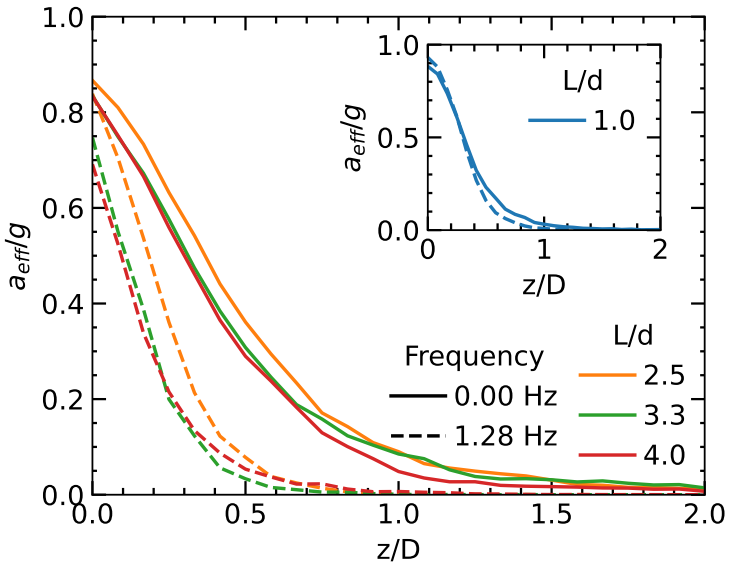

Figure 4.14: Relative vertical acceleration a_{eff}/g of particles in the middle of the silo along the vertical axis averaged in a cylinder with diameter of 3 cm. The x-axis is normalized by the orifice size, which was $D = 60$ mm in this case. Solid lines correspond to stationary bottom, while the dashed lines for rotational with $f = 1.28$ Hz. The inset includes the case of the spheres for comparison.

Chapter 5

Continuously heated granular gas of elongated particles

Tivadar Pongó, Dmitry Puzyrev, Kirsten Harth, Ralf Stannarius, and Raúl Cruz Hidalgo

EPJ Web of Conferences **249** 04003 (2021) DOI: 10.1051/epjconf/202124904003

Some years ago, Harth et al. experimentally explored the steady state dynamics of a heated granular gas of rod-like particles in microgravity [K. Harth et al. *Phys. Rev. Lett.* **110**, 144102 (2013)]. Here, we report numerical results that *quantitatively* reproduce their experimental findings and provide additional insight into the process. A system of sphero-cylinders is heated by the vibration of three flat side walls, resulting in one symmetrically heated direction, one non-symmetrically heated direction, and one non-heated direction. In the non-heated direction, the speed distribution follows a stretched exponential distribution $p(v) \propto \exp(-(|v|/C)^{1.5})$. In the symmetrically heated direction, the velocity statistics at low speeds is similar but it develops pronounced exponential tails at high speeds. In the non-symmetrically heated direction (not accessed experimentally), the distribution also follows $p(v) \propto \exp(-(|v|/C)^{1.5})$, but the velocity statistics of rods moving toward the vibrating wall resembles the indirectly excited direction, whereas the velocity statistics of those moving away from the wall resembles the direct excited direction.

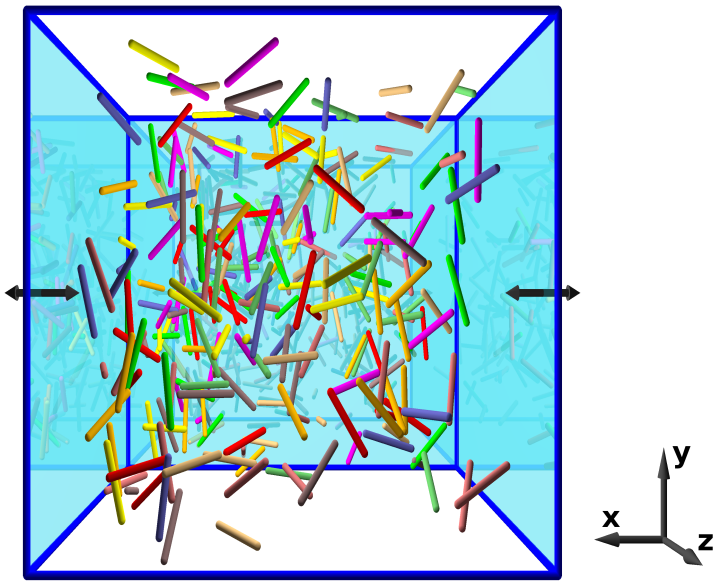

Figure 5.1: Dilute system of $N = 256$ spherocylinders with aspect ratio $\zeta = 9.2$. The blue walls vibrate in their normal direction as described in the text.

Granular media surround us in everyday life. For instance, while walking on a sandy beach our weight is supported by a complex granular force network that draws our footprint in the sand. Besides, centuries of human technological revolution have made possible the handling of many types of particles and grains [126]. Thus, theoretical approaches of granular media are always needed, due to its massive scale of use in industrial processes, and the role they play in many natural phenomena.

Most of the time we observe granular media to exhibit a solid or liquid-like behaviour. However, when dilute granular systems are sufficiently excited, they enter into a gas-like state, which is characterized by a very low collision rate between the grains [127, 128]. The dissipative nature of the interactions differentiates such granular gases from usual molecular gases. Indeed, this property makes these out-of-equilibrium systems interesting from the view of fundamental questions of statistical physics, and sometimes even tricky. Such lose ensembles of granular matter occur, e.g. in planetary rings, but also in industrial processes wherever granular materials are strongly excited.

In the past, kinetic and hydrodynamic theories have described the macroscopic properties of granular gases with and without external energy input. When considering the most simple case, the free cooling of an ensemble of spherical particles with constant restitution coefficient, the granular temperature diminishes in time following Haff's law resulting in an asymptotic decay $T \propto t^{-2}$ [129–133]. For freely cooling gases of visco-elastic particles, the exponent of the asymptotic algebraic decay of the granular temperature reduces to $T \propto t^{-5/3}$ [134]. However, in many cases the particles' interactions are over-simplified, and even fewer quantitative validations against actual experimental data exist.

In the nineties, first systematic studies of ensembles of needles addressed the impact of particle shape on the kinetic evolution of granular gases [135]. More recently, there has been an increasing interest in the dynamics of dilute granular ensembles composed of non-spherical grains, both experimentally [43, 131, 132, 136–138] and numerically [114, 139–142].

Experiments investigating the dynamics of elongated particles in a continuously heated steady state were carried out in microgravity by Harth et al. [43, 137]. They found that the velocity distributions in the indirectly excited direction were not far from a Gaussian behavior, but much better approximated by a stretched exponential distribution $p(v_y) \propto \exp\left[-\left(|v_y|/C\right)^{1.5}\right]$. The same applies for the rotational velocity distributions. In the directly heated direction, the low-velocity parts of $p(v_x)$ agree well with $p(v_y)$, while pronounced exponential high-velocity tails are observed. Regarding the spatial distribution of particles, no significant persistent inhomogeneities were observed.

In our contribution to Powders & Grains 2021, we report numerical results that reproduce quantitatively the experimental results introduced in Refs. [43, 137] and provide additional insight into the process. Our numerical data complement the experimental analysis, accessing the dynamic evolution of each particle in detail. The paper is organized as follow: In section 5.1, the numerical model is described briefly. In section 5.2, the numerical data is provided, while our main results are compared with the experimental data. Finally, several further work ideas are mentioned.

5.1 Numerical model

We used a home-made hybrid GPU-CPU discrete element algorithm (DEM) introduced earlier [114, 140]. This numerical tool was adapted to simulate confined systems with moving walls. The model considers an ensemble of $N = 256$ spherocylinders with length L and sphero-radius r, defining an aspect ratio of $\zeta = L/(2r)$. The interaction force between two particles i and j, $\vec{F}_{ij}$, is obtained using an algorithm of interacting spheropolygons [115]. The particular case of the spherocylinder is described by two vertices and the spheroradius; thus, its surface is delineated by all the points at distance r from the edge defined by the two vertices. The problem of contact detection between the spherocylinders reduces to the determination of the closest point between two edges. Thus, the overlap distance δ results from the simple overlap of two spheres of radius r. For the interaction between the particles and the walls, we used the same model but assuming the interaction of a spherocylinder with an infinite moving plane. Figure 5.1 displays a snapshot of the system composed of spherocylinders. The walls on the sides and in the back vibrate sinusoidally (colored blue), the others are stationary. The simulation limits are marked by the wire-frame.

The force $\vec{F}_{ij}$ acting on particle i by the particle j can be decomposed as $\vec{F}_{ij} = F^n \cdot \vec{n} + F^t \cdot \vec{t}$, where F^n is the component normal to the contact plane and F^t acts in tangential direction $\vec{t}$. Here, the normal interaction F^n is a linear elastic force, depending on the overlap distance δ^n between two spherocylinders. The normal dissipation is included using a velocity dependent viscous damping. The total normal force reads $F^n = -k^n\delta^n - \gamma^n v^n_{rel}$, where k^n is the spring constant in the normal direction, γ^n is the normal damping coefficient and v^n_{rel} is the normal relative velocity between the contacting particles i and j. The tangential force F^t also contains an elastic term and a tangential frictional term accounting for static friction between the grains. Taking into account Coulomb's friction constraint, which reads $F^t = \min\{-k^t\xi - \gamma^t \cdot |v^t_{rel}|, \mu F^n\}$, where γ^t is the damping coefficient in tangential direction, v^t_{rel} is the tangential component of the relative contact velocity of the overlapping pair. ξ represents the elastic deformation of an imaginary spring with spring constant k^t at the contact, which increases as $d\vec{\xi}(t)/dt = \vec{v}^{\,t}_{rel}$ as long as there is an overlap between the interacting particles. The elastic tangential

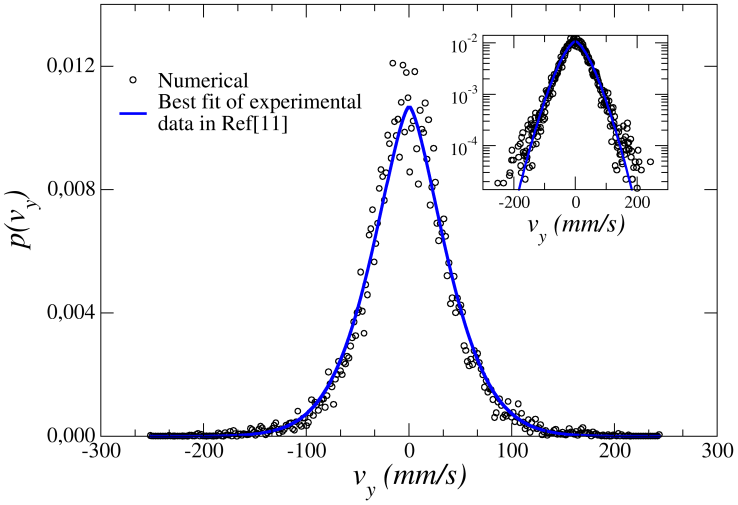

Figure 5.2: Speed distribution $p(v_y)$ on the y direction (non-moving walls), obtained for $A = 1$ mm and $f = 30$ Hz. The inset shows the same but in semi-log. The best fit of the experimental distribution of v_y from Ref. [43] is shown for comparison.

elongation $\vec{\xi}$ is kept orthogonal to the normal vector (truncated if necessary) [118], μ is the friction coefficient. A velocity Verlet numerical algorithm [3] integrated the 3D translational equations of motion of each particle, while the rotational degrees of freedom were resolved using a modified leap-frog algorithm [143].

Similar to the experimental setup of [43], we defined a rectangular container delimited by walls with dimensions $X = [-4.0; 4.0]$ cm, $Y = [-5.0; 5.0]$ cm and $Z = [-4.25; 4.25]$ cm. In the experiment described in Ref. [43, 137], the dimensions were $\Delta X = 8.5$ cm, $\Delta Y = 10$ cm, and $\Delta Z = 6.5$ cm. The two X-walls, as well as one of the Z walls moved sinusoidally in their normal direction with a fixed amplitude A and frequency f. The other three walls were fixed. The particle aspect ratio was $\zeta = 9.2$, *i.e.* $L = 12$ mm, $r = 0.65$ mm, and mass $m = 0.046$ g. Moreover, we have used a particle Young modulus of $Y = 10$ GPa and a restitution coefficient of $e_n = 0.6$. The friction coefficient of the particle-particle contact was $\mu_p = 0.1$, while for the particle-wall contacts $\mu_w = 0.2$.

In our analysis, we assume that the system is in steady state conditions. Initially, the particles are randomly distributed within the system domain, and the particle speeds are randomly generated in the range $[-0.1; 0.1]$ mm/s. Then, the excitation begins, and after a short transient, the system reaches a steady state characterized by a non-increasing mean kinetic energy. For each excitation condition (fixing A and f), the particle velocities are sampled during 20 seconds of simulation time.

5.2 Results and discussion

As mentioned before, here we focus on the system kinetics in steady state conditions, where the statistics of the particle linear speeds is described, in detail. The distributions are sampled, including particles away from the walls, at a distance $\delta > L/2$, where L is the longer side of the particles.

Figure 5.2 shows the translational velocity distribution $p(v_y)$ in the non-directly excited direction y (no moving wall), obtained for an oscillation amplitude of $A = 1$ mm and frequency $f = 30$ Hz.

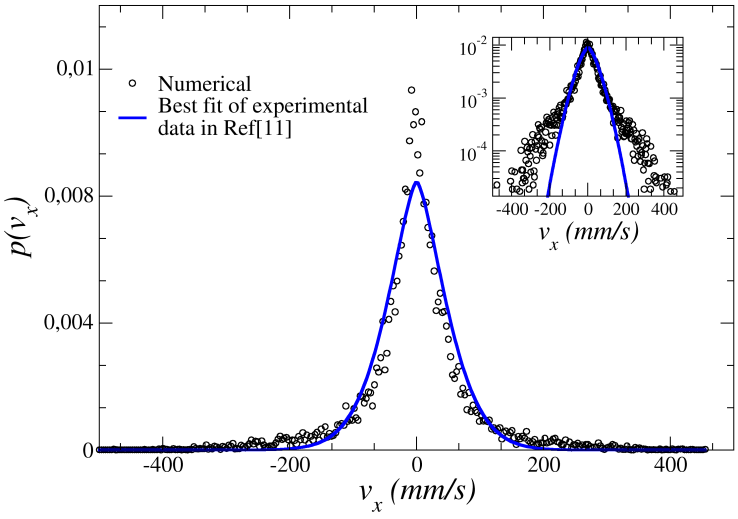

Figure 5.3: Speed distribution $p(v_x)$ in the x direction (two moving walls), obtained for $A = 1\,\text{mm}$ and $f = 30\,\text{Hz}$. The inset shows the same but in semi-log scale. In both cases, the best fit of the experimental data Ref[43] is also shown for comparison.

Note that our numerical data agree very well with the fit to the experimental data [43] shown in blue, $p(v_y) = 0.012 \exp\left[-\left(|v_y|/C_y\right)^{1.5}\right]$, with $C_y = 51.77$ mm/s. The standard deviation of the data set is $\sigma_y = 42.2$ mm/s, resembling the experimental value $\sigma_y^{\text{exp}} = 43.9$ mm/s [43]. Note that no significant fat tail is observed on the semi-log scale, which is consistent with the fact that there is practically no missing area in the low velocity range.

This result is in contrast to previous numerical observations of the cooling process of ellipsoids [139] and spherocylinders [114], *i.e.* without excitation and using periodic boundary conditions. In those cases, Gaussian velocity distributions without fat tails were obtained. However, another experimental study, carried out with similar rod-like particles (in confined conditions), observed non-Gaussian velocity distributions even in the scaling regime of granular cooling [131]. Our validated simulations may aid to reveal the origin of this discrepancy in future work.

Figure 5.3 illustrates the velocity distribution $p(v_x)$, obtained in the directly excited direction x (two moving walls), for oscillation amplitude of $A = 1\,\text{mm}$ and frequency $f = 30\,\text{Hz}$. Once again with reasonable accuracy, we find the statistics agree with a stretched exponential $p(v_x) = 0.008 \exp\left[-\left(|v_x|/C_x\right)^{1.5}\right]$, with $C_x = 65.5$ mm/s and standard deviation $\sigma_x = 75.6$ mm/s. Note, the same functionality and fitting parameters were used, when describing the experimental data [43], and result in a standard deviation of $\sigma_x^{\text{exp}} = 70.8$ mm/s [43]. Moreover, both the numerical and experimental data exhibit fat tails in the high velocity regime, which are not captured by the stretched exponential fit (see inset of Fig. 5.3) and Ref. [43]). Here, we can argue that the small deviations come from the slightly different container geometry and from possible artifacts due to the perspective view in the experiment. We also observe a slight accumulation of rods near the non-moving walls. So, when analysing the whole data (without the $\delta > L/2$ condition), the distributions show a slightly larger probability of slow particles, while the shape of the tails do not change significantly.

Additionally, the simulations also allow accessing the particle velocity in the direction where the

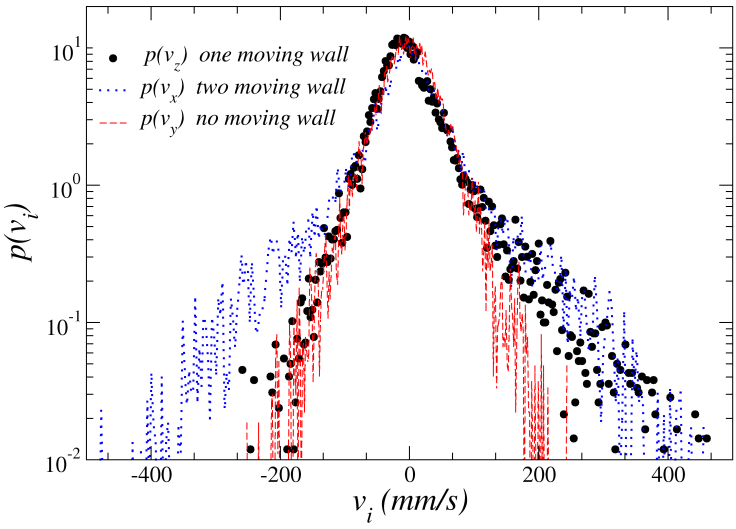

Figure 5.4: Speed distributions obtained in the three Cartesian directions ($p(v_x)$, $p(v_y)$, $p(v_z)$). Note the direction with one moving wall could not be accessed experimentally.

system is non-symmetrically heated (only one moving wall). Note, this data was not accessible in experiments due to technical reasons [43, 137]. The statistics corresponding to this degree of freedom is shown in Fig. 5.4 together with the data of the previously analyzed directions. Remarkably, the velocity distribution $p(v_z)$ becomes asymmetric, reflecting the single-sided excitation. The part of the distribution corresponding to negative velocities (towards the moving wall) agrees with $p(v_y)$, whereas the part at positive velocities (away from the moving wall) agrees with $p(v_x)$. Namely, the heated direction exhibits a fat tail, while the non-heated one does not. This result might suggest that the fixed walls behave as an energy sink, removing any trace of the direct excitation once grains have reversed their z-direction of the motion.

Our numerical simulations allow us to perform a systematic study of the system's dynamics when changing the heating intensity. Figure 5.5 displays the scaled velocity statistics obtained for outcomes corresponding to several heating intensities, varying the amplitude $A = [1; 1.8; 2]$ mm and the frequency $f = [15; 20; 25; 30]$ Hz as shown. In all cases, the velocity values have been scaled with $v_c = 2\pi f A$, *i.e.* the maximum wall velocity. Interestingly, all the scaled speed distributions collapsed on the same curve. The latter indicates that the maximum velocity of the moving walls v_c is the relevant characteristic value, denoting that the steady state energy of the system is controlled by the walls. These outcomes would corroborate the guess made in Ref. [43], that the kinetic energy in the system scales with $v_c^2 \propto A^2 f^2$, and not the peak acceleration of the walls. It is interesting to note that the energy gain of a *single* rod bouncing on a plate in this range of excitation parameters under normal gravity rather scales $\propto A^{1.5} f$ instead [144]. We may assume that either microgravity conditions or collective effects alter the scaling of the energy input into our granular gases of rod-like grains.

Outlook: The velocity distribution functions and scaling laws described above require additional investigation and explanation from the point of view of individual rod collision dynamics (with the walls and among rods), whose accurate modeling can still be improved by detailed comparison of experimental and numerical single-collision data. A second important aspect is the identification of

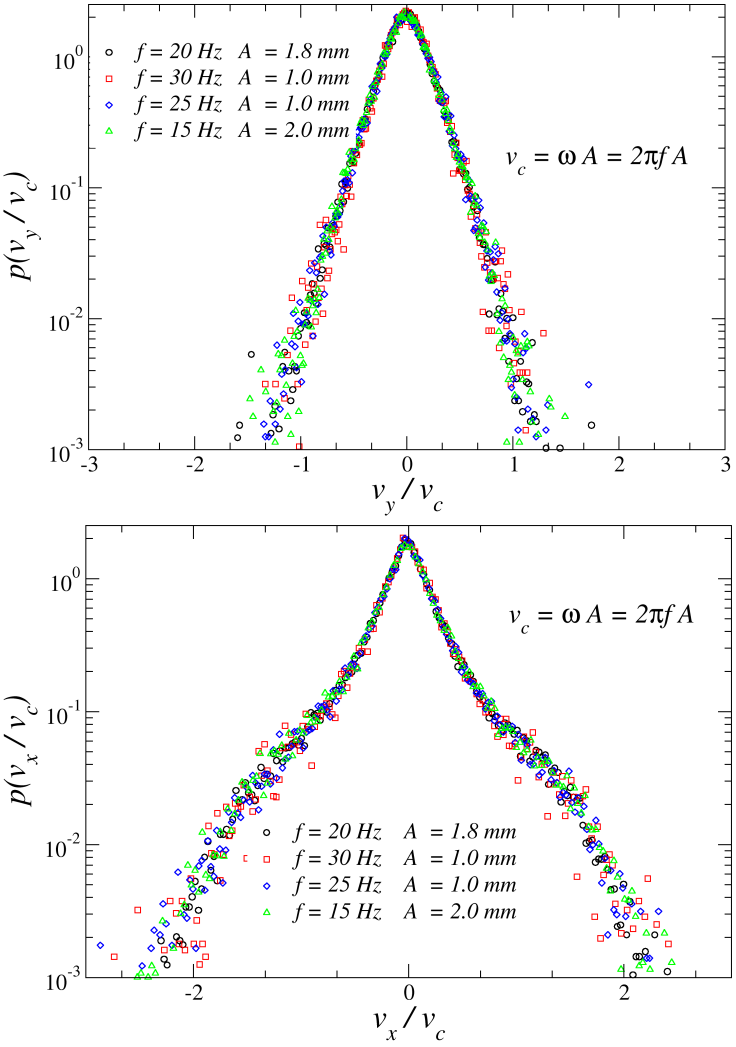

Figure 5.5: Scaled velocity distributions $p(v_y/v_c)$ (top) and $p(v_x/v_c)$ (bottom) for the indirectly and directly heated directions, respectively. Data correspond to four different cases (two frequencies and two amplitudes).

the role of the walls for the detailed shape of the velocity distributions. An interesting challenge will be the comparison of simulations and experiments at higher packing fractions. Here we can expect more influence of particle-particle collisions relative to collisions with the walls, highly pronounced orientational inhomogeneity as well as clustering effects. Taking into account the recent advances in the analysis of experimental data in similar systems [145], one expects more possibilities to fine-tune the simulations and get more insight into the dynamics of granular gases. Further investigations can be envisioned in the direction of ensembles of particles of more elaborate shapes, as well as mixtures of different particles.

Chapter 6

Discussion

This dissertation examines dense and dilute particle flows, commonly found in many engineering applications and natural processes. These are complex processes involving several length and time scales, where practical experience indicates that the shape, roughness, and mechanical properties of the grains play a significant role. The previous chapters include four scientific publications, in which we have examined examples of particle flows. The research consisted of numerical and theoretical analysis, although we have also participated in some experiments. In particular, we focused on the development of Discrete Element Method (DEM) algorithms and novel coarse-graining techniques, accessing the dynamical response of these systems at multiple scales.

The work has been done in close collaboration with experimental partners of the Wigner Research Centre for Physics (Hungary), University of Twente (Netherlands), the Otto von Guericke University Magdeburg (Germany), the Academia Sinica (Taiwan) and the industrial partner DCS Computing. Furthermore, the numerical tools were calibrated using experimental outcomes of high-speed imaging and automatized mass flow controllers. Moreover, in some cases, the accuracy and performance of our implementations were also compared with the implementation of the industrial partner DCS Computing (LIGGGHTS®) [146]. These collaborations were crucial to analyze and validate the macroscopic response of the studied particulate systems.

Specifically, we have focused our efforts on silo flow, numerically studying 2D and 3D configurations and several particle types. These setups were thus systematically evaluated, using spherical and non-spherical particles, and varying the particle friction and stiffness.

In 2D silos, we studied numerically the flow of a mixture of particles with different stiffness and friction through a small orifice (see Chapter 3). Starting from a homogeneous system of non-frictional soft particles, we obtained that the clogging probability notably increases when adding a small percentage of high-friction, hard particles. The researchers of the Otto von Guericke University Magdeburg (Germany) and Wigner Research Centre for Physics (Hungary) studied the same experimentally. Combining both numerical and theoretical analysis, we notably improved the understanding of the clogging mechanisms based on the micromechanical details. However, it is worth mentioning that the used contact model did not quantitatively reproduce the characteristic time of the unstable clogs obtained experimentally with low-frictional hydrogels. The Hertz-Mindlin contact model is more suitable for reproducing the behavior of hard grains. In any case, both experiment and simulations were in good qualitative agreement, and allowed a comprehensive analysis of the system from complementary points of view. It is also interesting

to note that the clogging dynamics of mixtures of grains is a novel area of research, which is of great interest as of today (e.g. [147]).

In 3D silos, the results of our numerical analysis demonstrated that changing particle stiffness and friction has also a significant impact on gravity driven granular flow (see Chapter 2). The experimental approach was executed by researchers of the Wigner Research Centre for Physics (Hungary). We mainly found that decreasing the interparticle friction has a much stronger effect for soft grains than for hard grains. Remarkably, our coarse-graining analysis reveals considerably different pressure fields for hard and soft grains with low friction coefficient. For low-friction hard grains, Janssen screening is observed with increased vertical stress near the walls, while for low-friction soft grains this effect is much weaker. These findings are highly impactful, because they show that Beverloo's law can not be applied in the case of soft, low-frictional grains. Remarkably, analyzing the momentum balance in the region of the orifice, we proposed an analytical formulation that predicts the linear decrease of the flow rate with the decreasing filling height. The linear dependence of the flow rate on the pressure gradient suggests that the ensemble of low-friction, soft grains can be interpreted as a Newtonian fluid. It is also worth mentioning that incorporating a multiple-contact approach [94, 148] to the DEM simulations might improve the quantitative match between experimental and simulation data.

Besides in 3D silos, we participated in a numerical study, examining the effect that the transverse shear has on the flow rate when using spheres (data not shown in the thesis, but see our publication Ref. [123]). Remarkably, we have reproduced the main experimental findings obtained earlier by researchers of the Academia Sinica (Taiwan) (see Ref. [38]), and our approach notably shed light on the dynamics of the flow process under this specific boundary conditions. The latter scenario has served as a reference to study the case of elongated particles (see Chapter 4). Note that the experimental approach was also performed, in collaboration with researchers of the Academia Sinica (Taiwan) (data not shown in the thesis, but see our publication Ref. [41]). This case was even more interesting because the particle shape has induced significant changes in the system response. In particular, we found for elongated particles that the introduction of a slight transverse shear reduces the flow rate Q by up to 70% compared to a stationary bottom. The numerical analysis, presented in Chapter 4, contributed significantly to the understanding of such response. In the case of a stationary bottom, rods typically flow oriented parallel to the streamlines. However, even a weak rotation of the bottom wall causes an abrupt change in particle orientations. Namely, the transverse shear induces a more horizontal alignment of grains compared to the stationary case. The correlation between the flow rate and vertical orientation of particles at the orifice indicates that the rotational shear controls the flow through the alignment of grains. By carrying out a rigorous micro-mechanical analysis, our work suggests that in silo flow of elongated grains, the classical analysis of the *free fall arch* should not be taken for granted.

Additionally, we have performed numerical simulations of a heated granular gas of rod shaped particles (see Chapter 5). We reported numerical results that *quantitatively* agree with previous experimental findings and provide additional insight into the process, for instance describing the system behavior in the non-symmetrically heated direction, which was not accessed experimentally. However, the obtained velocity statistics require additional investigation from the point of view of individual rod collision dynamics, both with the walls and among rods. Another exciting challenge would be the comparison of simulations and experiments at higher packing fractions. In that case, pronounced orientation inhomogeneities and clustering effects might be observed. It is worth mentioning that the analysis of

this dilute scenario allowed us to execute a comparative analysis between the outcomes of the hybrid CPU-GPU code developed at the University of Navarra [42] and two other numerical approaches of LIGGGHTS® (data not shown in the thesis but see Ref. [146]). Note that we find excellent agreement, when comparing outcomes obtained using different HPC solutions. Finding that their computational performance was very similar when exploring very dilute systems, such as the granular gas of rods, despite the fact that GPU codes are not so efficient when handling small system sizes due to their specific architectural design. Said that, the thorough comparison of computational performance should be realized as a future work, accounting for different particle representations, CPU and GPU types and system details.

Conclusions and Outlook

Conclusions

In this thesis, we have developed accurate computational models to predict the macroscopic response of granular materials with different particle properties (shape, stiffness, and friction). Moreover, we have also focused our efforts on reducing the computational cost required for discrete element simulations by developing novel and highly efficient algorithms on modern computing platforms. As an ultimate goal, we improved the understanding of flows of spherical and non-spherical grains, based on the description of the flow micromechanical details. Specifically, we have examined three different silo flow processes, systematically varying the particles' properties and exploring a non-standard boundary condition. Moreover, a dilute heated gas of elongated particles has also been studied.

Our numerical investigation demonstrated that changing particle stiffness and friction strongly affects gravity-driven 3D silo flow. Remarkably, our DEM analysis reproduced the height-dependent discharge flow rate, obtained experimentally for soft low-frictional grains. Furthermore, the coarse-graining analysis of the DEM-data showed that the pressure drop at the orifice follows a linear dependence on the column height. It allowed us to propose simple theoretical arguments, connecting the macroscopic flow rate with the pressure gradient at the orifice. As a result, we have come up with a well-reasoned explanation for the height-dependent discharge flow rate, shown experimentally and numerically by soft low-frictional grains. Moreover, we consistently found that the height-dependent flow rate gradually approaches a constant flow rate regime when increasing the particle's friction. For hard grains, only very low frictions ($\mu \lesssim 0.05$) showed a non-constant flow rate. Furthermore, examining the stress field reveals that the vertical stress above the orifice are much lower for hard grains than for soft grains. Thus, while for hard grains a large part of the weight of the material is directed towards the silo corners, indicating Janssen screening is effective, a notably smaller effect is observed for soft grains.

In 2D silos, our simulations discharging a mixture of soft low-frictional grains (*hyd*) and hard frictional (*hf*) grains, qualitatively reproduced that the addition of very small amounts of *hf* to an ensemble of *hyd* impacts significantly the response of the system. Remarkably, the numerical results also revealed the relevant role played by the interspecies friction $\mu_{\text{hyd–hf}}$, in the clogging process. For instance, the difference in flow rates obtained for systems with different compositions were notably enhanced for larger $\mu_{\text{hyd–hf}}$. This fact also leads to more frequent clog events, and in these events, the occurrence of *hf* grains in the blocking arches is favored significantly. We argue that the much higher importance of $\mu_{\text{hf–hyd}}$ in comparison to $\mu_{\text{hf–hf}}$ is due to the fact that the probability of direct contacts of two hard grains is substantially smaller than that of a *hf* and a *hyd* neighbor, owing to the low concentration of hard frictional grains. The simulations also complemented the experiments, studying clog duration at

notably shorter time scales. Altogether, a higher friction between the two kinds of particles also makes clogging more frequent, and increases the probability of finding hard grains in the arch.

Exploring the role of the particle shape, the DEM simulation of discharging elongated particles from a 3D silo with a rotating bottom indicated a flow rate reduction by up to 70%, in comparison to the stationary bottom case. These results agree well with our experimental findings [41], but are very surprising, mainly when set side by side with the case of spheres, where this reduction was only around 5% [38, 123]. Our numerical tool also allowed for the exploring of the dependence of flow rate Q on the orifice size D. In the limit of large orifices, the classical power-law correlation $Q \sim D^{5/2}$ was reproduced. For small apertures, however, we obtained a power-law relation but with a notably larger exponent. By employing a coarse-graining methodology, we computed the most relevant macroscopic fields, detecting a transition from a funnel to a mass flow pattern induced by the external shear. The averaged fields in the orifice region revealed that the initial decrease in Q is mainly attributed to the velocity changes. Besides this, the increase of the packing fraction near the orifice explains the increase in Q for larger rotation frequencies. Furthermore, the flow rate correlates with the particle orientation in the vertical direction, and the packing fraction with the order of grains in the region of the orifice. Interestingly, we also found that the vertical profiles of mean acceleration at the center of the silo are notably affected by the rotation of the bottom wall. In flows of elongated rods, it is observed that the region where the acceleration is not negligible (so-called free fall arch) shrinks significantly due to the perturbation induced by the moving wall.

When analyzing a dilute granular gas of elongated particles in microgravity conditions, our numerical approach reproduces the experimental findings and provides additional insight into this process. We reproduce that the maximum velocity of the moving walls v_c is the relevant characteristic scale. It denotes that the energy of the system in steady conditions is controlled by the walls. These outcomes corroborate the guess made in Ref. [43], that the kinetic energy in the system scales with $v_c^2 \propto A^2 f^2$, and not the peak acceleration of the walls. This finding is logical and would seem trivial until it is pointed out that the energy of a single rod excited by a vertically vibrated horizontal plane in gravity scales as $\propto A^{1.5} f$ instead [144]. The discrepancy of scaling might be due to the lack of gravity or due to the collective heating dynamics.

Outlook

The numerical investigation of the discharge of soft, low-friction particles showed that there are lots of opportunities for potential future research in the area. For example, the frequently used $\mu(I)$ rheology doesn't consider the stiffness of the grains, thus wouldn't be capable of predicting flows of hydrogels or other soft particles. From the point of view of DEM simulations, it is clear that contact models assuming independent contacts are not sufficient to precisely model soft grains. Thus, the implementation and calibration of a multi-contact model is necessary [94, 148].

Concerning the discharge of rods from a silo, additional research is needed to identify an effective particle size depending on the particle orientation. Also, a continuum model accounting for the particle elongation could be developed, since today's rheological models only consider spherical or close-to-spherical grains. One of the practical implications of the study of the rotating bottom silo is that this form of energy input breaks the arches which form a clog, thus it can appear on the palette of industrial

tools when solving clogging issues. On the other hand, counterintuitively, the flow is not enhanced but instead slowed down in the continuous flow regime when the rotational shear is applied. This could be undesirable in the industry.

The investigation of the effect of particle elongation in a normal, flat bottom silo is also in progress. The systematic study of rods with different aspect ratios (up to 6) reveals that the discharge rates are not always constant, but rather show a time evolution. This phenomenon depends on the orifice size, particle elongation and even on the system size. The full understanding of this observation needs more investigation in this line of research.

Regarding the granular gases, the understanding of the heating dynamics is crucial because the simplest way to introduce energy into a dilute system in experiments is through the vibration of the walls. In this line of investigation, one option could be the study of the spatial distribution of the velocity and energy fields.

It is worth mentioning that we are currently examining flows of irregular grains in 3D silos and hoppers. This work is in line with experiments carried out in parallel by researchers at the University of Twente (Netherlands). For the sake of efficiency, we have written new CUDA-kernels, which are able to handle the contact between particles with superquadrical shape [149]. The experimental results (flow morphology and particle flow rates) serve as a guiding line to validate and calibrate the DEM implementation, in particular using superquadrics. As a final goal, we aim to address the dynamical behavior of this system, examining the particle-particle correlations and their interrelation with the global macroscopic response of the system.

Through the utilization of GPUs and the development of our custom code, we have gained a lot of practical experience regarding computer science and numerical methods. We have started from small optimization steps in GPU programming, through the implementation of uncommon boundary conditions, up until the implementation and fine-tuning of a superquadrics contact detection algorithm on GPUs. One example of these optimizations is the rearrangement of particle neighbor information into a continuous contact pair list which offered a better fit for the GPU architecture and a speedup of about 70-80% in most of our simulations. For the efficient calculation of superquadric contacts on GPUs, it was crucial to improve the accuracy and to optimize the convergence of the iterative Newton-Raphson method for 32-bit floating point variables instead of employing double-precision floating point variables. Taking into account the fact on many inexpensive GPUs there are up to 64 times more 32-bit floating-point units compared to 64-bit ones, the use of single-precision float variables is greatly advantageous. This way the superquadrical particle representation opens windows to the simulation of larger (in the order of 100000 particles) system sizes with these kinds of particles which was not possible earlier. All of the above could be the base of a future research in the field of computational science.

Bibliography

[1] P. A. Cundall, O. D. Strack. *A discrete numerical model for granular assemblies*. geotechnique **29 (1)**, (1979), pp. 47–65.

[2] A. Di Renzo, F. P. Di Maio. *Comparison of contact-force models for the simulation of collisions in dem-based granular flow codes*. Chemical engineering science **59 (3)**, (2004), pp. 525–541.

[3] E. Hairer, C. Lubich, G. Wanner. *Geometric numerical integration illustrated by the störmer–verlet method*. Acta numerica **12**, (2003), pp. 399–450.

[4] D. J. Evans, S. Murad. *Singularity free algorithm for molecular dynamics simulation of rigid polyatomics*. Molecular physics **34 (2)**, (1977), pp. 327–331.

[5] D. J. Evans. *On the representatation of orientation space*. Molecular physics **34 (2)**, (1977), pp. 317–325.

[6] D. Antypov, J. Elliott. *On an analytical solution for the damped hertzian spring*. EPL (Europhysics Letters) **94 (5)**, (2011), p. 50004.

[7] Y. J. Huang, O. J. Nydal, B. Yao. *Time step criterions for nonlinear dense packed granular materials in time-driven method simulations*. Powder technology **253**, (2014), pp. 80–88.

[8] M. Babic. *Average balance equations for granular materials*. International journal of engineering science **35 (5)**, (1997), pp. 523–548.

[9] I. Goldhirsch. *Stress, stress asymmetry and couple stress: from discrete particles to continuous fields*. Granular Matter **12**, (2010), pp. 239–252.

[10] J. Zhang, R. P. Behringer, I. Goldhirsch. *Coarse-graining of a physical granular system*. Progress of Theoretical Physics Supplement **184**, (2010), pp. 16–30.

[11] GDR MiDi. *On dense granular flows*. The European Physical Journal E **14**, (2004), pp. 341–365.

[12] P. Jop, Y. Forterre, O. Pouliquen. *A constitutive law for dense granular flows*. Nature **441 (7094)**, (2006), pp. 727–730.

[13] L. Staron, P.-Y. Lagrée, S. Popinet. *The granular silo as a continuum plastic flow: The hour-glass vs the clepsydra*. Physics of Fluids **24 (10)**, (2012), p. 103301.

[14] L. Staron, P.-Y. Lagrée, S. Popinet. *Continuum simulation of the discharge of the granular silo*. The European Physical Journal E **37 (1)**, (2014), pp. 1–12.

[15] K. Kamrin. *Nonlinear elasto-plastic model for dense granular flow*. International Journal of Plasticity **26 (2)**, (2010), pp. 167–188.

[16] K. Kamrin, G. Koval. *Nonlocal constitutive relation for steady granular flow*. Physical review letters **108 (17)**, (2012), p. 178301.

[17] C. Kloss, C. Goniva, A. Hager, S. Amberger, S. Pirker. *Models, algorithms and validation for opensource dem and cfd–dem*. Progress in Computational Fluid Dynamics, an International Journal **12 (2-3)**, (2012), pp. 140–152.

[18] H. Janssen. *Versuche uber getreidedruck in silozellen*. Z. ver. deut. Ing. **39**, (1895), p. 1045.

[19] Y. Bertho, F. Giorgiutti-Dauphiné, J.-P. Hulin. *Dynamical janssen effect on granular packing with moving walls*. Physical review letters **90 (14)**, (2003), p. 144301.

[20] W. A. Beverloo, H. A. Leniger, J. Van de Velde. *The flow of granular solids through orifices*. Chemical engineering science **15 (3-4)**, (1961), pp. 260–269.

[21] A. Janda, I. Zuriguel, D. Maza. *Flow rate of particles through apertures obtained from self-similar density and velocity profiles*. Physical review letters **108 (24)**, (2012), p. 248001.

[22] P. Artega, U. Tüzün. *Flow of binary mixtures of equal-density granules in hoppers—size segregation, flowing density and discharge rates*. Chemical engineering science **45 (1)**, (1990), pp. 205–223.

[23] D. Bertuola, S. Volpato, P. Canu, A. C. Santomaso. *Prediction of segregation in funnel and mass flow discharge*. Chemical Engineering Science **150**, (2016), pp. 16–25.

[24] K. To, P.-Y. Lai, H. Pak. *Jamming of granular flow in a two-dimensional hopper*. Physical review letters **86 (1)**, (2001), p. 71.

[25] I. Zuriguel, A. Garcimartín, D. Maza, L. A. Pugnaloni, J. Pastor. *Jamming during the discharge of granular matter from a silo*. Physical Review E **71 (5)**, (2005), p. 051303.

[26] M. L. Hunt, R. C. Weathers, A. T. Lee, C. E. Brennen, C. R. Wassgren. *Effects of horizontal vibration on hopper flows of granular materials*. Physics of Fluids **11 (1)**, (1999), pp. 68–75.

[27] C. R. Wassgren, M. L. Hunt, P. J. Freese, J. Palamara, C. E. Brennen. *Effects of vertical vibration on hopper flows of granular material*. Physics of Fluids **14 (10)**, (2002), pp. 3439–3448.

[28] A. Janda, D. Maza, A. Garcimartín, E. Kolb, J. Lanuza, E. Clément. *Unjamming a granular hopper by vibration*. EPL (Europhysics Letters) **87 (2)**, (2009), p. 24002.

[29] C. Mankoc, A. Garcimartín, I. Zuriguel, D. Maza, L. A. Pugnaloni. *Role of vibrations in the jamming and unjamming of grains discharging from a silo*. Phys. Rev. E **80 (1)**, (2009), p. 011309.

[30] C. Merrigan, S. K. Birwa, S. Tewari, B. Chakraborty. *Ergodicity breaking dynamics of arch collapse*. Phys. Rev. E **97 (4)**, (2018), p. 040901.

[31] B. V. Guerrero, B. Chakraborty, I. Zuriguel, A. Garcimartín. *Nonergodicity in silo unclogging: Broken and unbroken arches*. Phys. Rev. E **100 (3)**, (2019), p. 32901.

[32] W. Chen, M. Hou, K. Lu, Z. Jiang, L. Lam. *Granular flows through vertical pipes controlled by an electric field*. Phys. Rev. E **64 (6)**, (2001), p. 061305.

[33] R. N. Dave, C.-Y. Wu, B. Chaudhuri, S. Watano. *Magnetically mediated flow enhancement for controlled powder discharge of cohesive powders*. Powder Technology **112 (1-2)**, (2000), pp. 111–125.

[34] D. Hernández-Enríquez, G. Lumay, F. Pacheco-Vázquez. *Discharge of repulsive grains from a silo: Experiments and simulations*. In *EPJ Web of Conferences. Powders and Grains 2017*, vol. 140, pp. 8–11 (2017).

[35] L. Thorens, M. Viallet, K. J. Måløy, M. Bourgoin, S. Santucci. *Discharge of a 2D magnetic silo*. In M. Aguirre, S. Luding, L. Pugnaloni, R. Soto, eds., *EPJ Web of Conferences. Powders and Grains 2021*, vol. 249, p. 03017 (2021).

[36] E. I. Corwin. *Granular flow in a rapidly rotated system with fixed walls*. Phys. Rev. E **77 (3)**, (2008), p. 031308.

[37] J. E. Hilton, P. W. Cleary. *The effect of rotational shear on granular discharge rates*. Physics of Fluids **22 (7)**, (2010), p. 071701.

[38] K. To, Y. Yen, Y.-K. Mo, J.-R. Huang. *Granular flow from silos with rotating orifice*. Phys. Rev. E **100 (1)**, (2019), p. 012906.

[39] T. Pongó, V. Stiga, J. Török, S. Lévay, B. Szabó, R. Stannarius, R. C. Hidalgo, T. Börzsönyi. *Flow in an hourglass: particle friction and stiffness matter*. New Journal of Physics **23 (2)**, (2021), p. 023001.

[40] J. Wang, B. Fan, T. Pongó, K. Harth, T. Trittel, R. Stannarius, M. Illig, T. Börzsönyi, R. C. Hidalgo. *Silo discharge of mixtures of soft and rigid grains*. Soft Matter **17 (16)**, (2021), pp. 4282–4295.

[41] K. To, Y.-K. Mo, T. Pongó, T. Börzsönyi. *Discharge of elongated grains from silo with rotating bottom*. Phys. Rev. E **103 (6)**, (2021), p. 062905.

[42] T. Pongó, D. Puzyrev, K. Harth, R. Stannarius, R. C. Hidalgo. *Continuously heated granular gas of elongated particles*. In *EPJ Web of Conferences*, vol. 249, p. 04003. EDP Sciences (2021).

[43] K. Harth, U. Kornek, T. Trittel, U. Strachauer, S. Höme, K. Will, R. Stannarius. *Granular gases of rod-shaped grains in microgravity*. Physical review letters **110 (14)**, (2013), p. 144102.

[44] R. Nedderman, U. Tüzün, S. Savage, G. Houlsby. *Flow of granular materials-i. discharge rates from hoppers*. Chem. Eng. Sci.;(United Kingdom) **37 (11)**.

[45] H. M. Jaeger, S. R. Nagel. *Physics of the granular state*. Science **255 (5051)**, (1992), pp. 1523–1531.

[46] H. M. Jaeger, S. R. Nagel, R. P. Behringer. *Granular solids, liquids, and gases*. Reviews of modern physics **68 (4)**, (1996), p. 1259.

[47] H. M. Jaeger, S. R. Nagel, R. P. Behringer. *The physics of granular materials*. Physics today **49 (4)**, (1996), pp. 32–39.

[48] J. Kakalios. *Resource letter gp-1: Granular physics or nonlinear dynamics in a sandbox*. American Journal of Physics **73 (1)**, (2005), pp. 8–22.

[49] B. P. Tighe, M. Sperl. *Pressure and motion of dry sand: translation of hagen's paper from 1852*. Granular Matter **9 (3)**, (2007), pp. 141–144.

[50] C. S. Campbell. *Granular material flows–an overview*. Powder Technology **162 (3)**, (2006), pp. 208–229.

[51] C. Mankoc, A. Janda, R. Arevalo, J. Pastor, I. Zuriguel, A. Garcimartín, D. Maza. *The flow rate of granular materials through an orifice*. Granular Matter **9 (6)**, (2007), pp. 407–414.

[52] H. Pacheco-Martinez, H. J. Van Gerner, J. Ruiz-Suárez. *Storage and discharge of a granular fluid*. Physical Review E **77 (2)**, (2008), p. 021303.

[53] H. Ahn, Z. Başaranoğlu, M. Yılmaz, A. Buğutekin, M. Z. Gül. *Experimental investigation of granular flow through an orifice*. Powder Technology **186 (1)**, (2008), pp. 65–71.

[54] J. Baosheng, T. He, W. Zhong. *Flow behaviors of non-spherical granules in rectangular hopper*. Chinese Journal of Chemical Engineering **18 (6)**, (2010), pp. 931–939.

[55] R. Balevičius, I. Sielamowicz, Z. Mroz, R. Kačianauskas. *Investigation of wall stress and outflow rate in a flat-bottomed bin: A comparison of the dem model results with the experimental measurements*. Powder technology **214 (3)**, (2011), pp. 322–336.

[56] I. Oldal, I. Keppler, B. Csizmadia, L. Fenyvesi. *Outflow properties of silos: The effect of arching*. Advanced Powder Technology **23 (3)**, (2012), pp. 290–297.

[57] C. Perge, M. A. Aguirre, P. A. Gago, L. A. Pugnaloni, D. Le Tourneau, J.-C. Géminard. *Evolution of pressure profiles during the discharge of a silo*. Physical Review E **85 (2)**, (2012), p. 021303.

[58] J. Koivisto, D. J. Durian. *The sands of time run faster near the end*. Nature communications **8 (1)**, (2017), pp. 1–6.

[59] J. Koivisto, M. Korhonen, M. Alava, C. P. Ortiz, D. J. Durian, A. Puisto. *Friction controls even submerged granular flows*. Soft Matter **13 (41)**, (2017), pp. 7657–7664.

[60] S. Dorbolo, L. Maquet, M. Brandenbourger, F. Ludewig, G. Lumay, H. Caps, N. Vandewalle, S. Rondia, M. Mélard, J. van Loon, et al. *Influence of the gravity on the discharge of a silo*. Granular Matter **15 (3)**, (2013), pp. 263–273.

[61] M. Sperl. *Experiments on corn pressure in silo cells–translation and comment of janssen's paper from 1895*. Granular Matter **8 (2)**, (2006), pp. 59–65.

[62] F. Huber-Burnand. *Sur l'écoulement et la pression du sable*. Ann. de Chimie et de Physique **50**, (1829), pp. 159–173.

[63] G. Hagen. *Bericht über die zur bekanntmachung geeigneten verhandlungen der königlich preussischen akademie der wissenschaften zu berlin* (1852).

[64] I. Roberts. *I. determination of the vertical and lateral pressures of granular substances*. Proceedings of the Royal Society of London **36 (228-231)**, (1883), pp. 225–240.

[65] L. Vanel, E. Clément. *Pressure screening and fluctuations at the bottom of a granular column*. The European Physical Journal B-Condensed Matter and Complex Systems **11 (3)**, (1999), pp. 525–533.

[66] L. Vanel, P. Claudin, J.-P. Bouchaud, M. Cates, E. Clément, J. Wittmer. *Stresses in silos: comparison between theoretical models and new experiments*. Physical review letters **84 (7)**, (2000), p. 1439.

[67] J. Hilton, P. Cleary. *Granular flow during hopper discharge*. Physical Review E **84 (1)**, (2011), p. 011307.

[68] R. Brown. *Profile of flow of granules through apertures*. Trans. Inst Chem. Engrs. **38**, (1960), pp. 243–256.

[69] F. Franklin, L. Johanson. *Flow of granular material through a circular orifice*. Chemical Engineering Science **4 (3)**, (1955), pp. 119–129.

[70] J. P. Peralta, M. A. Aguirre, J.-C. Géminard, L. A. Pugnaloni. *Apparent mass during silo discharge: Nonlinear effects related to filling protocols*. Powder Technology **311**, (2017), pp. 265–272.

[71] R. M. Nedderman, et al. *Statics and kinematics of granular materials*, vol. 352. Cambridge University Press Cambridge (1992).

[72] S. Savage. *Gravity flow of a cohesionless bulk solid in a converging conical channel*. International Journal of Mechanical Sciences **9 (9)**, (1967), pp. 651–659.

[73] J. Davidson. *The hourglass theory of hopper flow*. Trans. Instn Chem. Engrs **51**, (1973), pp. 29–35.

[74] S. M. Rubio-Largo, A. Janda, D. Maza, I. Zuriguel, R. Hidalgo. *Disentangling the free-fall arch paradox in silo discharge*. Physical review letters **114 (23)**, (2015), p. 238002.

[75] J. R. Darias, M. A. Madrid, L. A. Pugnaloni. *Differential equation for the flow rate of discharging silos based on energy balance*. Physical Review E **101 (5)**, (2020), p. 052905.

[76] T. Wilson, C. Pfeifer, N. Meysingier, D. J. Durian. *Granular discharge rate for submerged hoppers*. Papers in physics **6 (2)**, (2014), pp. 0–0.

[77] M. A. Madrid, J. Darias, L. A. Pugnaloni. *Forced flow of granular media: Breakdown of the beverloo scaling*. EPL (Europhysics Letters) **123 (1)**, (2018), p. 14004.

[78] D. Hirshfeld, Y. Radzyner, D. Rapaport. *Molecular dynamics studies of granular flow through an aperture*. Physical Review E **56 (4)**, (1997), p. 4404.

[79] D. Hirshfeld, D. Rapaport. *Granular flow from a silo: discrete-particle simulations in three dimensions*. The European Physical Journal E **4 (2)**, (2001), pp. 193–199.

[80] J. Jofriet, S. Negi, Z. Lu. *A numerical model for flow of granular materials in silos. part 3: Parametric study*. Journal of agricultural engineering research **68 (3)**, (1997), pp. 237–246.

[81] R. Balevičius, R. Kačianauskas, Z. Mroz, I. Sielamowicz. *Microscopic and macroscopic analysis of granular material behaviour in 3d flat-bottomed hopper by the discrete element method*. Archives of mechanics **59 (3)**, (2007), pp. 231–257.

[82] P. A. Langston, U. Tüzün, D. M. Heyes. *Discrete element simulation of granular flow in 2d and 3d hoppers: dependence of discharge rate and wall stress on particle interactions*. Chemical Engineering Science **50 (6)**, (1995), pp. 967–987.

[83] A. Ashour, T. Trittel, T. Börzsönyi, R. Stannarius. *Silo outflow of soft frictionless spheres*. Physical Review Fluids **2 (12)**, (2017), p. 123302.

[84] X. Hong, M. Kohne, M. Morrell, H. Wang, E. R. Weeks. *Clogging of soft particles in two-dimensional hoppers*. Physical Review E **96 (6)**, (2017), p. 062605.

[85] K. Harth, J. Wang, T. Börzsönyi, R. Stannarius. *Intermittent flow and transient congestions of soft spheres passing narrow orifices*. Soft Matter **16 (34)**, (2020), pp. 8013–8023.

[86] R. Stannarius, D. Sancho Martinez, T. Finger, E. Somfai, T. Börzsönyi. *Packing and flow profiles of soft grains in 3d silos reconstructed with x-ray computed tomography*. Granular Matter **21 (3)**, (2019), pp. 1–10.

[87] R. Stannarius, D. S. Martinez, T. Börzsönyi, M. Bieberle, F. Barthel, U. Hampel. *High-speed x-ray tomography of silo discharge*. New Journal of Physics **21 (11)**, (2019), p. 113054.

[88] J. A. Dijksman, N. Brodu, R. P. Behringer. *Refractive index matched scanning and detection of soft particles*. Review of Scientific Instruments **88 (5)**, (2017), p. 051807.

[89] N. Brodu, J. A. Dijksman, R. P. Behringer. *Spanning the scales of granular materials through microscopic force imaging*. Nature communications **6 (1)**, (2015), pp. 1–6.

[90] B. N. Persson. *Sliding friction: physical principles and applications*. Springer Berlin, Heidelberg (1998).

[91] T. Weinhart, R. Hartkamp, A. R. Thornton, S. Luding. *Coarse-grained local and objective continuum description of three-dimensional granular flows down an inclined surface*. Physics of Fluids **25 (7)**, (2013), p. 070605.

[92] R. Artoni, P. Richard. *Average balance equations, scale dependence, and energy cascade for granular materials*. Physical Review E **91 (3)**, (2015), p. 032202.

[93] R. Artoni, P. Richard. *Coarse graining for granular materials: micro-polar balances*. Acta Mechanica **230 (9)**, (2019), pp. 3055–3069.

[94] N. Brodu, J. A. Dijksman, R. P. Behringer. *Multiple-contact discrete-element model for simulating dense granular media*. Physical Review E **91 (3)**, (2015), p. 032201.

[95] M. A. Aguirre, J. G. Grande, A. Calvo, L. A. Pugnaloni, J.-C. Géminard. *Pressure independence of granular flow through an aperture*. Phys. Rev. Lett. **104**, (2010), p. 238002.

[96] H. G. Sheldon, D. J. Durian. *Granular discharge and clogging for tilted hoppers*. Granular Matter **12 (6)**, (2010), pp. 579–585.

[97] K. To. *Jamming transition in two-dimensional hoppers and silos*. Phys. Rev. E **71**, (2005), p. 060301.

[98] C. C. Thomas, D. J. Durian. *Fraction of clogging configurations sampled by granular hopper flow*. Phys. Rev. Lett. **114**, (2015), p. 178001.

[99] J. Tang, R. Behringer. *How granular materials jam in a hopper*. Chaos **21**, (2011), p. 041107.

[100] I. Zuriguel, D. R. Parisi, R. C. Hidalgo, C. Lozano, A. Janda, P. A. Gago, J. P. Peralta, L. M. Ferrer, L. A. Pugnaloni, E. Clément, D. Maza, I. Pagonabarraga, A. Garcimartín. *Clogging transition of many-particle systems flowing through bottlenecks*. Scientific Reports **4**, (2014), p. 7324.

[101] R. C. Hidalgo, C. Lozano, I. Zuriguel, A. Garcimartín. *Force analysis of clogging arches in a silo*. Granular Matter **15**, (2013), pp. 841–848.

[102] F. Vivanco, S. Rica, F. Melo. *Dynamical arching in a two dimensional granular flow*. Granular Matter **14 (5)**, (2012), pp. 563–576.

[103] B. V. Guerrero, C. Lozano, I. Zuriguel, A. Garcimartín. *Slow relaxation dynamics of clogs in a vibrated granular silo*. Phys. Rev. E **97**, (2018), p. 042904.

[104] A. Marin, H. Lhuissier, M. Rossi, C. J. Kähler. *Clogging in constricted suspension flows*. Phys. Rev. E **97**, (2018), p. 021102(R).

[105] R. C. Hidalgo, A. Goni-Arana, A. Hernández-Puerta, I. Pagonabarraga. *Flow of colloidal suspensions through small orifices*. Phys. Rev. E **97**, (2018), p. 012611.

[106] M. Souzy, I. Zuriguel, A. Marin. *Clogging transitions in constricted particle suspension flows*. Phys. Rev. E **101**, (2020), p. 060901(R).

[107] I. Zuriguel. *Clogging of granular materials in bottlenecks*. Papers in Physics **6**, (2014), p. 060014.

[108] T. Pöschel, T. Schwager. *Computational Granular Dynamics*. Springer-Verlag Berlin Heidelberg New York (2005).

[109] C. C. Thomas, D. J. Durian. *Geometry dependence of the clogging transition in tilted hoppers*. Phys. Rev. E **87**, (2013), p. 052201.

[110] B. Andreotti, Y. Forterre, O. Pouliquen. *Granular Media: Between Fluid and Solid*. Cambridge University Press (2013).

[111] A. Pascot, N. Gaudel, S. Antonyuk, J. Bianchin, S. Kiesgen De Richter. *Influence of mechanical vibrations on quasi-2D silo discharge of spherical particles*. Chemical Engineering Science **224**, (2020), p. 115749.

[112] T. Börzsönyi, B. Szabó, G. Törös, S. Wegner, J. Török, E. Somfai, T. Bien, R. Stannarius. *Orientational order and alignment of elongated particles induced by shear*. Phys. Rev. Lett. **108 (22)**, (2012), p. 228302.

[113] T. Börzsönyi, B. Szabó, S. Wegner, K. Harth, J. Török, E. Somfai, T. Bien, R. Stannarius. *Shear-induced alignment and dynamics of elongated granular particles*. Phys. Rev. E **86**, (2012), p. 051304.

[114] S. M. Rubio-Largo, F. Alonso-Marroquín, T. Weinhart, S. Luding, R. C. Hidalgo. *Homogeneous cooling state of frictionless rod particles*. Physica A **443**, (2016), pp. 477 – 485.

[115] F. Alonso-Marroquín. *Spheropolygons: A new method to simulate conservative and dissipative interactions between 2d complex-shaped rigid bodies*. Europhys. Lett. **83**, (2008), p. 14001.

[116] F. Alonso-Marroquín, Y. Wang. *An efficient algorithm for granular dynamics simulations with complex-shaped objects*. Granular Matter **11**, (2009), pp. 317–329.

[117] C. Vega, S. Lago. *A fast algorithm to evaluate the shortest distance between rods*. Computers & chemistry **18 (1)**, (1994), pp. 55–59.

[118] T. Weinhart, A. R. Thornton, S. Luding, O. Bokhove. *Closure relations for shallow granular flows from particle simulations*. Granul. Matter **14 (4)**, (2012), pp. 531–552.

[119] Y. Wang, S. Abe, S. Latham, P. Mora. *Implementation of particle-scale rotation in the 3-d lattice solid model*. In X.-c. Yin, P. Mora, A. Donnellan, M. Matsu'ura, eds., *Computational Earthquake Physics: Simulations, Analysis and Infrastructure, Part I*, Pageoph Topical Volumes, pp. 1769–1785. Birkhäuser Basel (2006).

[120] L. E. Silbert, D. Ertaş, G. S. Grest, T. C. Halsey, D. Levine, S. J. Plimpton. *Granular flow down an inclined plane: Bagnold scaling and rheology*. Phys. Rev. E **64 (5)**, (2001), p. 051302.

[121] T. Schwager, T. Pöschel. *Coefficient of restitution and linear–dashpot model revisited*. Granular Matter **9 (6)**, (2007), pp. 465–469.

[122] P. Richard, M. Nicodemi, R. Delannay, P. Ribière, D. Bideau. *Slow relaxation and compaction of granular systems*. Nature Materials **4**, (2005), pp. 121–128.

[123] D. Hernández-Delfin, T. Pongó, K. To, T. Börzsönyi, R. Hidalgo. *Particle flow rate in silos under rotational shear*. Phys. Rev. E **102 (4)**, (2020), p. 042902.

[124] T. Börzsönyi, E. Somfai, B. Szabó, S. Wegner, P. Mier, G. Rose, R. Stannarius. *Packing, alignment and flow of shape-anisotropic grains in a 3d silo experiment*. New J. Phys. **18 (9)**, (2016), p. 093017.

[125] S. Wegner, T. Börzsönyi, T. Bien, G. Rose, R. Stannarius. *Alignment and dynamics of elongated cylinders under shear*. Soft Matter **8 (42)**, (2012), pp. 10950–10958.

[126] Y. N. Harari. *Sapiens: A brief history of humankind*. Random House (2014).

[127] T. Pöschel, S. Luding. *Granular Gases*. Springer-Verlag, Berlin Heidelberg, Germany (2001).

[128] N. V. Brilliantov, T. Pöschel. *Kinetic Theory of Granular Gases*. Oxford University Press, Oxford, UK (2004).

[129] P. Haff. *Grain flow as a fluid-mechanical phenomenon*. J. Fluid Mech. **134**, (1983), pp. 401–430.

[130] C. C. Maaß, N. Isert, G. Maret, C. Aegerter. *Experimental investigation of the freely cooling granular gas*. Phys. Rev. Lett. **100**, (2008), p. 248001.

[131] K. Harth, T. Trittel, S. Wegner, R. Stannarius. *Free cooling of a granular gas of rodlike particles in microgravity*. Phys. Rev. Lett. **120 (21)**, (2018), p. 214301.

[132] K. Harth, T. Trittel, S. Wegner, R. Stannarius. *Cooling of 3d granular gases in microgravity experiments*. EPJ Web of Conferences **140**, (2017), p. 04008.

[133] P. Yu, M. Schröter, M. Sperl. *Velocity distribution of a homogeneously cooling granular gas*. Phys. Rev. Lett. **124**, (2020), p. 208007.

[134] T. Schwager, T. Pöschel. *Coefficient of normal restitution of viscous particles and cooling rate of granular gases*. Phys. Rev. E **57**, (1998), p. 650.

[135] T. Aspelmeier, G. Giese, A. Zippelius. *Cooling dynamics of a dilute gas of inelastic rods: A many particle simulation*. Phys. Rev. E **57**, (1998), p. 857.

[136] K. Harth, T. Trittel, K. May, S. Wegner, R. Stannarius. *Three-dimensional (3d) experimental realization and observation of a granular gas in microgravity*. Adv. Space Res. **55 (7)**, (2015), pp. 1901 – 1912.

[137] K. Harth, T. Trittel, U. Kornek, S. Höme, K. Will, U. Strachauer, R. Stannarius. *Microgravity experiments on a granular gas of elongated grains*. AIP Conf. Proc. **1542**, (2013), p. 807.

[138] S. Aumaitre, et al. *An instrument for studying granular media in low-gravity environment*. Rev. Sci. Instr. **89**, (2018), p. 075103.

[139] F. Villemot, J. Talbot. *Homogeneous cooling of hard ellipsoids*. Granular Matter **14 (2)**, (2012), pp. 91–97.

[140] S. M. Rubio-Largo, P. G. Lind, D. Maza, R. C. Hidalgo. *Granular gas of ellipsoids: analytical collision detection implemented on gpus*. Comput. Part. Mech. **2 (2)**, (2015), pp. 127–138.

[141] K. E. Buettner, Y. Guo, J. S. Curtis. *Development of a collisional dissipation rate model for frictional cylinders*. Powder Technol. **365**, (2020), pp. 83 – 91.

[142] D. Puzyrev, R. C. Hidalgo, D. Fischer, K. Harth, T. Trittel, R. Stannarius. *Cluster dynamics in dense granular gases of rod-like particles*. In *EPJ Web of Conferences*, vol. 249, p. 04004. EDP Sciences (2021).

[143] Y. Wang, S. Abe, S. Latham, P. Mora. *Implementation of particle-scale rotation in the 3-d lattice solid model*. Pure Appl. Geophys **163**, (2006), pp. 1769–1785.

[144] T. Trittel, K. Harth, R. Stannarius. *Mechanical excitation of rodlike particles by a vibrating plate*. Phys. Rev. E **95**, (2017), p. 062904.

[145] D. Puzyrev, K. Harth, T. Trittel, R. Stannarius. *Machine learning for 3d particle tracking in granular gases*. Microgravity Sci. Technol. **32**, (2020), p. 897.

[146] T. Pongó, B. Fan, Z. Ristic, M. Mascara, A. Mayrhofer, C. Kloss, T. Börzsönyi, R. Cruz Hidalgo. *Custom code calibration + comparison with LIGGGHTS®* (2021). https://www.doi.org/10.3030/812638 Results/Reports section.

[147] S. Alborzi, B. G. Clark, S. M. Hashmi. *Soft particles facilitate flow of rigid particles in a 2d hopper*. Soft Matter **18 (21)**, (2022), pp. 4127–4135.

[148] N. Ghods, P. Poorsolhjouy, M. Gonzalez, S. Radl. *Discrete element modeling of strongly deformed particles in dense shear flows*. Powder Technology **401**, (2022), p. 117288.

[149] A. Podlozhnyuk, S. Pirker, C. Kloss. *Efficient implementation of superquadric particles in discrete element method within an open-source framework*. Computational Particle Mechanics **4 (1)**, (2017), pp. 101–118.

Summary

Granular flows are frequently observed in nature and appear in many industrial processes as well. In this numerical work the focus is mainly directed at the understanding of how the change of different grain properties, such as shape, friction and stiffness, influences the flow out of a silo. However, the heating dynamics of a granular gas of rods is also analyzed. In all these scenarios, the simulations are paired with experiments to calibrate and validate the results.

The numerical analysis indicated that the discharge of soft, low-friction grains from a container exhibits a height-dependent flow rate, which is not usual for granular media. The systematic study mapped the parameter space of particle friction and stiffness, exploring the system's macroscopic response in detail. Moreover, the examination of the coarse-graining fields helped us to explain when and why the flow rate depends on the column height. The answers include the material response to pressure gradients, but also the way stress is transmitted in the system. The outcomes allowed us to propose simple theoretical arguments, connecting the macroscopic flow rate with the pressure gradient at the orifice. As a result, we have come up with a well-reasoned explanation for the height-dependent discharge flow rate, shown experimentally and numerically by soft low-frictional grains.

Our numerical investigation of a 2D silo flow of mixtures of soft and hard grains reproduced the high impact that even 5% of hard frictional grains have on the flow of an ensemble of low-friction, soft particles. Numerical results signaled the importance of the friction between the two types of grains. When the frictional hard grains are added to the soft grains, the flow gets slower, clogging becomes more frequent, and the force measured on the bottom plate decreases. Moreover, we obtained that these effects are enhanced when the interspecies friction is increased.

The introduction of a rotational shear through the rotation of the flat silo bottom leads to a surprising effect on the discharge of rods: the flow rate is reduced significantly, by up to 70%. Our simulations and the application of the coarse-graining methods reveal the underlying reasons for this observation. The exit velocity of particles is the main contributing factor to this drop, which is in correlation with the vertical orientation of the grains. Our numerical tool allowed the exploration of the dependence of flow rate Q on the orifice size D. In the limit of large orifices, the classical power-law correlation $Q \sim D^{5/2}$ was reproduced. For small apertures, however, we obtained a power-law relation but with a notably larger exponent. Furthermore, the size of the so-called free fall arch region is also found to decrease due to the rotation.

Finally, granular gas made up of rods and heated by the walls has been studied numerically. Our study provides additional insight into the process for instance by describing the system behavior in the non-symmetrically heated direction, which was not accessible experimentally. The velocity distributions of the particles are examined and found to be well-fitted by stretched exponential distributions, in agreement with previous experiments. Moreover, in the experimentally not accessible direction, we obtained asymmetrical distribution tails. Additionally, the collapsing of the velocity distributions lead us to conclude that the energy scales with the square of the characteristic velocity of the wall.

Resumen

Los flujos granulares se observan con frecuencia en procesos naturales e industriales. El enfoque de este trabajo se dirige a la comprensión de cómo el cambio de las diferentes propiedades de los granos (forma, fricción y rigidez) influye en el caudal de los silos. Complementariamente, se analiza la dinámica del calentamiento de un gas granular de partículas alargadas. En todos estos escenarios, las simulaciones se combinan con experimentos para calibrar y validar las herramientas numéricas empleadas.

En primer lugar, el análisis numérico de la descarga de granos blandos-lisos de un contenedor indicó el desarrollo de un caudal másico dependiente de la altura, lo cual no es habitual en los medios granulares. Nuestro estudio sistemático examinó el espacio de parámetros de fricción y rigidez de las partículas, explorando detalladamente la respuesta macroscópica de este sistema. Complementariamente, el análisis de los campos medios nos ayudó a explicar cuándo y por qué el caudal depende de la altura de la columna. La explicación general incluye: la respuesta del material a los gradientes de presión en el orificio de salida, pero también la forma en que se transmiten los esfuerzos en el sistema. Los resultados nos permitieron proponer argumentos teóricos simples, conectando el caudal macroscópico con el gradiente de presión en el orificio. Como resultado, hemos encontrado una explicación bien razonada de los valores de caudal dependiente de la altura, lo cual ha sido encontrado, experimental y numéricamente, para granos blandos de baja fricción.

En segundo lugar, realizamos una investigación numérica del flujo en un silo bidimensional, usando una de mezclas de granos blandos-lisos y duros-rugosos. Partiendo de un sistema homogéneo de granos blandos-lisos, nuestros resultados numéricos reproducen el alto impacto que produce la inclusión de solo un 5% de los granos duros, en el flujo del conjunto de partículas. Además, resaltaron la importancia de la fricción entre granos de diferente tipo, en le desarrollo de este proceso. Cuando los granos duros-rugosos son agregados al sistema, el flujo se vuelve más lento, los atascos resultan más frecuentes y la fuerza medida sobre el fondo disminuye. Además, resulta que estos efectos se potencian cuando aumenta la fricción entre especies.

También estudiamos, sistemáticamente, la introducción de esfuerzos cortantes, imponiendo la rotación del fondo de un silo plano. Estas condiciones de contorno producen un efecto sorprendente en la descarga de partículas alargadas: el caudal se reduce significativamente, hasta en un 70%. Nuestras simulaciones y la aplicación de los métodos de promediación espacio-temporales revelan las razones subyacentes de esta observación. La velocidad de salida de las partículas es el principal factor que contribuye a esta caída, lo cual correlaciona con la orientación vertical de los granos. Nuestra herramienta numérica permitió explorar la dependencia del caudal Q del tamaño del orificio D. En el límite de los orificios grandes, se reprodujo la clásica correlación de ley de potencia $Q \sim D^{5/2}$. Sin embargo, para aberturas pequeñas obtuvimos una ley de potencia pero con un exponente notablemente mayor. Además, también se encontró que el tamaño de la región denominada "arco de caída libre" disminuye debido a la rotación.

Finalmente, se ha estudiado numéricamente un gas granular agitado formado por partículas alargadas. Este sistema fue estudiado experimentalmente con anterioridad, y nuestro estudio proporciona información adicional sobre el proceso. Por ejemplo, describiendo el comportamiento del sistema en la dirección de calentamiento asimétrico, al que no se accedió experimentalmente. Se estudiaron las distribuciones de velocidad de las partículas, encontrando que ajustan muy bien con distribuciones

exponenciales con colas largas, lo cual está en acuerdo con experimentos previos. Además, en la dirección no accesible experimentalmente, obtuvimos colas asimétricas. El colapso de las distribuciones de velocidad nos lleva a concluir que la energía media del sistema escala con el cuadrado de la velocidad característica de la pared.